STUDY OF CO_2 MOBILITY CONTROL USING CROSS-LINKED GEL CONFORMANCE CONTROL AND CO_2 VISCOSIFIERS IN HETEROGENEOUS MEDIA

A Thesis

by

SHUZONG CAI

Submitted to the Office of Graduate Studies of
Texas A&M University
in partial fulfillment of the requirements for the degree of

MASTER OF SCIENCE

August 2010

Major Subject: Petroleum Engineering

STUDY OF CO_2 MOBILITY CONTROL USING CROSS-LINKED GEL CONFORMANCE CONTROL AND CO_2 VISCOSIFIERS IN HETEROGENEOUS MEDIA

A Thesis

by

SHUZONG CAI

Submitted to the Office of Graduate Studies of
Texas A&M University
in partial fulfillment of the requirements for the degree of

MASTER OF SCIENCE

Approved by:

Chair of Committee,	David S. Schechter
Committee Members,	Robert H. Lane
	Yuefeng Sun
Head of Department,	Stephen A. Holditch

August 2010

Major Subject: Petroleum Engineering

ABSTRACT

Study of CO_2 Mobility Control Using Cross-linked Gel Conformance Control and CO_2 Viscosifiers in Heterogeneous Media. (August 2010)

Shuzong Cai, B.S., Peking University; M.S., New York University

Chair of Advisory Committee: Dr. David S. Schechter

CO_2 has been widely used as a displacement fluid in both immiscible and miscible displacement processes to obtain tertiary recovery from the field. There are several problems associated with the application of CO_2 flooding, especially when there is a significant presence of heterogeneous elements, such as fractures, channels and high permeability streaks within the reservoir. With flooding, CO_2 will finger through the target zone while leaving most of the residual/trapped oil untouched. As a result, early gas breakthrough has been a very common problem in CO_2-related projects, reducing the overall sweep efficiency of CO_2 flooding. This research aims at improving the CO_2 flood efficiency using cross-linked gel conformance control and CO_2 viscosifier technique. A series of coreflood experiment studies have been performed to investigate the possibility of applying CO_2 mobility control techniques. Corresponding simulation works have also been carried out to predict the benefits of applying CO_2 mobility control techniques in the field.

In the laboratory study, the CO_2 coreflood system was integrated with the CT (Computed Tomography)-scanner and obtained real-time coreflood images of the CO_2 saturation distributions in the core. This system was applied to the research of both

cross-linked polymer gel treatment and CO_2 viscosifier study and produced images with sharp phase contrasts. For the gel conformance study, promising results were obtained by applying cross-linked gel to eliminate permeability contrast and diverting CO_2 into low permeability regions to obtain incremental oil recovery; also studied were the gel strength in terms of leak-off extent with the aid of CT (Computed Tomography) images. For the CO_2 viscosifier research, we tested several potential viscosifier chemicals and found out PVAc (Polyvinylacetate)/toluene combination to be the most promising. The follow-up study clearly demonstrates the superiority of viscosified CO_2 over neat CO_2 in terms of sweep efficiency. This research serves as a preliminary study in understanding advanced CO_2 mobility control techniques and will provide insights to future studies on this topic.

ACKNOWLEDGEMENTS

I would like to thank my committee chair, Dr. Schechter, and my committee members, Dr. Lane and Dr. Sun, for their guidance and support throughout the course of this research.

Thanks also go to my friends and colleagues and the department faculty and staff for making my time at Texas A&M University a great experience.

Finally, thanks to my mother and father for their encouragement.

TABLE OF CONTENTS

Page

ABSTRACT iii

ACKNOWLEDGEMENTS v

TABLE OF CONTENTS vi

LIST OF FIGURES viii

LIST OF TABLES xiv

CHAPTER

I INTRODUCTION 1

1.1 Introduction 1
1.2 Objectives 3
1.3 Background 4
1.3.1 CO_2 Flood Theoretical Background 4
1.3.2 CO_2 Displacement Mechanisms 5
1.3.3 Prediction of CO_2 MMP 6
1.3.4 CO_2 Mobility Control 9
1.3.4.1 Cross-linked Polymer Gel Conformance Control ... 10
1.3.4.2 CO_2 Viscosifier / Thickener 16
1.3.4.3 CO_2 Foam 20
1.3.5 CO_2 Flooding Visualization by CT-Scan.. 22
1.4 Methodology 25

II EXPERIMENTAL SETUP 27

2.1 Instrument Setup 27
2.1.1 Injection System 29
2.1.2 Coreflood Cell 29
2.1.3 X-Ray CT Scanner 30
2.1.4 Production System 30
2.1.5 Data Acquisition System30 30
2.2 Core Samples 30
2.3 Chemicals 31

III EXPERIMENTAL CONDITIONS AND PROCEDURE 32

3.1 Background 32

CHAPTER Page

3.2 Conformance Control Study on Gel Properties 32
3.3 Study of Viscosifier Application in CO2 Flooding 34
3.4 Data Processing 39
3.4.1 Porosity Calculation 40
3.4.2 Phase Saturation Calculation 43
3.5 Typical Experimental Procedures 45

IV EXPERIMENTAL RESULTS AND DISCUSSION 47

4.1 Porosity Measurement 47
4.2 Experiments in Unfractured Sandstone 51
4.3 Experiment in Fractured Sandstone 53
4.4 Experiments in Fractured Sandstone Using Cross-linked Polymer Gels for Conformance Control 59
4.4.1 3000 ppm Gel Application 60
4.4.2 10000 ppm Gel Application 68
4.5 Experiments in Heterogeneous Carbonate Using Cross-linked Polymer Gels for Conformance Control 76
4.6 Experiments in Fractured Sandstone Using Viscosified CO_2 87
4.6.1 Neat CO_2 Flooding in Single Fracture Sandstone 88
4.6.2 Viscosified CO_2 Flooding in Single Fracture Sandstone (Dodecamethylpentasiloxane) 96
4.6.3 Viscosified CO_2 Flooding Pressure Drop Test 105
4.6.4 Viscosified CO_2 Flooding in Single Fracture Sandstone (PVAc) 109
4.7 Simulation Study of Viscosified CO_2 Flooding 123
4.7.1 Simulation of Viscosified CO_2 Flooding by CMG 123
4.7.2 General Reservoir Model 126
4.7.3 Simulation of Viscosified CO_2 Flooding for Well A 137

V CONCLUSIONS AND RECOMMNEDATIONS 145

5.1 Conclusions 145
5.2 Recommendations 146

REFERENCES 148

VITA 153

LIST OF FIGURES

FIGURE		Page
1.1	CO_2 Phase Diagram	4
1.2	Guar/Borate Gel System and HPAM/Cr/Acetate Gel System	11
1.3	Chemical Structure of One Copolymer as CO_2 Thickener	19
1.4	Comparison of WAG Front (Left) and CO_2 Foam Front (Right)	24
1.5	Visualization of CO_2 Fluid Flow in Fractured Core after Gel Treatment	25
2.1	Schematic of Instrument Setup	28
3.1	Cross-linking Reaction of the HPAM Polymer Gel	33
3.2	Chemical Structure of Dodecamethylpentasiloxane	35
3.3	Repeating Unit of PVAc	36
3.4	Repeating Unit of Polydimethylsiloxane, Trimethylsiloxy Terminated	37
3.5	Illustration of CT Image Pixel Content Analysis	41
4.1	Color Spectrum (CT number 1500~2200) for CT Images in Section 4.1	48
4.2	Dry Sandstone Core CT Image	48
4.3	Brine Saturated Sandstone Core CT Image	49
4.4	Normal Probability Plot Examination for CT Measured Porosity	50
4.5	Below and Above MMP CO_2 Flood Recovery Curve	52
4.6	Color Spectrum (CT number 1400~1750) for CT Images in Section 4.3	54
4.7	Scan of 100% CO_2 Saturated Fractured Sandstone Core	54
4.8	Scan of 100% Brine Saturated Fractured Sandstone Core	55
4.9	Scan at OOIP Oil Saturation after Oil Injection/Water Drainage Process	55

FIGURE Page

4.10 Scan 1 after the Start of the CO_2 Flooding 56

4.11 Scan 2 after the Start of the CO_2 Flooding 56

4.12 Scan 3 after the Start of the CO_2 Flooding 57

4.13 CO_2 Saturation Distribution in Highly Fractured Sandstone Core 58

4.14 Designed Fractured Sandstone Pattern for Gel Conformance Control Study .. 59

4.15 Color Spectrum (CT Number 1200~1800) for CT Images in Section 4.4.1 61

4.16 Scan of 100% CO_2 Saturated Fractured Sandstone Core 61

4.17 Scan of 100% Oil Saturated Fractured Sandstone Core 61

4.18 Scan at 2 Min of the CO_2 Flooding 62

4.19 Scan at 6 Min of the CO_2 Flooding 62

4.20 Scan at 12 Min of the CO_2 Flooding 63

4.21 Scan at 25 Min of the CO_2 Flooding 63

4.22 Scan before Gel Injection at 100 psi Gel Injection Pressure 64

4.23 Scan after Gel Injection at 100 psi Gel Injection Pressure 64

4.24 Scan at 2 Min of CO_2 Flooding in Core with Gel Placement 65

4.25 Scan at 30 Min of CO_2 Flooding in Core with Gel Placement 65

4.26 CO_2 Saturation Distribution in Fractured Sandstone Core 66

4.27 CO_2 Flood Recovery Curve for Fractured Sandstone 67

4.28 Color Spectrum (CT Number 1200~1800) for CT Images in Section 4.4.2 69

4.29 Scan of 100% CO_2 Saturated Fractured Sandstone Core 69

4.30 Scan of 100% Oil Saturated Fractured Sandstone Core 70

4.31 Scan at 4 Min of the CO_2 Flooding 70

FIGURE Page

4.32 Scan at 9 Min of the CO_2 Flooding 70

4.33 Scan at 25 Min of the CO_2 Flooding 71

4.34 CO_2 Saturation Distribution in Fractured Sandstone Core 72

4.35 Scan before Gel Injection at 100 psi Gel Injection Pressure 72

4.36 Scan after Gel Injection at 100 psi Gel Injection Pressure 72

4.37 Scan at 2 Min of CO_2 Flooding in Core with Gel Placement 73

4.38 Scan at 30 Min of CO_2 Flooding in Core with Gel Placement 73

4.39 Comparison between the CT Images from the End of Coreflood for 3000 ppm (Above) Gel and 10000 ppm (Below) Gel 74

4.40 Oil Recovery Curve for CO_2 Flooding in Fractured Sandstone 75

4.41 Color Spectrum (CT Number 1800~2400) for CT Images in Fig. 4.37 76

4.42 Scan of Impermeable Carbonate Core during Attempted CO_2 flooding 76

4.43 Color Spectrum (CT Number 1700~2400) for CT Images in Section 4.5 78

4.44 Scan of 100% CO_2 Saturated Heterogeneous Carbonate Core 78

4.45 Scan of 100% Oil Saturated Heterogeneous Carbonate Core 79

4.46 Scan at 5 Min of the CO_2 Flooding 79

4.47 Scan at 8 Min of the CO_2 Flooding 80

4.48 Scan at 15 Min of the CO_2 Flooding 80

4.49 Scan at 40 Min of the CO_2 Flooding 80

4.50 Scan before Gel Injection at 100 psi Gel Injection Pressure 81

4.51 Scan after Gel Injection at 100 psi Gel Injection Pressure 81

4.52 CT Nnumber Increase Before and After Gel Placement 82

4.53 Scan at 2 Min of CO_2 Flooding after Gel Placement 83

FIGURE Page

4.54 Scan at 30 Min of CO_2 Flooding after Gel Placement 83

4.55 Inspection of the Actual Core Images 84

4.56 CO_2 Saturation Profile Distribution in Heterogeneous Carbonate Core 85

4.57 CO_2 Flood Recovery Curve for Heterogeneous Carbonate Core 86

4.58 Sandstone Core with a Single Fracture in the Center 87

4.59 Color Spectrum (CT Number 1400~1800) for CT Images in Section 4.6.1 88

4.60 Scan of 100% CO_2 Saturated Single Fractured Sandstone Core 89

4.61 Scan of 100% Oil Saturated Single Fractured Sandstone Core 89

4.62 Vertical Slice Images of the Single Fractured Sandstone Core From Scan 1 .. 90

4.63 Scan 1 during the CO_2 Flooding in Single Fractured Sandstone 90

4.64 Vertical Slice Images of the Single Fractured Sandstone Core From Scan 2 .. 91

4.65 Scan 2 during the CO_2 Flooding in Single Fractured Sandstone 92

4.66 Vertical Slice Images of the Single Fractured Sandstone Core From Scan 3 .. 93

4.67 Scan 3 during the CO_2 Flooding in Single Fractured Sandstone 93

4.68 CO_2 Saturation Profile for Neat CO_2 Flood 94

4.69 Color Spectrum (CT Number 1400~1800) for CT Images in Section 4.6.2 98

4.70 Scan of 100% CO_2 Saturated Single Fractured Sandstone Core 98

4.71 Scan of 100% Oil Saturated Single Fractured Sandstone Core 98

4.72 Slice Images of the Single Fractured Sandstone Core From Scan 1 99

4.73 Scan 1 during the CO_2 Flooding in Single Fractured Sandstone 100

4.74 Vertical Slice Images of the Single Fractured Sandstone Core From Scan 2 .. 101

4.75 Scan 2 during the CO_2 Flooding in Single Fractured Sandstone 101

FIGURE Page

4.76 Vertical Slice Images of the Single Fractured Sandstone Core From Scan 3 .. 102

4.77 Scan 3 during the CO_2 Flooding in Single Fractured Sandstone 103

4.78 CO_2 Saturation Profile for Viscosified CO_2 Study..... 103

4.79 Color Spectrum (CT Number 1400~1800) for CT Images in Section 4.6.4 110

4.80 Scan of 100% CO_2 Saturated Single Fractured Sandstone Core..... 110

4.81 Scan of 100% Oil Saturated Single Fractured Sandstone Core 110

4.82 Vertical Slice Images of the Single Fractured Sandstone Core From Scan 1 .. 111

4.83 Scan 1 during the CO_2 Flooding in Single Fractured Sandstone 111

4.84 Vertical Slice Images of the Single Fractured Sandstone Core From Scan 2 .. 112

4.85 Scan 2 during the CO_2 Flooding in Single Fractured Sandstone 113

4.86 Vertical Slice Images of the Single Fractured Sandstone Core From Scan 3 .. 114

4.87 Scan 3 during the CO_2 Flooding in Single Fractured Sandstone 114

4.88 CT Image of Single Fractured Sandstone Core before Injecting PVAc Viscosified CO_2..... 115

4.89 Vertical Slice Images of the Single Fractured Sandstone Core From Scan 4 .. 116

4.90 Scan 4 during the CO_2 Flooding in Single Fractured Sandstone 116

4.91 Vertical Slice Images of the Single Fractured Sandstone Core From Scan 5 .. 117

4.92 Scan 5 during the CO_2 Flooding in Single Fractured Sandstone 117

4.93 Vertical Slice Images of the Single Fractured Sandstone Core From Scan 6 .. 118

4.94 Scan 6 during the CO_2 Flooding in Single Fractured Sandstone 118

4.95 CO_2 Saturation Profile for PVAc Viscosified CO_2 120

4.96 Oil Recovery with Pore Volume of CO_2 Injected Comparison 121

4.97 CO_2 Saturation with Pore Volume of CO_2 Injected Comparison..... 121

FIGURE Page

4.98 Three-Component Miscible Displacement in a Grid Block 124

4.99 Mixing Parameter *vs.* Pressure 125

4.100 1/8 of a 5-Spot CO_2 Pattern Flood Model 126

4.101 3-D Representation of the CO_2 Pattern Flood Model 127

4.102 Mixing Parameter and CO_2 Viscosity Changing with Pressure 128

4.103 Different Viscosity Curves Changing with Pressure 129

4.104 Solvent Saturatoin Distribution for Three Different Simulation Runs 130

4.105 Simulation Results: Oil Rate for Case 1 to Case 3 132

4.106 Simulation Results: Cumulative Oil Rate for Case 1 to Case 3 133

4.107 Solvent Production Rate for Case 1-3 133

4.108 Well Block Pressure vesus Well Bottom-hole Pressure for Case 1-3 135

4.109 3-D Representation of Well A Model 139

4.110 Oil Rate for Case 4 and Case 5 140

4.111 Cumulative Oil Rate for Case 4 and Case 5 141

4.112 Solvent Production Rate for Case 4 and Case 5 142

4.113 Solvent Saturation Distribution in the 3D Reservoir Model at the End of Simulation (Above: Case 4, Below: Case 5) 143

LIST OF TABLES

TABLE		Page
3.1	Typical Concentrations HPAM/$Cr(OAc)_3$ Polymer Gel System	34
4.1	Porosity Measurement Result for Berea Sandstone	49
4.2	Oil Recovery Table for Neat CO_2 Flooding	95
4.3	Van Der Waals Coefficients of Selected Gases	97
4.4	Oil Recovery Table for Viscosified CO_2 Flooding	104
4.5	Pressure Drop Test Results	108
4.6	CT-Scan Scheme for PVAc Viscosifier Study	109
4.7	Oil Recovery Table for Neat/Viscosified CO_2 Flooding	119
4.8	Well A Model Properties and Injection Details	137

CHAPTER I

INTRODUCTION

1.1 Introduction

CO_2 has been widely used as a displacement fluid in both immiscible and miscible displacement process to obtain tertiary recovery from the field. The high solubility of CO_2 in crude oil makes it ideal to "swell" the net volume of oil, thereby reducing oil viscosity. The importance of utilizing CO_2 can be attributed to two factors: First, CO_2 is readily available from industrial emission. Second, it is one of the most promising ways to reduce greenhouse gas emission. A study by the U.S. Office of Technology Assessment has indicated that the total CO_2 required as an Enhanced Oil Recovery (EOR) fluid could ultimately reach 50×10^{12} SCF.[1]

There are several problems associated with the application of CO_2 flooding, especially when there is a significant presence of heterogeneous elements such as fractures, channels and high permeability streaks within the reservoir; CO_2 will finger through the target zone while leaving most of the residual/trapped oil untouched. As a result, early gas breakthrough has been a very common problem in CO_2-related projects, reducing the overall sweep efficiency of CO_2 flooding. The CO_2 "Utilization Factor" which is the number of thousands of cubic feet (Mcf) of CO_2 injected per barrel of oil recovered will be greatly increased and will eventually cause the production to become uneconomical.

This thesis follows the style of *Journal of Petroleum Technology*.

Thus, it is essential to develop novel CO_2 mobility control techniques in order to apply CO_2 flood in highly heterogeneous reservoirs.

Three major techniques have been proposed to increase the CO_2 flood efficiency: Cross-linked gel conformance control, CO_2 viscosifier and CO_2 foams. Conformance control is the process of injecting cross-linked-gel into the reservoirs to modify the permeability profile. It usually targets high permeability regions such as fractures or high permeability streaks; its purpose is to direct CO_2 fluid into low permeability regions after gel treatment to the high permeability regions.

CO_2 viscosifier is the most direct way to increase the viscosity of CO_2, hence improving the overall sweep efficiency; high molecular weight polymer and cosolvent are blended and pressurized together with CO_2 so that the fluid viscosity can be greatly increased before CO_2 is injected for oil recovery. Unforunately, this is the most underdeveloped method compared to other CO_2 flooding improvement techniques. The most significant problem in the research towards perfect CO_2 viscosifier is balancing the solubility and viscosity properties of polymer materials.

CO_2 foam is the simultaneous injection of CO_2 fluid and surfactant fluid into the reservoir. This technique has not drawn as much attention due to the lack of understanding in the foaming mechanism and it is not as promising as two previously mentioned techniques and we decided to leave it out of this research project.

Our laboratory work employs a novel design which integrates the fourth generation X-Ray CT scanner with a specially fabricated aluminum coreflood cell. Experiments were carried out at various pressure and flow rate conditions. With the integrated system we were able to obtain real-time fluid distribution images in the cores. We could also obtain

quantitative phase saturation information from the CT data measured in different stages of coreflood experiments. The laboratory research includes the preliminary study of immiscible/miscible CO_2 flood, testing of gel performances in heterogeneous carbonate/sandstone cores, and screening the performances of novel CO_2 viscosifier chemicals. All of these results were obtained from a series of distinctively designed coreflood experiments. We also confirmed our laboratory research results by simulating gel conformance control and CO_2 viscosifier performance using CMG reservoir simulation software.

1.2 Objectives

Our research work aims at improving CO_2 flood efficiency using novel CO_2 mobility control techniques. For the initial stage of the research, the coreflood system combining CT scanner is examined to prepare for more complicated studies. Then, factors affecting the Minimum Miscibility Pressure are investigated. To study the cross-linked gel conformance control technique, such factors as pressure, temperature, gel/cross-linker concentration are investigated with the eventual goal of comparing different gel strengths with the aid of CT-scan technique. To study the CO_2 viscosifier technique, the available industrial/laboratory chemicals from the market are surveyed and promising formulation of CO_2 viscosifiers are tested to observe the contribution from applying CO_2 viscosifier; the CT images are used to provide robust supportive information when comparing the overall sweep efficiencies between different CO_2 flooding experiments.

1.3 Background

In this section CO_2 flood theories and mechanisms are reviewed. A literature review is followed to provide an up-to-date summary on various CO_2 mobility control methods. The focus, however, will be on gel conformance control and CO_2 viscosifiers.

1.3.1 CO_2 Flood Theoretical Background

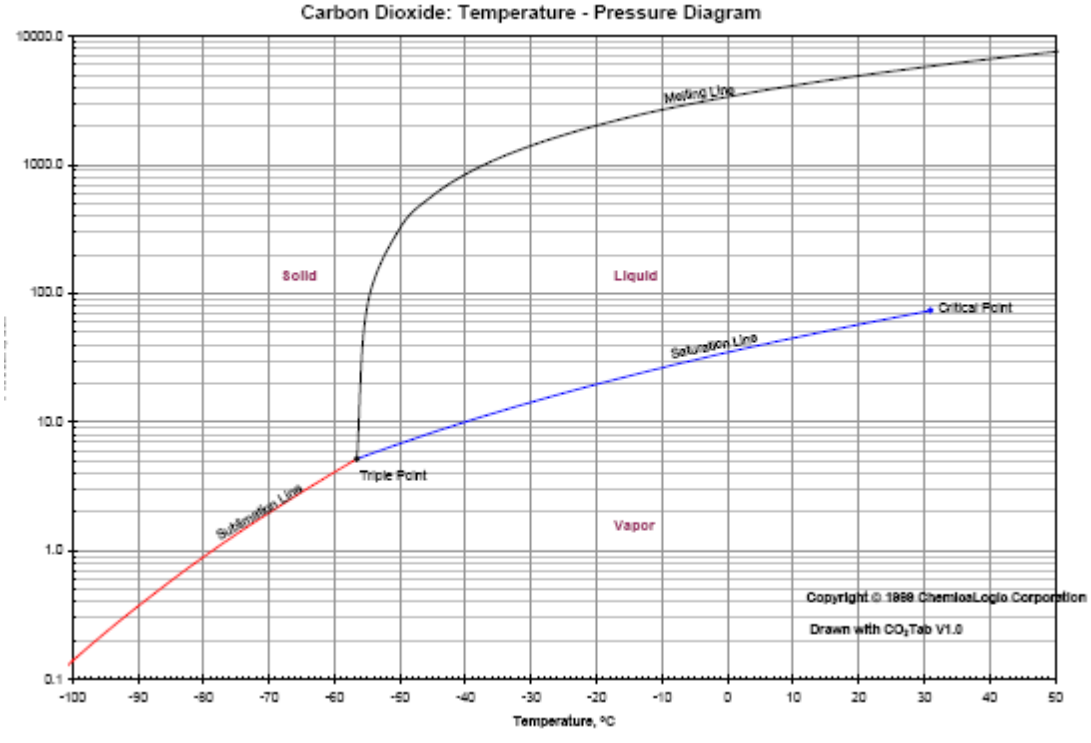

Fig. 1.1 – CO_2 Phase Diagram[2]

Understanding of the characteristics of CO_2 is helpful in developing new effective CO_2 mobility control methods to improve CO_2 flooding performance. Fig. 1.1 shows a typical CO_2 phase diagram and it can be observed that CO_2 can easily be in a supercritical fluid state at relatively low temperature and pressure conditions (Critical

point at 1070 psi and 89 °F). At this supercritical fluid state, CO_2 exhibits significant changes in solubility, interfacial tension and density.

1.3.2 CO_2 Displacement Mechanisms

The mechanisms by which CO_2 displaces oil can be classified as following[3]:

1. Solution gas drive: Solution gas drive usually occurs at low pressure conditions. It involves dissolution of CO_2 into oil at initial pressure and release of CO_2 at a later time after the depletion of pressure. Very few field cases have utilized this technique.
2. Immiscible CO_2 drive: This mechanism is characterized by liquid-liquid immiscible CO_2 flooding. This drive mechanism can be applied at relatively low reservoir pressure. Industrial applications of this mechanism include Water Alternating Gas (WAG) injections.
3. Hydrocarbon-CO_2 miscible drive: Light hydrocarbons such as methane, ethane and propane can be completely miscible with CO_2 at relatively low temperature. Therefore, low molecular weight hydrocarbon and CO_2 slug can be formed in the front of a CO_2 drive. However this has not been utilized much in the field and very few successful cases have been reported.
4. Hydrocarbon vaporization: For light oil, CO_2 has the ability to extract and vaporize hydrocarbons and transfer those hydrocarbons from the reservoir. However, only low molecular weight hydrocarbons can satisfy the requirements for this application.
5. First Contact Miscible process (FCM) (direct miscible CO_2 drive): This mechanism requires immediate and complete miscibility between CO_2 and

hydrocarbon in the reservoir. Relatively high pressure and temperature are required for this application. At practical reservoir conditions, direct miscibility is hard to achieve.

6. Multiple-Contact Miscible process (MCM): In this mechanism, multiple-contact between oil and CO_2 is necessary compared to the direct contact miscible mechanism. The depth of vaporization and extraction of hydrocarbons from crude oil is not as significant. However, miscible front breaks down when it comes in contact with new crude oil, and new miscible front must be constantly formed by vaporization or extraction mechanism so that miscibility can be maintained.[4] So far, required pressure for multiple-contact miscible displacement with CO_2 has not been properly determined because of the wide range of possible pressure at which extraction of hydrocarbons for CO_2 begins. Different correlations to predict miscibility pressure will be discussed.

1.3.3 Prediction of CO_2 MMP

In order to successfully design and implement a CO_2 injection EOR project, it is essential to predict the minimum miscibility pressure (MMP) in combination with the actual reservoir conditions. To determine MMP by experimental methods (slim tube test) is both expensive and time consuming.[5]

Preliminary analytical correlations can be used to estimate MMP; this gives us information regarding whether our displacement mechanism in the reservoir is miscible or immiscible.

Miscible Displacement can be classified as First Contact Miscible (FCM) process or Multiple-Contact Miscible (MCM) process. In the FCM process injected CO_2 and oil in

the reservoir will form a single phase mixture. In MCM process heavier components of the reservoir oil are not miscible with CO_2 upon first contact but miscibility develops after multiple contacts. MCM is characterized by repeating vaporizing and condensing drive mechanisms. Because FCM usually requires high pressure to take place, MCM CO_2 floods are the most effective EOR methods available in actual field production cases.

Glasø[6] has proposed a correlation based on earlier work of Benham[7] *et al.* . The MMP is predicted by reservoir temperature, molecular weight of C_{7+}, mole percent ethane in the injected gas and the molecular weight of the intermediates (C_2 through C_6) in the gas.

$$(MMP)_{x=34} = 6{,}329 - 25.410 \times y - (46.475 - 0.185 \times y) \times z + (1.127 \times 10^{-12} \times y^{5.258} \times e^{319.8zy^{-1.703}}) \times T$$

……..(1.1)

$$(MMP)_{x=44} = 5{,}503 - 19.238 \times y - (80.913 - 0.273 \times y) \times z + (1.7 \times 10^{-9} \times y^{3.730} \times e^{13.567zy^{-1.508}}) \times T$$

……..(1.2)

$$(MMP)_{x=54} = 7{,}437 - 25.703 \times y - (73.515 - 0.214 \times y) \times z + (4.920 \times 10^{-14} \times y^{5.520} \times e^{21.706zy^{-1.109}}) \times T$$

……..(1.3)

x= the molecular weight of C_2 through C_6 components in injection gas in lbm/mol

y= corrected molecular weight of C_{7+} in the stock-tank oil in lbm/mol

$$y = \left(\frac{2.622}{\gamma_{C_{7+}}^{-0.846}} \right)^{6.558}$$ ……...……(1.4)

γ_{C7+}= specific gravity of heptane-plus fraction

z= mole percent methane in injection gas

Firoozabadi *et al.*[8] has proposed another simple correlation to predict MMP for lean natural gas or N_2 injection. Correlating parameters include the concentration of intermediates, the volatility, and the temperature. C_6 is excluded from the intermediate to improve the correlation of MMP.

$$MMP = 9{,}433 - 188\times10^3 \times\left(\frac{x_{\text{int}}}{M_{C7+}T^{0.25}}\right) + 1430\times10^3 \times\left(\frac{x_{\text{int}}}{M_{C7+}T^{0.25}}\right)^2 \quad \text{.....(1.5)}$$

$x_{\text{int}} = x_{CO2} + \sum_{i=2}^{i=5} x_i$ =mole percent of intermediates in the oil

M_{C7+}= molecular weight of heptane plus.

Eakin *et al*. [9] have presented another MMP correlation method using Rising Bubble Apparatus (RBA). Correlating parameters are solvent composition, C_{7+} molecular weight and the pseudo-reduced temperature of the reservoir fluid. To calculate pseudo-critical temperature T_{pc} and pseudo-critical pressure P_{pc}, Kay's rules were used.

$$\ln p_{pr} = \ln(MMP/p_{pc}) = (0.1697 - 0.06912/T_{pr})\times y_{C1}\times M_{C7+}^{0.5}$$
$$+ (2.3865 - 0.005955\frac{M_{C7+}}{T_{pr}})\times y_{c2+} + (0.01221M_{C7+} - 0.0005899\frac{M_{C7+}^{1.5}}{T_{pr}})\times y_{CO2} \quad \text{.....(1.6)}$$

y= mole fraction of certain molecular weight range hydrocarbon in the reservoir fluid

T_{pr}= pseudo reduced temperature of the reservoir fluid

T_{pc}= pseudo critical temperature of the reservoir fluid

P_{pr}= pseudo reduced pressure of the reservoir fluid

P_{pc}= pseudo critical pressure of the reservoir fluid

Since most of these correlations do not account for the fluid composition properly, Firoozabadi *et al.* and Eakin *et al*. correlations are considered to be relatively more reliable.

For our coreflood experiments we decided to use the Cronquist correlation[10] from DOE reports because of our limited fluid data:

$$MMP = 15.988T^{(0.744206+0.0011038MwC5+)} \quad \text{.....(1.7)}$$

T: Temperature in Fahrenheit

Mw C5+: The molecular weight of pentanes and heavier fractions in the reservoir oil

1.3.4 CO_2 Mobility Control

There are several problems associated with the application of CO_2 flooding, especially when there is a significant presence of heterogeneous elements such as fractures, channels and high permeability streaks within the reservoir; CO_2 will finger through the target zone while leaving most of the residual/trapped oil untouched. As a result, early gas breakthrough has been a very common problem in CO_2-related projects, reducing the overall sweep efficiency of CO_2 flooding. The CO_2 "Utilization Factor" which is the number of thousands of cubic feet (Mcf) of CO_2 injected per barrel of oil recovered will be greatly increased and will eventually cause the production to become uneconomical.

In order to address these problems of mobility control during CO_2 flooding, different methods have been employed. The most studied three approaches are: (1) cross-linked polymer gel conformance control; (2) CO_2 viscosifier / thickener; (3) CO_2 foam. In the following sections three major CO_2 mobility control methods will be reviewed; with emphasis on the first two methods since these two methods have been adopted in our research.

1.3.4.1 Cross-linked Polymer Gel Conformance Control

Developments in conformance control technique are in relatively mature stage in enhanced oil recovery operations. The basic idea of conformance control technique is to inject cross-linked polymer into the reservoir to modify the permeability profile so that CO_2 does follow fractures or high permeability streaks/channels. Thus, this method improves the overall sweep efficiency.

Polyacrylamide polymer gels with chromium (III) cross-linkers have been widely used in fracture system treatment, casing-leaks, water shut-off, and permeability reduction operations in the fields. Recently, it has been tested for CO_2 flooding conformance control by in-depth placement of the cross-linked gel into a reservoir. In comparison with another common gel system Guar/Borate, Polyacrylamide gel system is more resistant to acidic conditions caused by CO_2 treatment compared to another common gel system, Guar/Borate, that can only survive relatively basic pH environments. As shown in Fig. 1.2, Boron (III) center cation is very susceptible to acidic conditions and the cross-linked gel will dissociate into separate polymer chains.

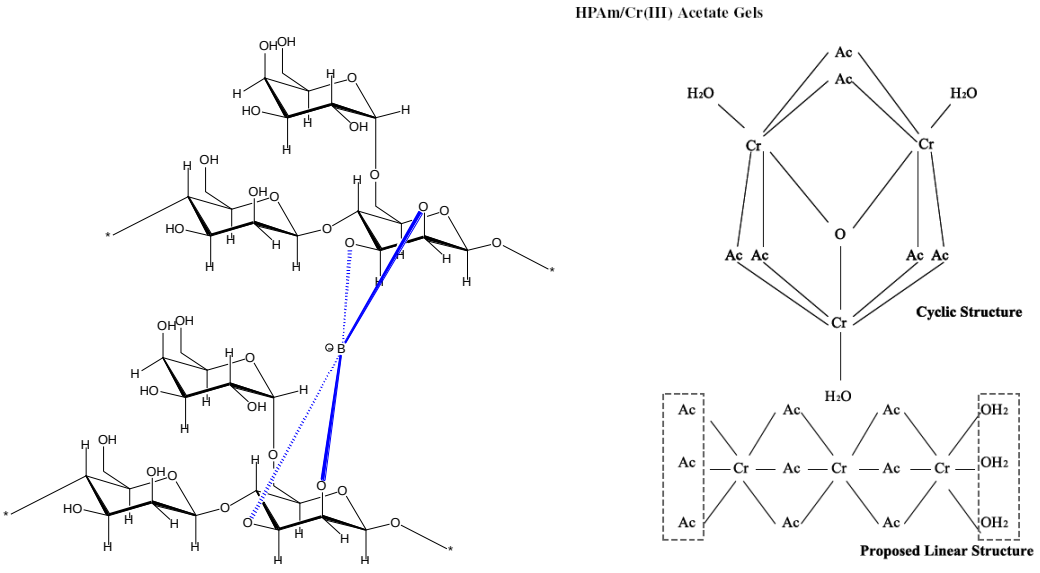

Fig. 1.2 – Guar/Borate Gel System and HPAM/Cr/Acetate Gel System[11]

HPAM (Partly Hydrolyzed Polyacrylamide) $Cr(OAc)_3$ (Chromium (III) Acetate) Polymer Gel is one of the most commonly used Polyacrylamide type polymer gels in the field. HPAM / $Cr(OAc)_3$ Polymer gels have been used in polymer floods. In other applications, these gels have been used in water shut-off to reduce water production and in zone abandonment.

There are two commonly used approaches to apply the HPAM / $Cr(OAc)_3$ polymer gel system depending on the conditions of the reservoir; pre-formed gel and in-situ formed gel:

In the former approach, a pre-formed cross-linked gel is prepared before injection. Then, the HPAM polymer beads are dissolved and hydrated first in brine, and cross-linker $Cr(OAc)_3$ will be added next. The whole mixture is left to cure overnight or even for days, depending on the actual gelation time of the gel system. The pre-formed cross-linked gel prepared this way has a very high viscosity and low permeability in the

matrix. The cross-linked gel is expected to extrude through fractures without invading and damaging the reservoir matrix.

In the latter approach, HPAM polymer solution and $Cr(OAc)_3$ solution are mixed and immediately, the mixture is injected in the reservoir before the gelation process is completed. The injected reaction mixture is not in cross-linked state yet; without the cross-linked polymer gel structure, the mixture still contains uncross-linked polymer strands and it can enter the reservoir matrix. This mixture solution is expected to go into high permeability regions of the reservoir to eliminate permeability distribution heterogeneities. The mixture then turns into polymer aggregates in the reservoir matrix and starts to form cross-linked gel in reservoir conditions. CO_2 injection should not start until the cross-linking reaction is completed in the reservoir. Previous studies suggest that a longer time is needed for gel cross-linking process if it takes place in the reservoir.[12] This approach is suitable for CO_2 flood in heterogeneous yet unfractured carbonate reservoirs with varying permeability.

Some examples of previous studies on conformance control technique are discussed in the following section in terms of experimental conditions and procedures along with the significance of these studies.

Kovarik *et al*. studied the effects of commercial gelants to reduce CO_2 permeability as early as 1987.[13] The experimental conditions for the core tests were 1500 psi and 105 °F, which was set in reference to reservoir conditions in some west Texas/southeast New Mexico reservoirs. The MMP was claimed to be around 1200 psi. The permeability tests provided information on gel stability and polymer-gel interactions. Three types of gels were used in this study: PAM Cyanagel 100 with Cr (VI) cross-linkeder, Pfizer

FLOCON 4800P with Pfizer X-LINK 1000 cross-linkeder, and in-situ cross-linkeder PAM/OCL. The cores used were Berea cores (sandstone). Some improvements on brine/CO_2 WAG (Water Alternating Gas) injection performances have been observed after gel treatment. Although matrix was not affected by gel infiltration, some gel became mobile after WAG injection. This result showed the necessity to evaluate the long-term stability of different gel systems. The researchers attempted to visualize fluid flow scenarios in 2-D, but the end product was not very satisfactory. Fortunately, this visualization is much clearer today with our updated CT-scan visualization technique.

R. S. Seright extensively studied the mechanism for Polyacrylamide/Chromium acetate gel propagation through fractures.[14] During large volumes of gel injection, a special experimental set-up was devised to measure the pressure drops of different intervals of fractures. Pressure gradients were monitored and effluents from fractures were also analyzed. It was found out that the concentrated gel completely filled the width of the fracture but the thickness of the filter cake was not affected by the amount of gel injected; the extra amount of gel injected only changed the dehydrated gel filter cake concentration. A simple model was developed in their study to account for the relationship between pressure gradient and gel extrusion possibility:

$$dp/dl = 0.02/(w_f)^2 \quad \text{.....(1.8)}$$

w_f : fracture width

Other similar correlations were also proposed by Seright *et al*.; their equations predict in-depth gel placement extent during gel conformance control coreflood experimental study.

Most of the studies on gel conformance control have focused on sandstone reservoirs more than carbonate reservoirs. Taabbodi *et al*. investigated the application of gel placement onto carbonate porous medium to reduce its permeability to water and supercritical CO_2.[15] The gel systems used were high and low molecular weigh polyacrylamide polymer with chromium (III) as cross-linker. Sodium lactate was added to some of the experiments to extend the gelation time. In some of their experiments, residual oil was present inside the core t its effect on gel performance. It was found out that permeability reduction decreased when there was residual oil saturation present inside the core. Gelation time, permeability tests were carried out to show the effectiveness of different gel systems for conformance control. However, their experimental condition of 1200 psi and 100 °F is still very close to CO_2 critical point and it might not be enough to guarantee the claimed supercritical CO_2 fluid state.

G. P. Hild and R. K. Wackowski reported the application of polyacrylamide/ chromic-acetate polymer gel system to improve CO_2 flood performance at Rangely Weber Sand Unit in northwestern Colorado.[16] Significant amount of gel (10,000 bbl) have been pumped in this unit for 44 injection well treatments. Previously only small volumes of gel were injected by near-wellbore methods. In more recent projects, significant volumes of diverting agents were injected to correct the poor vertical and areal sweep in the reservoir. Since this gel system requires a minimum permeability of several hundred mD for matrix placement, it ensures that the injected gel will not invade deep into the matrix and low permeability wells will not be damaged after the injection of gel. An average incremental oil of 21 bbls/day was achieved for the unit and water production was reduced by 98 bbls/day.

Another successful pilot field application of conformance control for CO_2 flooding using gel treatment was reported by Celebioglu *et al*.[17] The CO_2 injection project is at Bati Raman heavy-oil filed in Southeastern Turkey. This reservoir is a naturally fractured carbonate reservoir which has problems of poor sweep efficiency of CO_2. Chromium acetate-cross-linked polyacrylamide gels were used and a flowing gel condition was applied to plug the vuggy and fractured zones. Large volumes, sometimes as much as 10,000 bbls, of gel were injected to each well. This attempt tuned out to be both technically and economically successful; the incremental oil after the gel treatment can be 330, 000 bbls for 10 years.

Although polyacrylamide/chromium gel system has settled down as the rule of thumb for CO_2 conformance control, some novel gel systems were also tested in different research labs. However, considering the cost of these synthetic chemicals, these materials are still far from being applied in the large scale field production.

Willhite *et al*. reported a laboratory study on some novel in-situ gel systems including KUSP1 biopolymers and SMRF (sulfomethylated resorcinol/formaldehyde gel).[18] Effective permeabilities of brine and CO_2 before and after gel treatments were measured and compared. For KUSP1, in-situ polymerization has been initiated by injecting supercritical CO_2 and permeability reduction as much as 80% has been observed. Other methods to initiate polymerization were also tested for KUSP1 such as using an ester to promote reaction. For SMRF system, the reaction between two components promoted an in-situ polymerization and permeability reduction was as high as 99%. Since these were only permeability tests, no oil recovery coreflood tests were attempted.

Dong *et al*. investigated a more novel approach to control CO_2 permeability.[19] In their study, enzyme bovine carbonic anhydrase was used to facilitate the precipitation of calcium carbonate in the presence of both CO_2 and calcium ions. This precipitation caused reduction in permeability of the flooded region of the reservoir, thus improving the subsequently injected CO_2 sweep efficiency. The enzymatic hydration reaction mechanisms were studied under different temperature and concentration conditions. It was shown that the enzymatic precipitation of $CaCO_3$ was not dependent on the concentration of bovine enzyme. Two flow experiments were carried out with different injection sequences. Reduction of CO_2 permeability was higher when the $CaCl_2$/Enzyme fluid and CO_2 fluid were injected simultaneously (permeability reduction from 9.81 mD to 2.49 mD). However, the coreflood experiments had only small pressure drops (~40 psi) thus they were not proper indications of the actual reservoir pressure and temperature conditions. However, their research serves to provide an alternative for conformance control by using enzymes instead of large quantities of polymer gels.

1.3.4.2 CO_2 Viscosifier / Thickener

CO_2 viscosifier is the most direct way to control the mobility of CO_2. (Note: the term "viscosifier" has the same meaning as "thickener" throughout the thesis.) However, this is also the technique that is most underdeveloped comparing to other CO_2 flooding improvement techniques. The most significant problem in the research towards perfect CO_2 viscosifier is balancing the solubility and viscosity properties of polymer materials.

During multiple contact miscibility, which commonly occurs at pressures above the minimum miscibility pressure, CO_2 obtains a relatively high density (above 0.45 g/cm^3) at reservoir conditions. However, owing to the low viscosity of dense CO_2 (in the range

of 0.03 to 0.08 cp), it is not as effective in displacing oil. This leads to a high mobility ratio for the CO2 and in turn significantly decreases the macroscopic efficiency of CO_2.

Heller *et al*. (1985) provided the first reports on viscosity increasing polymers for reducing mobility of CO_2 in EOR applications.[20] In their work, they attempted to find viscosity increasing chemicals that were soluble in supercritical or dense CO_2. However, none of their soluble polymers yielded significant increase in viscosity for CO_2 fluids.

Terry *et al*. also conducted similar polymerization reactions in supercritical CO_2 in an attempt to increase CO_2 viscosity.[21] They used olefin monomers (about 10-50 vol %) and benzoyl peroxide as an initiator (1.2-3.0 wt % of monomer) for the polymerization reaction. Even though they were successful in performing the polymerization reaction and dissolving polymers in supercritical CO_2, no apparent viscosity increase was observed.

An applicable CO_2 viscosifier is expected to increase the CO_2 viscosity by 1 to 2 orders of magnitude while keeping the CO_2 viscosifier concentration under 5 wt %. The diluted viscosifier chemical concentration will minimize the process cost and formation damage caused by viscosifier chemical deposition. More ideally, 10-100 fold increase is expected from 0.1-2.0 wt % viscosifier CO_2 solution. Previously, conventional hydrocarbon-based polymers, telechelic ionomers, organometallic compounds, surfactants, hydroxystearic acid and ammounium carbamates have all been tried as CO_2 thickener. However, large amounts of these materials are needed to increase the CO_2 viscosity.

DeSimone *et al*. conducted polymerization in liquid and supercritical CO_2 using poly(1,1-dihydro perfluoro octyl acrylate) with a high molecular weight. 6.7 wt / vol %

polymer was blended in CO_2 and viscosity increased from 0.08 mPa s to 0.2-0.6 mPa.s at 23-35 Mpa.[22]

The most feasible research on CO_2 thickener for CO_2 flooding was conducted by Bae *et al.*.[23] Most of the CO_2 viscosifiers tested were commercial siloxane polymers. Different solubility issues regarding the viscous CO_2 process had emerged and a polymer screening process was conducted. When a commercial polydimethyl siloxane polymer from General Electric (GE) was used as CO_2 thickener with toluene used as cosolvent, corefloods experiments showed that supercritical CO_2 was viscosified by two orders of magnitude, forming a single-phase admixture. The use of cosolvent also helped in reducing minimum solubility pressure (MSP) which rendered this method viable for field use. The viscous phase of CO_2 consisted of 4 wt % polymer and 20 wt % toluene and had a viscosity of 1.2 cp at experimental conditions of 130 °F and 2500 psi. Using a cosolvent was necessary because of the low solubility of the test chemicals in supercritical CO_2 and a screening for the cosolvent was conducted. Some coreflood experiments were conducted and oil recovery was shown as a function of cumulative fluid injection. A significant delay in gas breakthrough was observed with viscosified CO_2. Oil production was increased and accelerated. Through infrared spectrophotometer analysis, partition of the injected polymer between CO_2 and crude oil phase was studied; the analysis showed that only a small amount of the injected polymer blended in with the produced oil. For most of the experiments, oil viscosity was not significantly altered ("significant" defined as 10 to 100 fold increase). However, an economic analysis on this approach also concluded that the costs of polymer and the cosolvent (toluene) made the viscous CO_2 economically unfeasible with the concurrent market prices of oil and

chemicals. No further work was done in continuation to this approach. This method will be the basis for our viscosified CO_2 EOR approach. Especially, it will be worthwhile to see if current crude oil prices and chemical costs make the process economical now.

Enick *et al*. did an extensive study on the development of a novel CO_2 thickener without cosolvent.[24] Their research work between 2001 and 2004 provided some guidance for the structural design of possible CO_2 thickener. However, this research funded by Department of Energy did not yield any industrially applicable polymer materials for CO_2 EOR projects. Polymers, surfactants, dispersants and chelating agents with high solubility in CO_2 were synthesized with CO_2-philic fluoroether functionality. One fluoroacrylate-styrene random copolymer reported by them is credited as the first associative thickener for CO_2.[25]

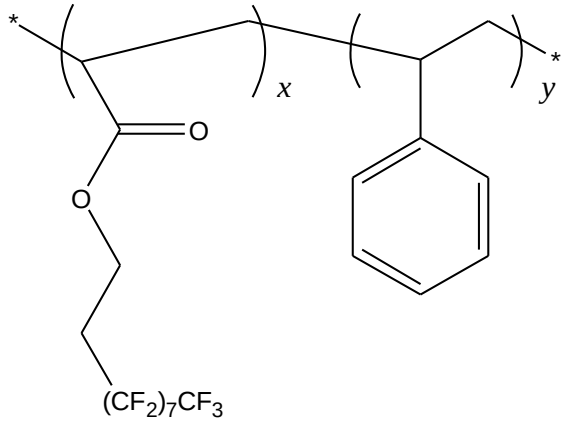

Fig. 1.3 – Chemical Structure of One Copolymer as CO_2 Thickener

The structure of the copolymer in Fig. 1.3 demonstrates the guideline for designing CO_2 thickeners. The fluoroacrylate unit serves as CO_2-philic component while the styrene unit serves as the intermolecular associating component to enhance viscosity.

This polymer was able to increase the viscosity of CO_2 by a factor of 8-6 at superficial velocity of 0.00035 to 0.0035 cm/s for a 1 wt % solution of the copolymer in CO_2.

However, fluoropolymers are not ideal for large quantity commercial production; the undegradable characteristics render this polymer an environmentally unfriendly one. To search for alternatives, Enick *et al*. identified poly(vinyl acetate) PVAc as the most CO_2 soluble, inexpensive, commodity polymer to viscosify CO_2. But the pressure required to dissolve an effective amount of PVAc in CO_2 was 6000-9000 psia, making it impractical for field application.

The frontier in CO_2 thickener research now is to screen for technologically and economically viable polymer basic structures and develop better cosolvent to enhance polymer solubility in CO_2 at lower pressure and temperature.

1.3.4.3 CO_2 Foam

CO_2 foam technology uses foam to reduce gas mobility in the reservoir. However, the control of foam generation and propagation in the field is the major challenge. CO_2 foam is not the focus of our research project because of its economic and technological issues. However, a brief review of this technology will be provided in this part.

Conventional foam generation with the surfactant injected with water was studied extensively. Usually, foam generation can be done using surfactant solution-alternating-gas injection (SAG) or co-injection. However, both have their limitations with respect to the placement of surfactant into theft zones and severe surfactant adsorption, particularly in carbonate reservoirs.

It is worth mentioning that conventional surfactants show very poor solubility in CO_2. To address this issue, CO_2-philic surfactants such as non-fluorinated AOT (sodium

bis(2-ethylhexyl)-sulfosuccinate) and non-ionic surfactants have been chosen for extensive testings.

Viet Q. Le *et al*. proposed a novel foam generation concept in which they dissolved surfactant directly in CO_2.[26] Foam generation occurred in-situ on combining with reservoir water. This can be particularly effective in blocking thief zones if they are sufficiently saturated with water to allow foaming process. The authors compared conventional SAG (surfactant in water alternated with CO_2), novel WAGS (water alternated with surfactant in CO_2) and novel CO_2 (continuous CO_2 dissolved surfactant injection). To utilize the benefit of miscible CO_2 displacement and improve injectivity, the novel CO_2 injection approach was developed without any water injection. Experimental results showed a surprisingly large pressure drop at the onset of CO_2 injection due to strong foam propagation in the core. Oil recovery with the novel CO_2 injection method (surfactant dissolved in CO_2 without any water) was as much as 60 % OOIP as compared to 51 % OOIP with novel WAGS and similar recovery with conventional SAG.

Huh *et al*. studied the mixing and flow behavior of a CO_2/surfactant-solution/oil system.[27] 2D flow-visualization experiments were conducted. To study the gas permeability reduction mechanism, different factors such as microscopic heterogeneity, presence of oil phase, surfactant concentration, and flow rate in secondary and tertiary miscible CO_2 floods were considered. When high pressure CO_2-foam was used as a blocking agent, factors such as CO_2 fluid diversion increased CO_2 sweep efficiency. Then the mobilization of bypassed oil was investigated. It was observed that foam subdivision and emulsification of the oil particles immobilized parts of the oil region and

flow blockage. However, the CO_2-foam performances were not evaluated at reservoir conditions.

Under more realistic temperature and pressure conditions, Wang reported that foams could only propagate for a short distance from inlet after the foam was in contact with oil.[28] CO_2-foam flood would be more effective for heterogeneous reservoirs with channels and highly conductive streaks. Better sweep efficiency was obtained with higher surfactant concentration and higher flow rates.

Liu *et al*. studied the influence of parameters on CO_2-foam stability and surfactant adsorption at reservoir conditions.[29] Different salinity, pH and surfactant concentrations were tested on the CO_2 foam.

Duyilemi *et al*. studied the CO_2-foam flooding of fractured carbonate oil reservoirs.[30] It was shown that CO_2-foam helped transportation of CO_2 from fracture to matrix and the macroscopic sweep efficiency of the CO_2 floods increased. A waterflood was conducted on the oil-saturated core prior to CO_2-foam flooding. The CO_2-foam flooding was intended as a tertiary oil recovery. It was suggested that foaming agent did not interfere with CO_2 diffusion to the matrix at reservoir condition, meaning that the foam might only affect the process of oil production from matrix to fracture to increase oil recovery.

1.3.5 CO_2 Flooding Visualization by CT-Scan

The first X-ray CT imaging technique was developed by Hounsfield in 1972.[31] CT-scanners can generate cross-sectional image slices through one object by revolving the X-ray tube around the object and obtain projections at different angles. CT images are displayed by assigning each pixel unit a value in Hounsfield unit. 3-D images can be

generated by taking small intervals of 2-D images around a constant axis. Details of CT imaging basic principles and the theories for CT image data processing are included in Chapter III.

Since then, CT-scanner has developed to the fourth-generation with fan-beam geometry with source rotating within a fix ring (gantry) of high efficiency detectors. For petroleum engineering applications, CT-scanner are often used to monitor acidizing wormholes, fluid saturation distribution. The resolution of CT-scan images can be 2 mm or less by detecting 0.1 % of attenuation differences.

The major advantage of using CT-scanner in CO_2 flooding experiments is that it has the ability to reconstruct the real-time cross-section and slab images. This dynamic feature can be applied to monitor CO_2 flood and the imaging results give us detailed information on viscous fingering, gravity segregation, miscibility, and mobility control.

Wellington and Vinegar[32] developed some pioneering work for the application of the CT-scan technique in petrophysics and reservoir engineering. Research topics such as three-dimensional (3D) measurement of density and porosity; rock mechanics; correlation of core logs with well logs; characterization of mud invasion, fractures, and disturbed cores were discussed in combination with the X-Ray computerized tomography technique. Fundamental studies of CO_2 displacement in cores were also discussed. A total of six tertiary CO_2 corefloods were carried out to study both immiscible and miscible displacements; capillary forces, viscous forces and gravitational forces were investigated together in control experiments. Iodododecane/Sotrol oil mixture were used as the oil phase. Iodododecane was used as a dopant for CT imaging while maintaining the same wettability property.

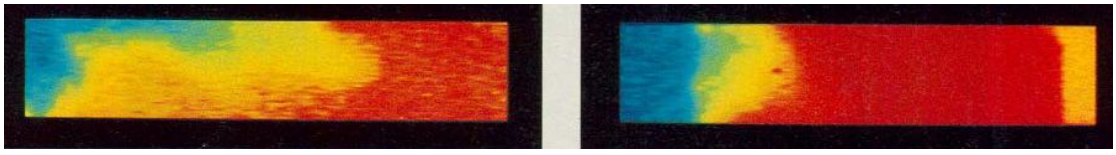

Fig. 1.4 – Comparison of WAG Front (Left) and CO_2 Foam Front (Right)

One Water Alternating Gas injection coreflood suggested that WAG could provide better horizontal sweep but could not prevent gravity segregation. A viscous-dominated miscible CO_2 flood was also tested and the results showed that viscosity increase by foam could diminish the gravity force segregation. It can be seen clearly by comparing the blue displacing fluid front in Fig. 1.4.

Uijttenhout *et al*. recently used CT scan to study the CO_2 foam rheology in sandstone cores.[33] Their goal was to observe CO_2 foam propagation in Bentheim sandstone cores. The injection sequence was described as Water Alternating Foam (WAF) with surfactants in aqueous phase. This was the first example of imaging post-foam liquid injection in CO_2 foam study. Dynamic foam and liquid displacement behavior inside the sandstone cores were analyzed by studying the CT-images. Since water was used as an alternating phase during the coreflood, variations of the CO_2 solubility in the liquid phase under different system pressures were observed; the foam flows under lower systems pressures tended to exhibit higher pressure drop across the core. The researchers also demonstrated that CO_2 foam effectively removed more residual oil from the reservoir comparing with normal CO_2 flood. The spiral CT-scan mode was used in their coreflood study. However, the coreflood cell temperature was not specifically controlled, which might cause some deviation of the CO_2 phase behavior from the real situation.

Schechter *et al.* utilized the CT-scan technique to study CO_2 flooding in fractured cores using WAG and polymer gel injection.[34] It is generally believed that fractured reservoirs are not very good candidates for CO_2 flooding because the fracture can conduct the injected CO_2 directly through the reservoir without sweeping the trapped oil. During the WAG coreflood experiments, water was viscosified using polymers so that CO_2 flow could be diverted into the matrix. A Guar gum and borate cross-linker gel was also used to counter the "leak-off" problem. All the coreflood fluid flows were visualized under CT-scan as shown in Fig. 1.5.

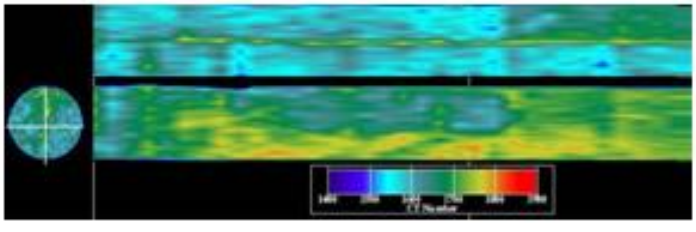

Fig. 1.5 – Visualization of CO_2 Fluid Flow in Fractured Core after Gel Treatment

During all the experiments, CO_2 was injected below MMP in the WAG process, simulating the immiscible flood process. These works provided the base for our continuing research on CO_2 flooding mobility control under different conditions.

1.4 Methodology

In our research of investigating CO_2 mobility control methods, the major technology we employed was the CT-scan imaging device. We designed and arranged a proper setup to combine the CT-scanner with our coreflood system. The integrated experimental system enabled us to visualize the fluid distribution and phase saturation

within the core at any specific injection intervals. Through the processing of the real time CT-data, we were also able to obtain both qualitative and quantitative experimental results such as CO_2 flood images and CO_2 saturation distribution curves.

The whole research project basically followed three major stages. During the first stage, the validity and accuracy of our integrated system were tested and some basic CO_2 flood experiments were carried out under both immiscible and miscible conditions. In the second stage of research, conformance control technique was applied to both sandstone and carbonate core samples. The effectiveness of conformance control was verified and the stability of cross-linked polymer gel was studied. In the third stage of research, a search for CO_2 viscosifier chemical was conducted and several chemicals were purchased to carry out viscosified CO_2 flood study. Pressure drop tests were used to compare the viscosity increase extents with different chemicals. CT-imaging for viscosified CO_2 flood experiments was utilized to confirm the difference between neat CO_2 flood and viscosified CO_2 flood.

CHAPTER II

EXPERIMENTAL SETUP

The two biggest components of the main experimental instrument setup are the CT-scanner and the coreflood system as will be explained in more detail in this section. Descriptions of core samples and chemicals used in the research are also included.

2.1 Instrument Setup

The coreflood experiments in this project are expected to represent both immiscible and miscible CO_2 flood scenarios. Temperature and pressure control of both the CO_2 fluid and coreflood cell is essential. Fig.2.1 shows the schematic of our experimental instrument setup. Tubings and fitting are all made of stainless steel ordered from Swagelok to withstand high temperature and pressure. Only the Production System uses plastic tubing from Nylaflow. Because this tubing is transparent, it helps us visualize and identify the effluent produced from the coreflood cell.

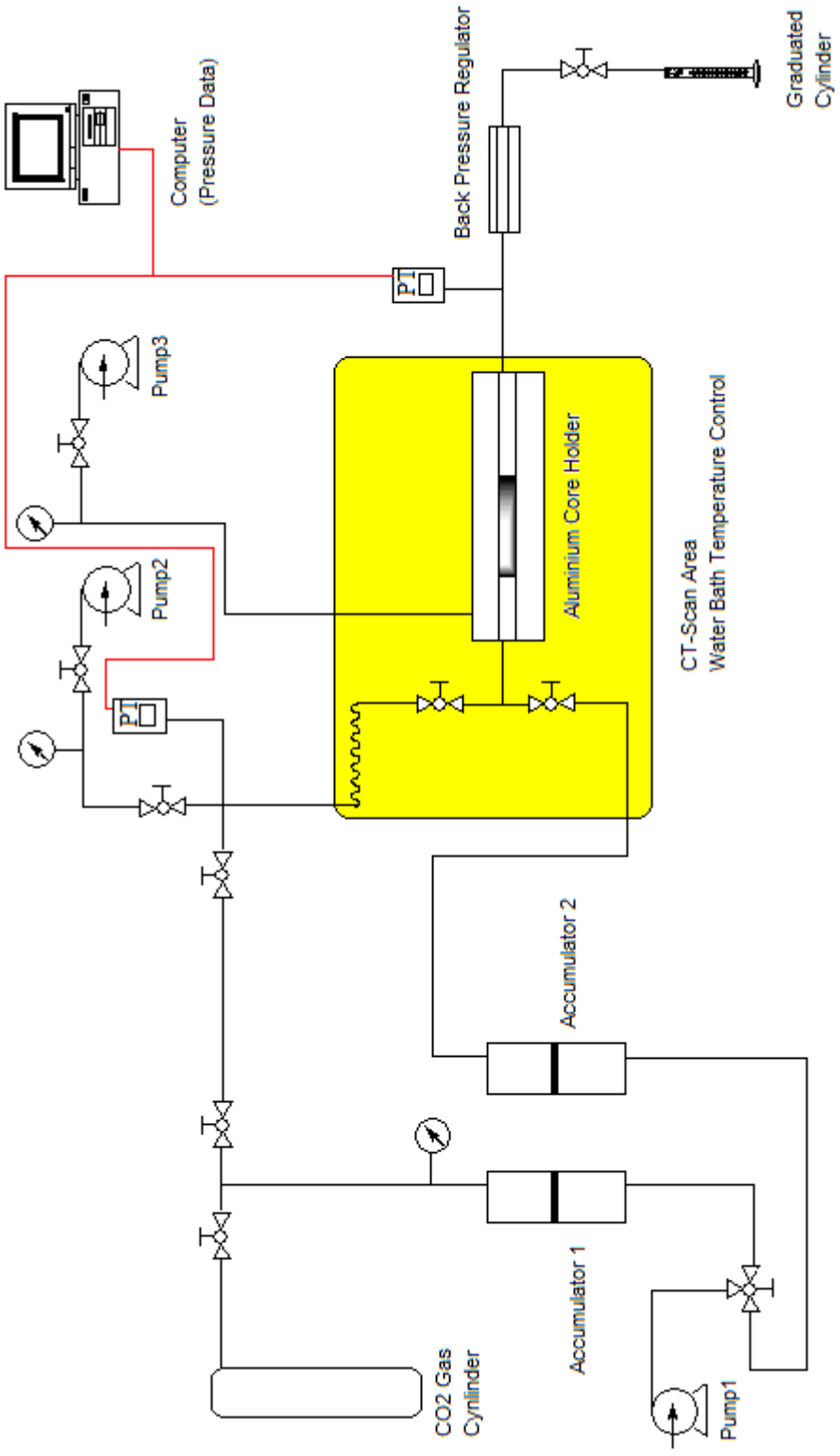

Fig. 2.1 – Schematic of Instrument Setup

The experimental instrument setup consists of five main components – the injection system, the coreflood cell, HD 200 X-Ray CT scanner, the production system and the data acquisition system. A brief description of each of the components is given below.

2.1.1 Injection System

The injection system consists of two accumulators and two pumps: Accumulator 1 is used to pressurize CO_2 and accumulator 2 is for brine or polymer gel during waterflood or gel placement experiments; pump 2 in Fig. 2.1 is used to saturated the core with Soltrol oil before any oil recovery experiment. Accumulator 1 is also used as a mixing cell for the preparation of viscosified CO_2. Both accumulator 1 and 2 are connected to an ISCO 5000 D syringe pump (Pump 1 in Fig. 2.1). Pump 1 is equipped with a programmable controller which is capable of running at a constant flow rate or at a constant pressure. Water is injected below the piston in the accumulator, increasing the pressure of the fluid above the piston to the desired level. A flow switching valve is used to inject either CO_2 or brine/gel into the coreflood cell.

2.1.2 Coreflood Cell

A 21-inches-long core holder made up of aluminum was used for use with the CT scanner. It is capable of holding cores up to 1 ft. in length and 1 in. in diameter. A viton Hassler sleeve surrounds the core and is secured to plungers at the ends of the core holder. The coreflood cell has an inlet for hydraulic oil that is used to apply overburden pressure. Hydraulic pump (Pump 3 in Fig. 2.1) is used to pressurize the cell by injecting hydraulic oil into the Hassler sleeve – an inner wall annulus pressure up to 7000 psi can be obtained in this manner. A waterbath tub is installed on the CT couch to heat the coreflood cell up to 130 °F.

2.1.3 X-Ray CT Scanner

The X-Ray CT scanner is a fourth generation Universal systems HD 200 system with a resolution of 0.3 mm x 0.3 mm. This scanner can be used to scan a maximum diameter of 48 cm with a maximum scan time of 4 sec per scan. Cross sectional images of the core sample are scanned at regular intervals during the experiment. The data obtained from the CT scanner is transferred and processed using VoxelCalc software. The cross sectional images can then be used for porosity and saturation determination or reconstructed for flow visualization.

2.1.4 Production System

The outlet end of the core holder is connected to a back pressure regulator which is used to increase pressure in the system. The produced fluid is collected in a graduated cylinder.

2.1.5 Data Acquisition System

Two pressure transducers one each at the inlet and the outlet are used in conjunction with an Omega OMB 55 data acquisition system. The pressures are read in real time from the PC connected to the DAQ. During the later stage of our research, the pressure transducers are upgraded to Omega digital pressure gauges which display the fluid pressure in real time.

2.2 Core Samples

Berea sandstone cores are used for coreflood experiments for the initial studies. Carbonate cores are drilled from outcrop rocks or field core samples for coreflood experiments. Generally, the core sample size is 1 inch in diameter and 5 inch in length.

The core samples can be classified as:

(1) Unfractured Berea Sandstone

(2) Horizontally and Vertically Fractured Berea Sandstone

(3) Horizontally Fractured Berea Sandstone

(4) Carbonate Sample I from Outcrop Limestone (Low porosity around 10%)

(5) Carbonate Sample II from Chevron Field Core Sample (High porosity around 20%)

2.3 Chemicals

The oil used in all experiments is Soltrol oil from Chevron Phillips. For conformance control experiments, polyacrylamide/chromium acetate gel chemical is used.

To enhance CT-image contrasts between phases, dopants were used in some cases. The dopant used for oil phase is 1-iodohexadecane from Acros Organic Chemical (10% by weight). The dopant used for polymer gel is KI (Sigma Aldrich) which was used in 6% aqueous solution.

CHAPTER III

EXPERIMENTAL CONDITIONS AND PROCEDURE

3.1 Background

The coreflood experiments were organized to focus on the study of CO_2 conformance control using both cross-linked polymer gels and CO_2 viscosifiers. Considering typical reservoir permeability heterogeneity in various field data, we carried out different coreflood runs in sandstones and carbonate to investigate possible scenarios of CO_2 fluid flow in reservoir conditions. The experiments are designed to address mainly the following issues: (1) eliminating heterogeneity of permeability in carbonate cores; (2) eliminating negative effect of fractures on CO_2 flood; (3) improving cross-linked gel stability at different reservoir conditions. (4) Testing the effectiveness of different CO_2 viscosifier chemicals.

3.2 Conformance Control Study on Gel Properties

Two key factors are vital for evaluation of the polymer gel properties: gelation time and gel strength.

Gelation time is usually defined as the time required for the viscosity of the gel system to reach twice the value before adding cross-linker. HPAM are partially hydrolyzed during commercial production so that there could be effective coordinate bonding between the carboxylate functional groups on the polymer chains and the Cr (III) cations. This coordinate bonding reaction is the base of cross-linking mechanism:

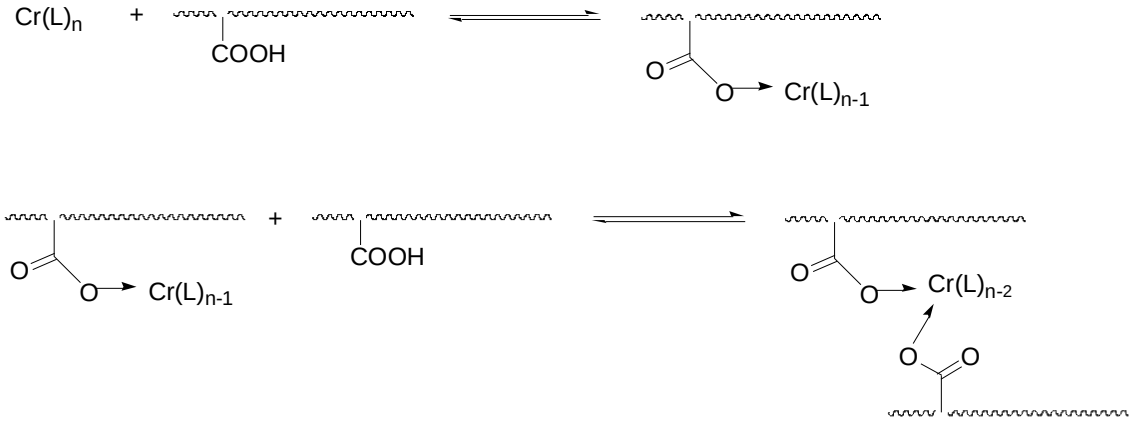

Fig. 3.1 – Cross-linking Reaction of the HPAM Polymer Gel

It has been suggested that the reaction is first order in polymer and first order for the cross-linker; making the overall reaction second order. The reaction mechanisms are shown in Fig. 3.1.

Several factors affect the gelation time. The acetate anion in the $Cr(OAc)_3$ cross-linker usually makes the gelation time longer compared to inorganic Chromium salts such as $CrCl_3$. Increasing polymer concentration accelerates gelation process while increasing polymer to cross-linker ratio slows down gelation process. Because $Cr(OAc)_3$ is used for many on-site application, we have chosen $Cr(OAc)_3$ as the cross-linker to test in coreflood experiments.

Because salinity of the solution is known to have no apparent influences on the gel properties, we added KI as an dopant in HPAM/Cr(III) acetate polymer gel to produce more distinguishable CAT-scan images.

Gel strength can be quantitatively measured from viscoelastic properties, but these methodologies usually cannot predict the performance of gel system in the actual oil field. Generally, for pre-formed cross-linked gels, the gel strength decreases as the gel

moves further into the reservoir while for in-situ formed gels, the gel strength increases as the gel moves further into the reservoir.

Other issues might also affect the gelation time and gel strength such as the presence of divalent cations (Ca^{2+}, Mg^{2+}) or the reservoir temperature. These issues should be analyzed according to the actual reservoir conditions.

So far there is no widely applicable methodology to predict the performance of gels in the reservoir. In our research project, CAT-Scan technique is employed to visualize the distribution of gel in the cores during the CO_2 flooding process.

In our research on the application of HPAM/$Cr(OAc)_3$ polymer gel in CO_2 flooding, some of the concentration ranges in Table 3.1 were tested on carbonate and sandstone cores to simulate reservoir conditions.

Table 3.1 – Typical Concentrations HPAM/$Cr(OAc)_3$ Polymer Gel System

Polymer Active Weight Loading/ppm	Chrome Acetate Polymer wt/$Cr(OAc)_3$ wt	Active Chromium Polymer wt/Cr(III) wt
3000-4500	10	44
4500-7000	12.5	55
7000-8500	15	66
8500-17000	17.5	77

3.3 Study of Viscosifier Application in CO_2 Flooding

A market survey was conducted to select among potential CO_2 viscosifier chemicals. Some of the industrial siloxane polymers used in the early research from Chevron are no longer available; these polymers were only tested for research purposes and no field application was carried out. However, we managed to find other possible substitute

industrial polymers in supply. The details of the viscosifier chemicals are provided in this section.

Research Lab Chemicals:

Two major potential candidates for CO_2 viscosifier were Polyvinylacetate (PVAc) and Polydimethylsiloxane. These two compounds are high molecular weight chemicals which can increase CO_2 viscosity significantly. These two commercially available research lab chemicals were purchased from Acros Organic and Alfa Aesar, respectively. Their properties are specified as following.

(1) Dodecamethylpentasiloxane

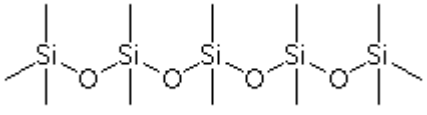

Fig. 3.2 – Chemical Structure of Dodecamethylpentasiloxane

Dodecamethylpentasiloxane (CAS Number: 141-63-9) has the molecular formula $C_{12}H_{36}O_4Si_5$ and a molecular weight of 384.84. The chemical structure is shown in Fig. 3.2. This chemical contains a repetition of dimethylsiloxane unit which is an effective functional unit to viscosify CO_2 fluid. Although the structure only contains a limited number of dimethylsiloxane units; experiments with this basic structure should yield information on the effectiveness of adding CO_2 viscosifying functionalities to the backbone of the viscosifier chemical.

(2) PVAc (Poly (vinyl acetate))

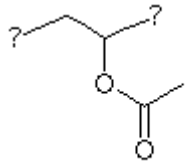

Fig. 3.3 – Repeating Unit of PVAc

Poly (vinyl acetate) (CAS Number: 9003-20-7) used in our research has the molecular formula $(C_4H_6O_2)_n$ and a molecular weight of 170,000 (average). The chemical structure is shown in Fig. 3.3. PVAc is a readily available, cheap commercial polymer. We carried out a literature survey on different commercial polymers and PVAc was recommended as the most practical CO_2 viscosifying chemical. Although a relatively high miscibility pressure is required for PVAc polymer to dissolve in the CO_2 fluid, most of the potential CO_2 flooding fields have high reservoir pressure which can aid in increasing the solubility of viscosifiers in CO_2 fluids. Also, previous viscosity tests on PVAc polymer were based on only PVAc and CO_2 mixture; we added a 10% cosolvent toluene in our coreflood experiment which, we expected, would greatly enhance the solubility of PVAc in CO_2.

(3) Polydimethylsiloxane, trimethylsiloxy terminated.

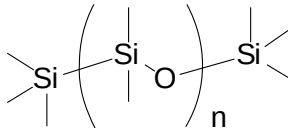

Fig. 3.4 – Repeating Unit of Polydimethylsiloxane, Trimethylsiloxy Terminated

Polydimethylsiloxane (CAS Number: 9016-00-6) used in our research has the molecular formula $(C_2H_6SiO)_n$ and a molecular weight of 139,000 (average). The chemical structure is shown in Fig. 3.4. Polydimethylsiloxane itself is already a pretty viscous material even before adding to toluene cosolvent and CO_2. Its viscosity is around 100,000 centistokes. However, the market price of this chemical prohibits its actual use in field applications. In our research we purchased 4 kg of polydimethylsiloxane for $ 417.00. It is important to note that industrial siloxane polymers with similar structures are marketed at a much lower price.

Industrial Chemical:

We carried out an extensive market search of proper CO_2 viscosifiers to be purchased in large quantities. One brand of polymer product from Dow-Corning was the most promising chemical: XIAMETER(R) PMX-200 SILICONE FLUID 600000CS.

Dow-Corning products are mainly silicone polymers and the major composition of the chemical is polydimethylsiloxane; the structural feature of repeating dimethylsiloxane follows the guideline of choosing effective CO_2 viscosifier. A series of the XIAMETER® product can be obtained with a range of different viscosities with very high range from 100,000 c St to 600,000 c St. This polymer has great potential when

used in conjunction with toluene cosolvent to enhance the solubility of the polymer materials and increase CO_2 viscosity. We tried to contact the industrial chemical companies requesting samples for our study but were not successful in obtaining them. However, the above information is worth looking into for possible large scale application in future.

To carry out viscosified CO_2 flooding, we followed a fixed routine to prepare the polymer / CO_2 fluid mixture. The viscosified CO_2 mixture fluid used in our coreflood experiments were composed of 5% viscosifier, 10% cosolvent, and 85% CO_2 by weight. In the following section, typical procedures for the preparation of PVAc viscosified CO_2 in the lab are described. Preparations with other viscosifiers followed similar procedures.

(1) Preparation of chemical solution:

10 g of solid PVAc beads were mixed with 20 g of Toluene cosolvent; the mixture was stirred overnight to get a homogeneous solution. All PVAc polymer beads were dissolved in the cosolvent to form a viscous solution.

(2) Introduction of viscosifiers:

The viscous solution was poured into the accumulator; then the accumulator was sealed and 500 psi CO_2 was injected into the accumulator. The weight of CO_2 was calculated to ensure that the PVAc polymer was 5% of the total weight and the toluene cosolvent was 10% of the total weight.

(3) Dissolution of viscosifiers:

The accumulator was pressurized by pump to reach 2000 psi pressure. As CO_2 shrinks in volume, significant heat was generated from the dissolution of viscosifier in CO_2. The mixture was left to equilibrize before injecting into the core.

3.4 Data Processing

X-ray linear attenuation coefficient μ can be expressed as:

$$\mu = \rho\left[\sigma(E) + b\frac{Z_e^{3.8}}{E^{3.2}}\right] \quad \text{.....(3.1)}$$

ρ= electron density

σ (E)= Klein-Nishina coefficient

b= constant($= 9.8\times10^{24}$)

Z= the atomic number of the chemical species

E= the X-ray photon energy in kEV

As can be seen from equation 3.1, the coefficient magnitude is affected by the atomic number and that is the base for X-ray imaging dopant addition.

The above μ value is measured in Hounsfield units (HU):

$$HU = 1000\times\left(\frac{\mu}{\mu_w} - 1\right) \quad \text{.....(3.2)}$$

μ_w=X-ray linear attenuation coefficient for water

During most of X-ray imaging processing applications, a simplified linear basic assumption is derived from the definition to correlate the density of the material at a pixel with the average CT number at the same pixel.

For each pixel in a CT image:

$$Density = A * \mathrm{CT} + B \quad \text{.....(3.3)}$$

Density= density at the selected pixel

CT= CT number of the selected pixel

A,*B*= constants

Each pixel of reconstructed CT-image has a corresponding CT-number. By approximation this number is in a linear relationship with the average density of the substances in the pixel. The linear relationship enables the average CT number to be a weighed mean from the CT numbers and percentages of pure substances present in the pixel.

CT data can be widely applied to find out porosity and phase saturation quantitatively.

3.4.1 Porosity Calculation

In this section, we will take a typical dry sandstone core exposed in air as an example to derive porosity step by step: In order to do so, the following equation is established first according to mass conservation:

$$\rho_{\text{average}} V_0 = \rho_{\text{air}} * V_0 * a\% + \rho_{\text{matrix}} * V_0 * b\% \quad (3.4)$$

ρ_{average}= the average density at the pixel

ρ_{air} = the density of air

ρ_{matrix} = the density of the sandstone matrix (Assuming sandstone matrix has a uniform distribution of density.)

V_0= volume of the pixel region

$a\%$ = the percentage of air content in the pixel by volume

$b\%$ = the percentage of solid matrix content in the pixel by volume

Here we assume the sandstone is completely dry and only air is present in the pore space. ($a\% + b\% = 1$) An illustration is provided in Fig. 3.5.

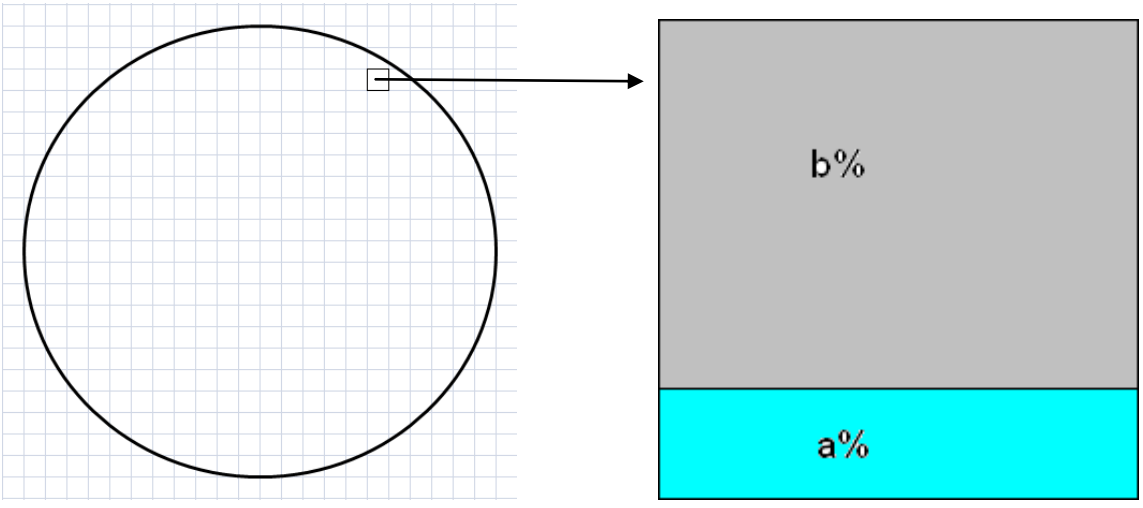

Fig. 3.5 – Illustration of CT Image Pixel Content Analysis

Assuming a dry sandstone core sample is scanned, we can plug in the linear relationship from equation 3.3 to obtain the following equation:

$$(A * \mathrm{CT(pixel)} + B) * V_0 = (A * \mathrm{CT(air)} + B) * V_0 * a\% + (A * \mathrm{CT(matrix)} + B) * V_0 * b\% \quad \text{.....(3.5)}$$

CT(pixel) = average CT number obtained from CT image

CT(air) = CT number of air (-1000)

CT(matrix) = CT number of the matrix content (Assuming sandstone matrix has a uniform distribution of density.)

Simplifying Equation 3.5, we have the following equation for any pixel within the sandstone core CT image:

$$\mathrm{CT(pixel)} = a\% * \mathrm{CT(air)} + b\% * \mathrm{CT(matrix)} \quad \text{.....(3.6)}$$

Ideally, $a\%$ should be equal to the porosity of this pixel. However, to find out porosity from equation 3.5, the matrix CT number is necessary. It is usually unrealistic to measure the average matrix CT number because of the heterogeneity of the matrix and variations between different cores. In order to obtain porosity, we assume this same sandstone core is further processed and saturated with water (brine) displacing all the air in the pore space. We can obtain another linear relationship as:

$$\mathrm{CT(pixel)}' = a\% * \mathrm{CT(brine)} + b\% * \mathrm{CT(matrix)} \quad (3.7)$$

CT(brine) = CT number of brine (0)

Here we assume all the pore space is filled with water and the presence of air is neglected.

If there are n pixels in one CT slice image, for one slice of core image we have:

$$\mathrm{CT(slice)} = \sum_{i=1}^{n} \mathrm{CT(pixel)}/n \quad (3.8)$$

CT(slice) = average CT number of the slice image

If we integrate and add up every pixel within one single slice for equation 3.6 and equation 3.7, we can obtain the following:

$$\sum_{i=1}^{n} \mathrm{CT(pixel)} = \sum_{\mathrm{i}=1}^{\mathrm{n}} a_{\mathrm{i}}\% * \mathrm{CT(air)} + \sum_{\mathrm{i}=1}^{\mathrm{n}} b_{\mathrm{i}}\% * \mathrm{CT(matrix)} \quad (3.9)$$

$$\sum_{i=1}^{n} \mathrm{CT(pixel)}' = \sum_{\mathrm{i}=1}^{\mathrm{n}} a_{\mathrm{i}}\% * \mathrm{CT(brine)} + \sum_{\mathrm{i}=1}^{\mathrm{n}} b_{\mathrm{i}}\% * \mathrm{CT(matrix)} \quad (3.10)$$

Substracting Eq.3.9 from Eq.3.10 and dividing by n, we have:

$$\left(\sum_{i=1}^{n} \mathrm{CT(pixel)}' - \sum_{i=1}^{n} \mathrm{CT(pixel)}\right)/n =$$

$$\left(\sum_{\mathrm{i}=1}^{\mathrm{n}} a_{\mathrm{i}}\% * (\mathrm{CT(brine)} - \mathrm{CT(air)})\right)/n \quad (3.11)$$

Naturally the average porosity of the slice will be calculated as:

$$\emptyset = \sum_{\mathrm{i}=1}^{\mathrm{n}} a_{\mathrm{i}}\%/n \quad (3.12)$$

Combining 3.8, 3.11 and 3.12, we will have the final equation to calculate the porosity of one slice of CT image:

$$\emptyset = (\mathrm{CT(slice)}' - \mathrm{CT(slice)})/(\mathrm{CT(brine)} - \mathrm{CT(air)}) \quad (3.13)$$

3.4.2 Phase Saturation Calculation

In the following section, we discuss two ways to calculate phase saturation using CO_2 displacing oil as an example.

In the case of CO_2 displacing oil, if only CO_2 and oil phases occupy effective pore spaces, we can quantitatively calculate CO_2 and oil phase saturations from a series of CT data.

Before CO_2 flood, suppose the core plug is fully saturated by CO_2, then for one pixel of CT image we will have:

$$\mathrm{CT(pixel)1} = a\%\mathrm{CT(CO2)} + b\%\mathrm{CT(matrix)} \quad (3.14)$$

a% = the percentage of CO_2 content in the pixel by volume

b% = the percentage of solid matrix content in the pixel by volume

CT(pixel)1 = average CT number obtained from CT image

CT(CO2) = CT number of CO_2

CT(matrix) = CT number of the matrix content

Assuming that the same pixel is fully saturated with oil, we have:

$$\mathrm{CT(pixel)2} = a\%\mathrm{CT(oil)} + b\%\mathrm{CT(matrix)} \quad (3.15)$$

CT(pixel)2 = average CT number obtained from CT image

CT(oil) = CT number of oil

After CO_2 flood started, the pore space is occupied by both CO_2 and oil. Then we can establish the following equation:

$$\mathrm{CT(pixel)3} = c\%\mathrm{CT(oil)} + d\%\mathrm{CT(CO2)} + b\%\mathrm{CT(matrix)} \quad \text{.....(3.16)}$$

CT(pixel)3 = average CT number obtained from CT image

$c\%$ = the percentage of oil content in the pixel by volume during CO_2 flood

$d\%$ = the percentage of CO_2 content in the pixel by volume during CO_2 flood

$a\% = c\% + d\%$

Again, we take the sum of the pixels and use average slice CT number of each slice from the data generated from CT-scanner.

We then substract Eq.3.16 from Eq.3.15::

$$\sum_{i=1}^{n} \mathrm{CT(pixel)2} - \sum_{i=1}^{n} \mathrm{CT(pixel)3} = \sum_{i=1}^{n}(a_i - c_i)\%\ \mathrm{CT(oil)} - \sum_{i=1}^{n} d_i\%\,\mathrm{CT(CO2)} \quad \text{.....(3.17)}$$

Since $d_i = a_i - c_i$,

$$\mathrm{CT}(slice) = \sum_{i=1}^{n} \mathrm{CT(pixel)}/n \quad \text{..... (3.8)}$$

We can rearrange 3.17 to get:

$$(\sum_{i=1}^{n} d_i\%)/n = (\mathrm{CT(slice)2} - \mathrm{CT(slice)3})/(\mathrm{CT(oil)} - \mathrm{CT(CO2)}) \quad \text{.....(3.18)}$$

The average CO_2 saturation for one slice can be expressed as:

$$S_{\mathrm{CO2}} = \sum_{i=1}^{n} d_i\%/\sum_{i=1}^{n} a_i\% = \sum_{i=1}^{n} d_i\%/(\emptyset n) \quad \text{.....(3.19)}$$

$\emptyset$ = the average porosity of the slice

Combining 3.18 and 3.19, we arrive at the final equation for CO_2 saturation:

$$S_{\mathrm{CO2}} = (\mathrm{CT(slice)2} - \mathrm{CT(slice)3})/(\emptyset(\mathrm{CT(oil)} - \mathrm{CT(CO2)})) \quad \text{.....(3.20)}$$

One problem with equation 3.20 is that it is difficult to obtain a good average CT number for oil and CO_2. To circumvent this problem we can use equation 3.14. Assume average slice CT number for fully CO_2 saturated image is CT(slice)1, then we have:

$$S_{CO2} = 100\% = (\mathrm{CT(slice)2} - \mathrm{CT(slice)1})/(\emptyset(\mathrm{CT(oil)} - \mathrm{CT(CO2)})) \quad \text{.....(3.21)}$$

Combining 3.20 and 3.21, we have:

$$S_{CO2} = (\mathrm{CT(slice)2} - \mathrm{CT(slice)3})/(\mathrm{CT(slice)2} - \mathrm{CT(slice)1}) \quad \text{.....(3.22)}$$

Equation 3.22 is more suitable for phase saturation calculation since it avoids the use of average CT number for pure substances. One extra step of saturating the whole core with CO_2 is necessary to set up a standard CT(slice)1. It is worth mentioning that adding dopant to oil is necessary to increase the accuracy of calculation. The more dopant is added, the bigger the difference is between CT(slice)2 and CT(slice)1, resulting in a bigger denominator that allows for more accuracy in the final calculation.

3.5 Typical Experimental Procedures

General experimental procedures for CO_2 coreflood experiments are provided as following.

1) Core is heated in an oven and then weighed.
2) The dry core is placed into the coreholder with confining pressure and scanned.
3) CO_2 is flooded through the dry core to achieve 100 % CO_2 saturation. (at the experimental pressure and temperature condition) Then the CO_2 saturated core is CT-scanned.
4) The dry core is flooded with oil. At least 15 PV (approximately 150 ml for sandstone cores) oil is used to flush the core. The oil saturated core is then CT-scanned.

5) CO_2 injection is started at 0.5 ml/min using the injection pump while recovery data and pressure data are collected. CT-scans are performed at different time intervals during the CO_2 flood.
6) For gel placement, gel is injected into the front part of the core. CT-scans are performed before and after gel injection.
7) For CO_2flooding after gel placement, the core is finally CO_2 flooded one day after the gel is injected. CT-Scans are taken at different time intervals.
8) For viscosified CO_2, viscosified CO_2 solution is prepared in the accumulator beforehand and is used for CO_2 flood.

CHAPTER IV

EXPERIMENTAL RESULTS AND DISCUSSION

Laboratory study results from all coreflood experiments in the project are specified in the following sections. The major technique we use is CT-scanning imaging. This technology enables us to visualize the real-time fluid flow in a coreflood experiment. We can also process CT-imaging data quantitatively with designed sequences of fluid injection.

Most of the experimental procedures are similar to the protocols described above. However, for clarifications, specific experimental conditions are mentioned for each case of coreflood experiment in the following sections.

4.1 Porosity Measurement

To prepare for the coreflood experiment, 10 Berea sandstone cores (sample bs-01 to bs-11) were tested for their porosity distribution. The purpose of this test was to verify the quantitative feature of CT image data. We were also interested in comparing the two porosity measurement techniques: CT scan and weight difference.

The two techniques for the porosity measurement can be summarized as:

(1) CT number difference between dry core and brine saturated core

(2) Weight difference between dry core and brine saturated core

Before experiment, all core sizes were measured (diameter and length). The dry cores were prepared by heating Berea sandstone cores in the oven overnight. After the dry cores were scanned and weighed, they were immersed into a brine solution and a

vacuum was applied over the brine solution. The vacuum condition was kept overnight to ensure that almost all air in the core is displaced by brine. The brine saturated core was then scanned and weighed.

The images were processed using a color spectrum from 1500 to 2200 as shown below; different CT numbers on the image were assigned different colors according to the spectrum in Fig. 4.1.

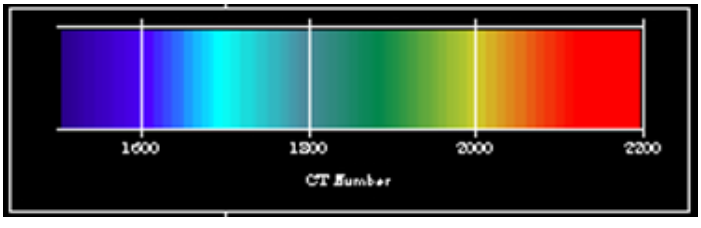

Fig. 4.1 – Color Spectrum (CT number 1500~2200) for CT Images in Section 4.1

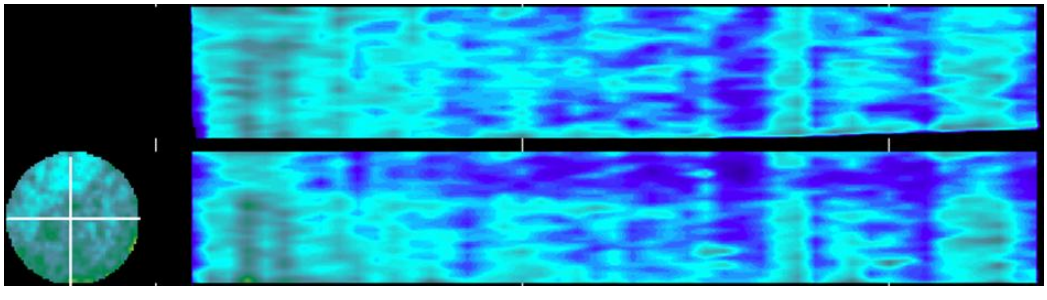

Fig. 4.2 – Dry Sandstone Core CT Image (The upper slab is the horizontal cross-section image and the lower slab is the vertical cross-section image)

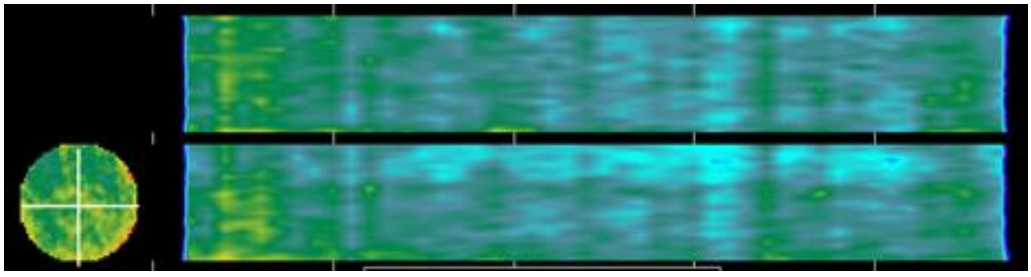

Fig. 4.3 – Brine Saturated Sandstone Core CT Image (The upper slab is the horizontal cross-section image and the lower slab is the vertical cross-section image)

Fig. 4.2 and Fig. 4.3 are presented to show a CT image comparison of dry sandstone core and brine saturated sandstone core (sample bs-01).

It can be seen that after brine (CT number=0) has displaced air (CT number=-1000) in the pore space, the average CT-numbers increased significantly. It is reflected by the color shift of blue in dry core towards green in brine saturated core.

The porosity measurement results are listed in the Table 4.1 below:

Table 4.1 – Porosity Measurement Result for Berea Sandstone

Core Sample Name	Effective Porosity	CT Number Calculated Porosity
bs-1	0.183964166	0.248586087
bs-3	0.183987622	0.185196222
bs-4	0.185802187	0.161658
bs-5	0.183796027	0.211015641
bs-6	0.184276731	0.210974222
bs-7	0.184930461	0.239951333
bs-8	0.184514152	0.187720455
bs-9	0.184719038	0.170536
bs-10	0.184292036	0.165232667
bs-11	0.182840792	0.191072273
Average	**0.184312321**	**0.185425685**

Effective Porosity is calculated from the weight difference between dry core and brine saturated core. CT number calculated porosity is obtained from equation 3.13.

The porosity values obtained from CT measurement can be used to construct a Normal Probability Plot in Fig. 4.4:

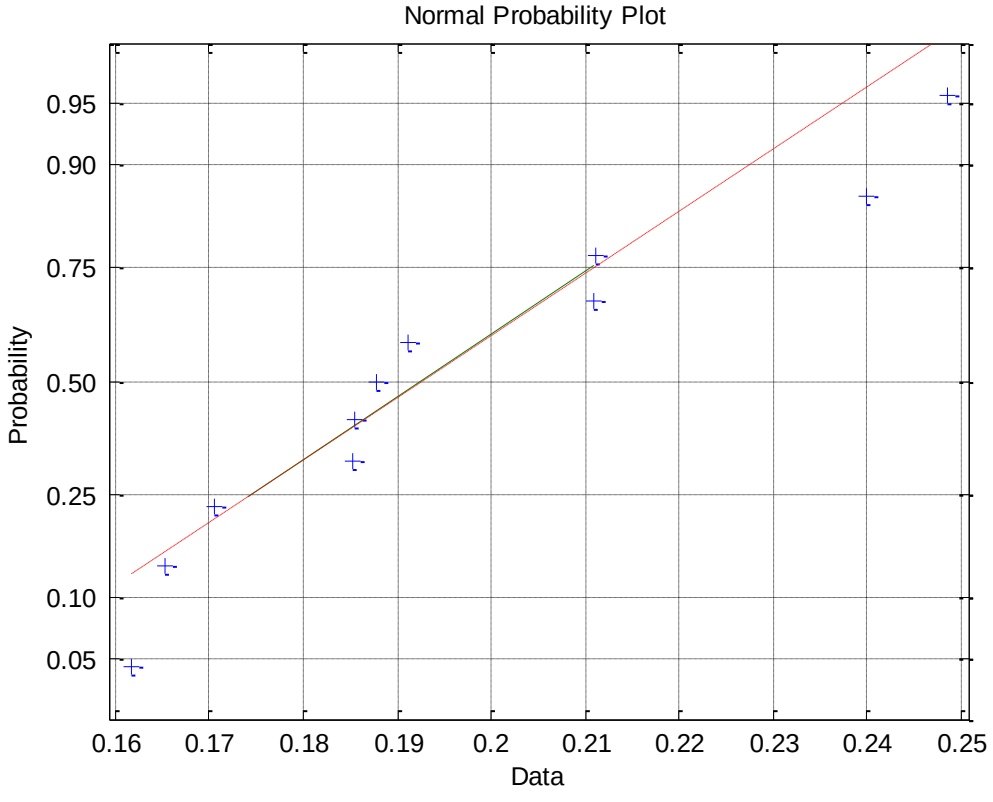

Fig.4.4 – Normal Probability Plot Examination for CT Measured Porosity

The porosity measurement results show that CT measured porosity of the Berea sandstone cores follows an approximate normal distribution. The average porosity values obtained from two different methods are very close to each other (0.1843 and 0.1854). The validity of using CT for quantitative calculation could be confirmed by these

experimental results. We can determine pore volume (PV) of fluid injected into the sandstone cores using the average porosity of 0.185 in our future coreflood experiments.

4.2 Experiments in Unfractured Sandstone

CO_2 flooding in unfractured sandstone was studied first to obtain preliminary understanding of ideal conditions. We have accomplished CO_2 flooding both above and below MMP.

CO_2 flooding below MMP experiment details can be summarized as following. Before coreflood experiment, the core was prepared according to the standard procedures provided in the last section: The core was first oven heated and weighed and then the sandstone core was saturated with brine under vacuum and was left over night. The brine-saturated core was placed in the core holder with a confining pressure of 2000 psi and under temperature of 70 °F. Then oil was injected into the brine-saturated core to perform a water drainage process in order to establish irreducible water saturation and OOIP (original oil in place) oil saturation. The CO_2 fluid was injected into the oil-saturated core at 800 psi. Injection rate was kept at 2 ml/min (CO_2 is predicted to be in liquid state at 800 psi and 70 °F).

CO_2 flooding above MMP experiment details can be summarized as following. Experimental conditions were designed to ensure that the CO_2 fluid would be at supercritical state. MMP (minimal miscible pressure) was calculated beforehand and the experimental CO_2 injection pressure was set at well above the predicted MMP value.

MMP calculation was carried out according to the Cronquist correlation (Equation 1.7), the MMP was determined to be 1333 psi at 120˚F with our light oil (*Mw* 122).

The experimental conditions were set to be 1500 psi for CO_2 injection pressure and 120 °F for water bath temperature. Before coreflood experiment, the core was first oven heated and weighed. Then, the sandstone core was saturated with brine in vacuum and was left over night. The brine-saturated core was placed in the core holder with a confining pressure of 4000 psi and under temperature of 170 °F. Then oil was injected into the brine-saturated core to perform a water drainage process in order to establish irreducible water saturation and OOIP (original oil in place) oil saturation. The supercritical CO_2 fluid was injected into the oil-saturated core at 1500 psi. Injection rate was kept at 2 ml/min. (CO_2 is predicted to be in supercritical state at 1500 psi and 120 °F.) The recovery data is shown in Fig. 4.5:

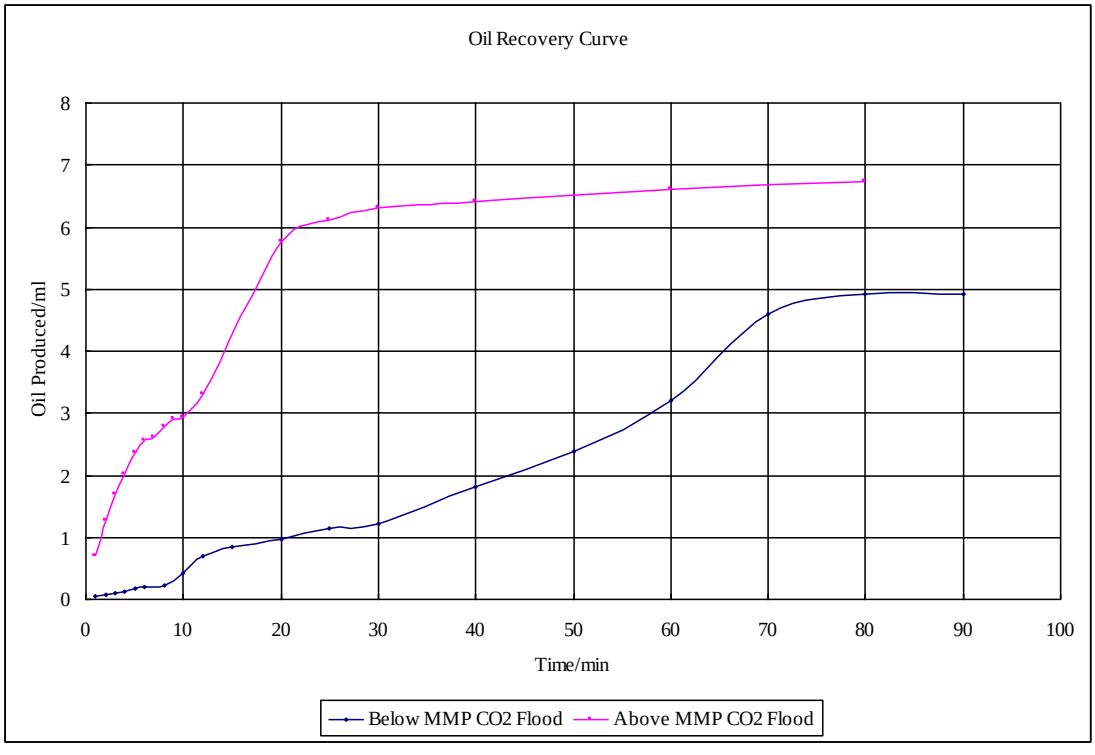

Fig. 4.5 – Below and Above MMP CO_2 Flood Recovery Curve

Original Oil in Place (OOIP) for the cores in both experiments is estimated to be 8.95 ml. The two sandstone cores have the same pore volume thus we can compare the volume of oil produced as it is in a linear relationship with the oil recovery factor (RF). It is shown from the recovery data that above MMP CO_2 flood shows a higher oil production rate with time compared to the below MMP CO_2 flood; it can also be seen that above MMP CO_2 flood gives a higher overall oil recovery. The CT-scan images were also obtained at different times of the coreflood experiment. They have provide details on the fluid distribution in the sandstone cores; we observed that in the above MMP CO_2 flood case greater miscibility between CO_2 phase and oil phase have been achieved.

4.3 Experiment in Fractured Sandstone

The frequent presence of fractures in reservoirs usually brings in complication for the CO_2 flooding project design. We decided to study the effects of fractures on CO_2 flooding in sandstones to provide practical information for the further mobility control study.

To give a negative example of CO_2 flooding in untreated fractured reservoir; we carried out the corresponding coreflood experiment. The experimental results show that relatively low CO_2 saturation was established at the end of the coreflood and oil recovery is significantly lower compared to CO_2 flooding in unfractured sandstone.

Before coreflood experiment, the core was prepared according to the standard procedures provided: The core was first oven heated and weighed. Then, the sandstone core was saturated with brine in vacuum and was left over night. The brine-saturated core was placed in the core holder with a confining pressure of 2000 psi and under

temperature of 70 °F. Then oil was injected into the brine-saturated core to perform a water drainage process in order to establish irreducible water saturation and OOIP (original oil in place) oil saturation. The CO_2 fluid was injected into the oil-saturated core at 800 psi. Injection rate was kept at 2 ml/min (CO_2 is predicted to be in liquid state at 800 psi and 70 ℉).

The CT image color spectrum is shown in Fig. 4.6.

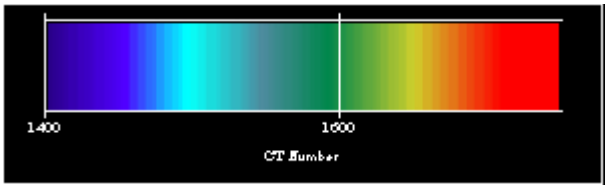

Fig. 4.6 – Color Spectrum (CT number 1400~1750) for CT Images in Section 4.3

In Fig. 4.7 below, the upper slab is the horizontal cross section of the core while the lower slab is the vertical cross section of the core. These images are reconstructed from 2 mm interval multiple cross scans of the core. The fluid flow direction is always from right to left. The description above applies to all the cross section images shown in the thesis.

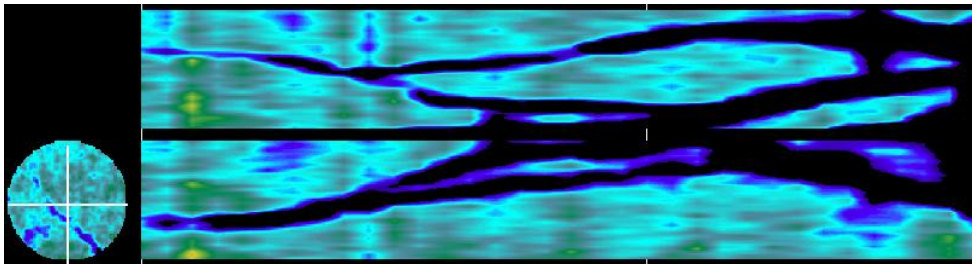

Fig. 4.7 – Scan of 100% CO_2 Saturated Fractured Sandstone Core

CO_2 has relatively low CT number and the overall color tone is blue. Dark blue color close to fractures suggests higher concentration of CO_2. The completely dark regions are filled with CO_2 fluid; the CT number of these regions is not within our color spectrum range thus no color is assigned.

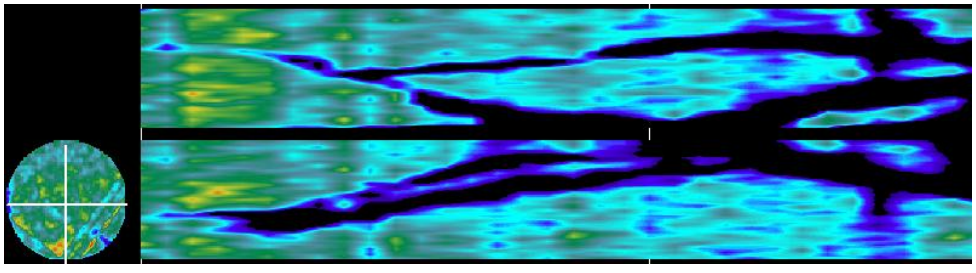

Fig. 4.8 – Scan of 100% Brine Saturated Fractured Sandstone Core

Brine also has very low CT number and the overall color tone is again blue in Fig. 4.8. Dark blue color close to fractures suggests higher concentration of brine. The completely dark regions are filled with brine; the CT number of these regions is again not within our spectrum range.

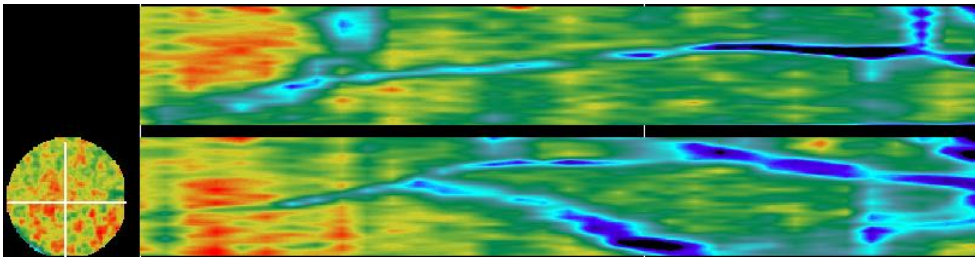

Fig. 4.9 – Scan at OOIP Oil Saturation after Oil Injection/Water Drainage Process

When oil was replacing brine the whole color tone in Fig. 4.9 shifted to the red end of the spectrum. The oil used here had an approximate CT number of 650 compared to the

low CT number of brine (CT = 0). This significant CT difference caused the average CT number resulting in the color shift.

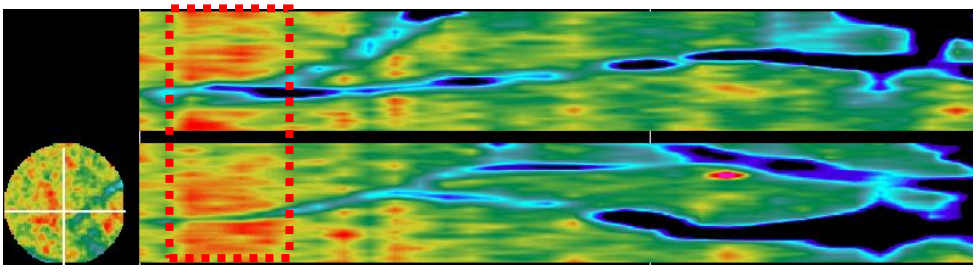

Fig. 4.10 – Scan 1 after the Start of the CO_2 Flooding

As shown in Fig. 4.10, at 5 min CO_2 already had a breakthrough from the core. In fractured reservoirs CO_2 fluid flowed through the fracture pathway almost instantaneously. There are more completely dark regions in the slab image, indicating aggregation of liqueous CO_2 fluid.

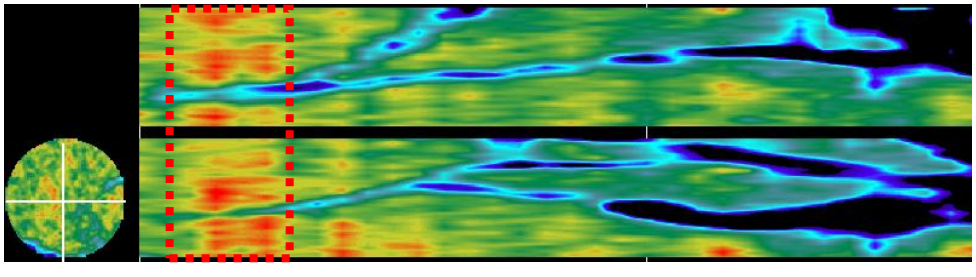

Fig. 4.11 – Scan 2 after the Start of the CO_2 Flooding

After 15 min, the matrix regions containing oil changed in color slightly as can be seen in Fig. 4.11. In the dashed red line rectangle region specified within the core image, the red color spots have decreased, suggesting displacement of oil by CO_2.

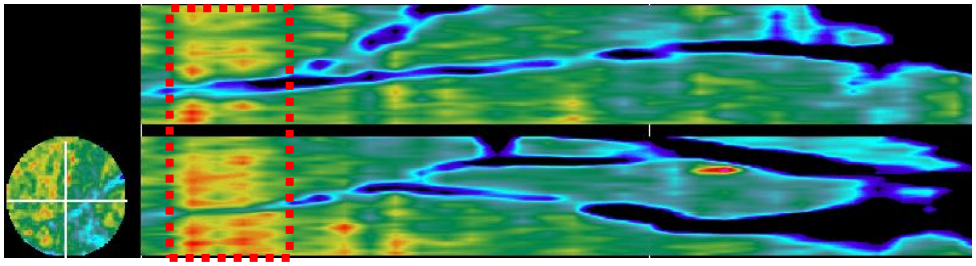

Fig. 4.12 – Scan 3 after the Start of the CO_2 Flooding

CT image at 50 min (Fig. 4.12) indicates that the whole core has a darker color compared to the 5 min image and 15 min image. However, the color change is still not very significant because most of the CO_2 is just flowing along the fractures without entering and affecting the matrix.

The average slice CT numbers of each scan were processed quantitatively and a CO_2 saturation profile was constructed and shown in Fig. 4.13; the CO_2 flow direction is shown by the arrow in the plot:

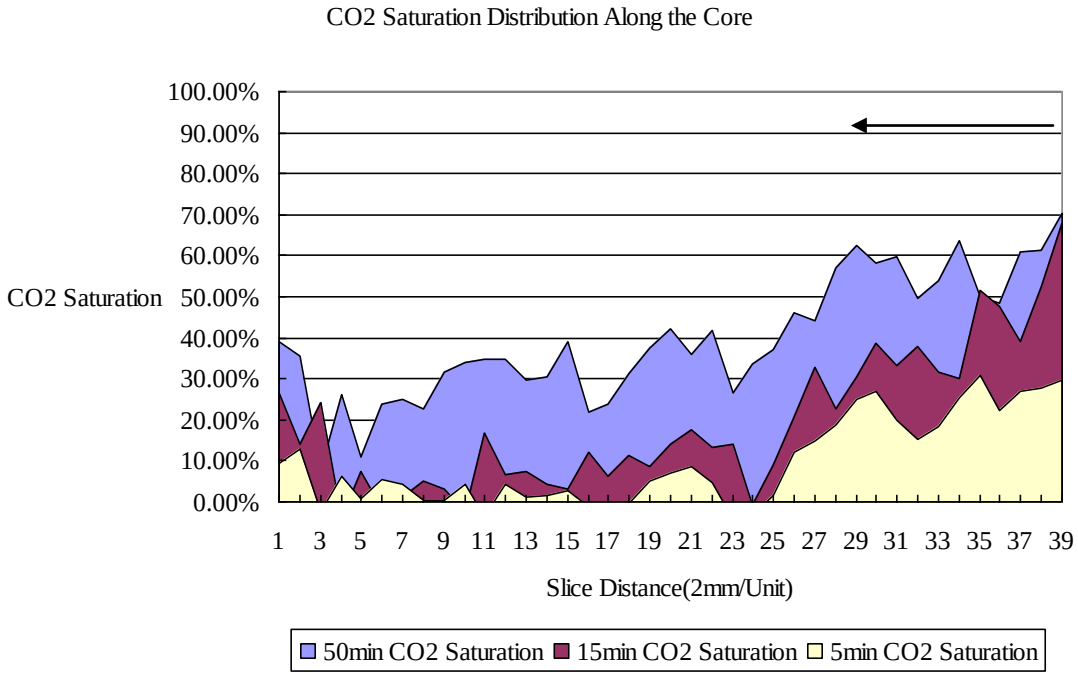

Fig. 4.13 – CO_2 Saturation Distribution in Highly Fractured Sandstone Core

The saturation profile shows that very low CO_2 saturation builds up in the sandstone core with an average saturation of approximately 30%. It can also be observed that relatively higher CO_2 saturation is obtained near the inlet of CO_2. These observations can be attributed to the fact that most of injected CO_2 is flowing through the fracture pathways instead of sweeping the sandstone matrix. To reduce CO_2 mopbility and improve sweep efficiency, we then tried on applying HPAM / $Cr(OAc)_3$ cross-linked gel in our next set of experiments.

4.4 Experiments in Fractured Sandstone Using Cross-linked Polymer Gels for Conformance Control

We reviewed various techniques to improve CO_2 flooding efficiency in sandstone reservoirs and decided to use HPAM / $Cr(OAc)_3$ cross-linked gel system to treat the fracture regions.

A highly fractured sandstone core model was then designed for CO_2 coreflood experiment and cross-linked gel was used this time to investigate the effects of conformance control on CO_2 flow in the heterogeneous media. The experimental results confirmed the positive contribution of gel application to the fractured sandstone.

The following fractured sandstone pattern was designed and applied for coreflood experiments. Fractured sandstone blocks were put together so that both horizontal and vertical fracture planes are present in the sandstone core.

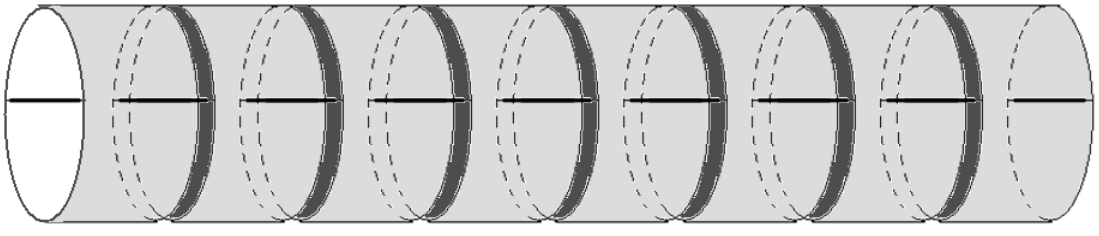

Fig. 4.14 – Designed Fractured Sandstone Pattern for Gel Conformance Control Study

In Fig. 4.14, the fractures are shown in black color; the fractured core was assembled by small blocks. The small blocks were fractured right in the center and were aligned during the assembly to produce a longer core with both horizontal and vertical fractures. High oil recovery is expected for CO_2 flooding in this constructed core pattern because of CO_2 gravity segregation in the horizontal fracture plane and CO_2 fluid redistribution

in the vertical fracture plane. If the CT images followed, the horizontal and vertical fracture intersections would appear as dark spots because the density at the intersection of fractures would be the lowest, corresponding to small CT number. The small CT numbers of these fracture intersections would fall out of the CT image color spectrum. Thus, black color will be assigned for all these small CT number regions.

4.4.1 3000 ppm Gel Application

Before coreflood experiment, the core was first oven heated and weighed. Then, the dry core was placed in the core holder with a confining pressure of 2000 psi and under temperature of 70 °F. Then CO_2 fluid was injected into the dry core to achieve 100% CO_2 saturation at 800 psi. (CO_2 is predicted to be in liquid state at 800psi and 70 °F.) Then, the core was scanned. Next, the core was flushed with 50 ml of oil. The core was left under 800 psi pressure overnight to achieve 100% oil saturation. The fractured sandstone core was scanned for a total of 5 times at different intervals during the whole CO_2 flooding process.

After CO_2 flood, pre-formed gel injection was performed to the sandstone core. Low concentration 3000 ppm gel solution (with 6% KI dopant) and $Cr(OAc)_3$ cross-linker solutions were mixed and left to cure for 24 hrs at room temperature. Then preformed cross-linked gel was transferred to the accumulator and 10 ml of gel was injected into the core. The sandstone core was scanned 2 times during the gel placement stage. (Injection pressure for the gel around 100 psi)

The core was left for 24 hours at room temperature after gel placement. Then CO_2 flood was resumed. The sandstone core was scanned 2 times during CO_2 flooding stage (Below MMP 800 psi).

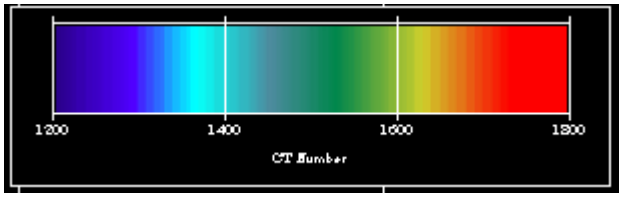

Fig. 4.15 – Color Spectrum (CT Number 1200~1800) for CT Images in Section 4.4.1

Fig. 4.15 shows the color spectrum for CT images. In the images below, the upper slab is the horizontal cross section of the core while the lower slab is the vertical cross section of the core. These images are reconstructed from 2 mm interval multiple cross scans of the core. The fluid flow direction is always from right to left. The description above applies to all the cross section images shown in the thesis.

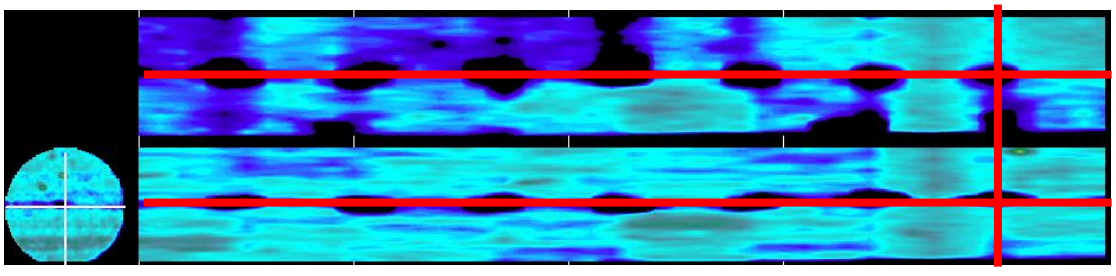

Fig. 4.16 – Scan of 100% CO_2 Saturated Fractured Sandstone Core

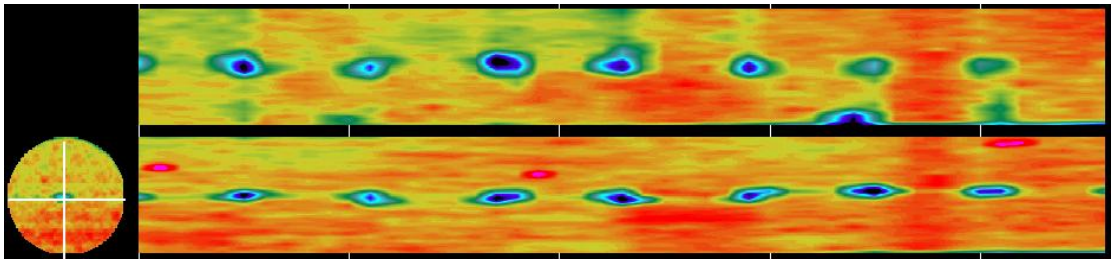

Fig. 4.17 – Scan of 100% Oil Saturated Fractured Sandstone Core

Two saturation images were shown in Fig 4.16 and Fig. 4.17. The horizontal and vertical fracture intersections are shown as dark spots in the images and there is clear difference between the horizontal slab and the vertical slab. In the 100% CO_2 saturated image, the upper slab is where the horizontal fracture is located, more CO_2 will aggregate in this fracture region and it can be seen that the color is dark blue compared to the vertical slab image, indicating a lower CT number and higher CO_2 saturation in the fracture plane. Vertical fractures can also be observed in form of vertical dotted lines composed of dark blue dots, but not as significant as horizontal fractures. Some horizontal and vertical fracture direction are marked using red lines in Fig. 4.16.

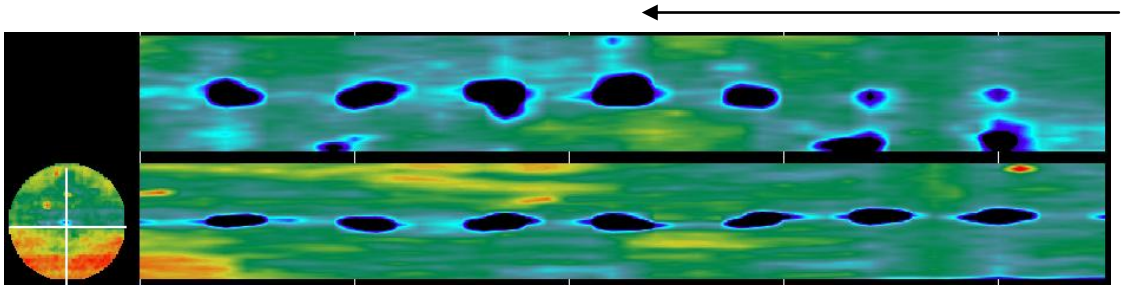

Fig. 4.18 – Scan at 2 Min of the CO_2 Flooding (Arrow shows the direction of CO_2 flow and it applies to all the coreflood images throughout the thesis.)

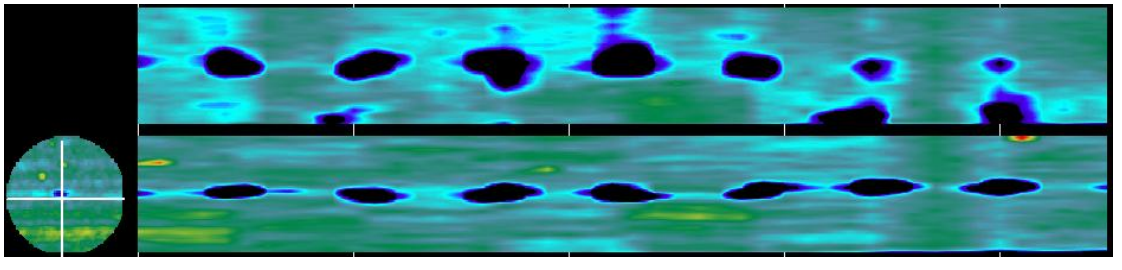

Fig. 4.19 – Scan at 6 Min of the CO_2 Flooding

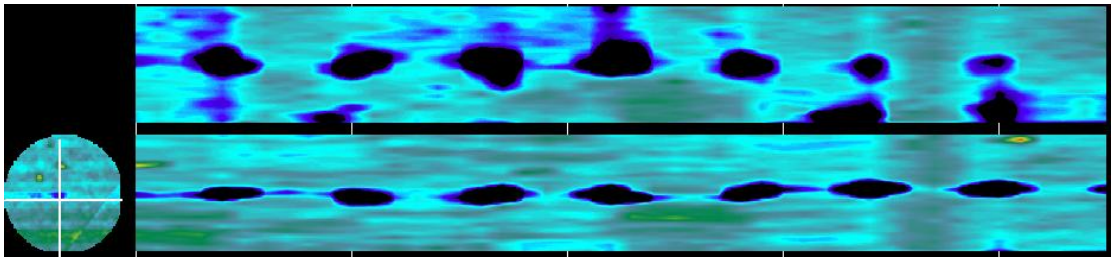

Fig. 4.20 – Scan at 12 Min of the CO_2 Flooding

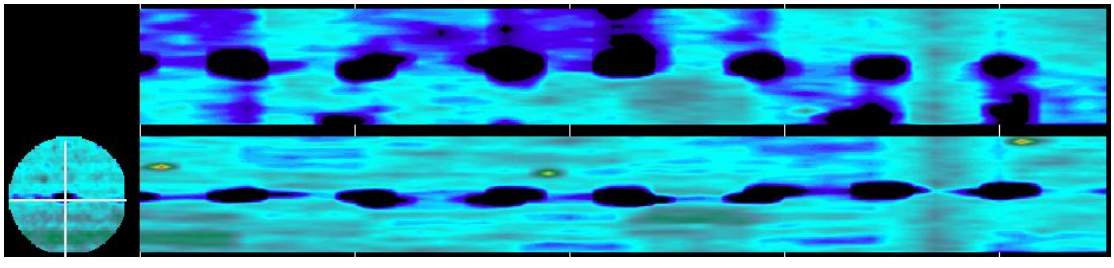

Fig. 4.21 – Scan at 25 Min of the CO_2 Flooding

CT images at different stages are shown in Fig. 4.18, Fig. 4.19, Fig. 4.20 and Fig. 4.21. In the coreflood experiment, the breakthrough of CO_2 was almost instantaneous. In the 2 min scan image (Fig. 4.18), a bright blue stripe of CO_2 fluid path can be observed in the horizontal fracture. The CO_2 flow did not sweep the other parts of the matrix. As time progressed, CO_2 gradually diffused into the matrix region of the fractured sandstone cores and CO_2 saturation increased accordingly. There always exists a color difference between the upper horizontal cross section and the lower vertical cross section because CO_2 preferably aggregates in the fracture plane which appears as dark blue regions in the image.

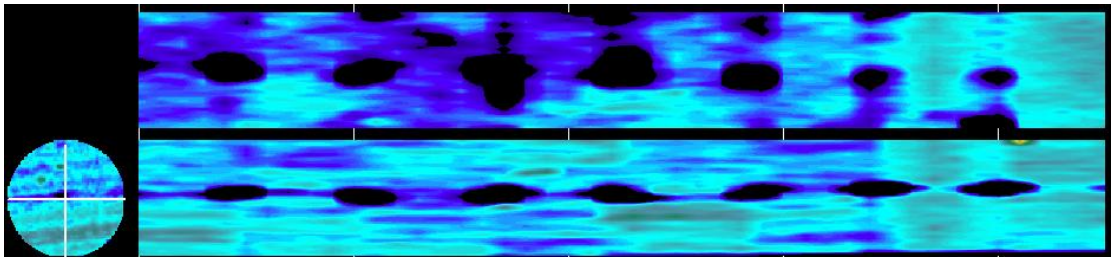

Fig. 4.22 – Scan before Gel Injection at 100 psi Gel Injection Pressure

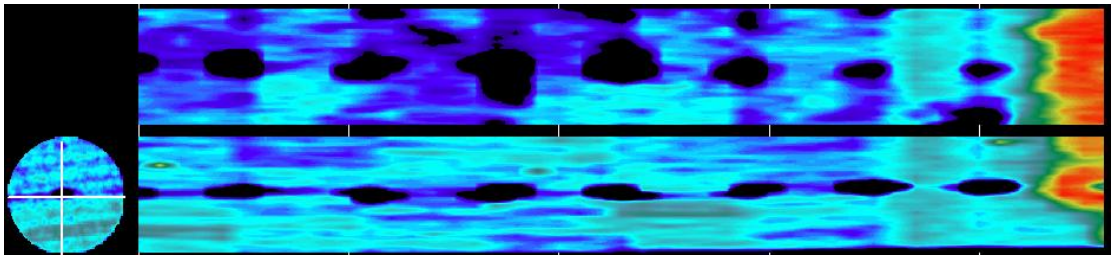

Fig. 4.23 – Scan after Gel Injection at 100 psi Gel Injection Pressure

The core was scanned before and after gel placement and CT images are shown in Fig. 4.22 and Fig. 4.23. It was expected that the preformed cross-linked gel will not enter the matrix region. However, the reconstructed images suggest otherwise. After the gel placement, it can be seen that the gel invaded the first fractured sandstone block almost completely. Ideally gel placement should only place cross-linked gel in the fractures instead of making the gel seep into the reservoir matrix. This unexpected behavior may be due to the low concentration of gel selected (3000 ppm); another reason may be a leak from the cross-linked gel entering the matrix.

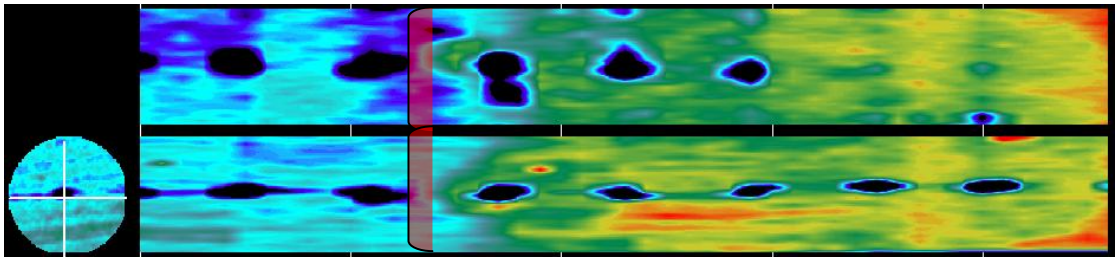

Fig. 4.24 – Scan at 2 Min of CO_2 Flooding in Core with Gel Placement

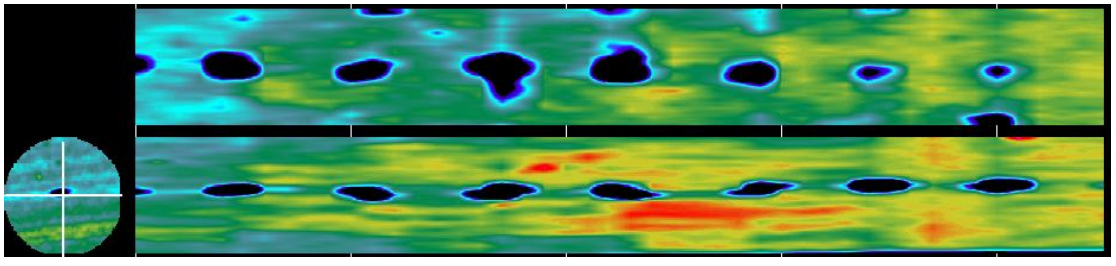

Fig. 4.25 – Scan at 30 Min of CO_2 Flooding in Core with Gel Placement

CT images of CO_2 flooding after gel placement are presented in Fig. 4.24 and Fig. 4.25. The instability of the low concentration gel was demonstrated during the CO_2 flooding process. Initially during the CO_2 flooding process, gel only occupies the first block of the fracture sandstone core. At 2 min, the red colored gel region seems to spread out to the left half of the core; the gel color changes from red to yellow due to diluted concentration of KI dopant caused by gel expansion. While at 2 min of the CO_2 flooding we can still see a gel front (shown by red highlighted area in Fig. 4.24), at the end of the 30 min CO_2 flooding, the gel front is completely destroyed and the gel fragments even reach the left end/outlet of the core. During the CO_2 flooding process after the gel treatment, incremental oil production was observed. Processed CO_2 saturation plots and recovery curves were obtained in Fig. 4.26.

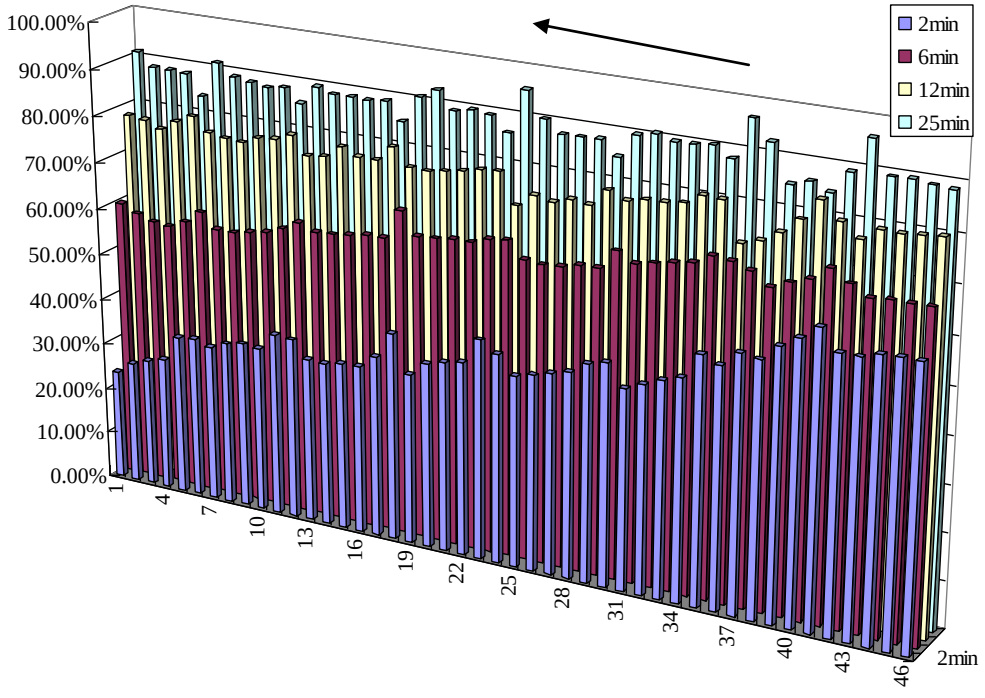

Fig. 4.26 – CO_2 Saturation Distribution in Fractured Sandstone Core

The CO_2 saturation profile along the core was computed and plotted as shown above. The vertical axis is CO_2 saturation and the horizontal axis is the slice image number which is 2 mm distance in between. The CO_2 flow direction is shown by the arrow above the plot.

The distribution of CO_2 saturation is relatively uniform throughout the core; initially the CO_2 saturation is lower at the left outlet end. As time elapses, CO_2 saturation increases almost simultaneously to 90% across the whole core. This is also a good demonstration of applicability of CO_2 flooding in highly fractured sandstone reservoir.

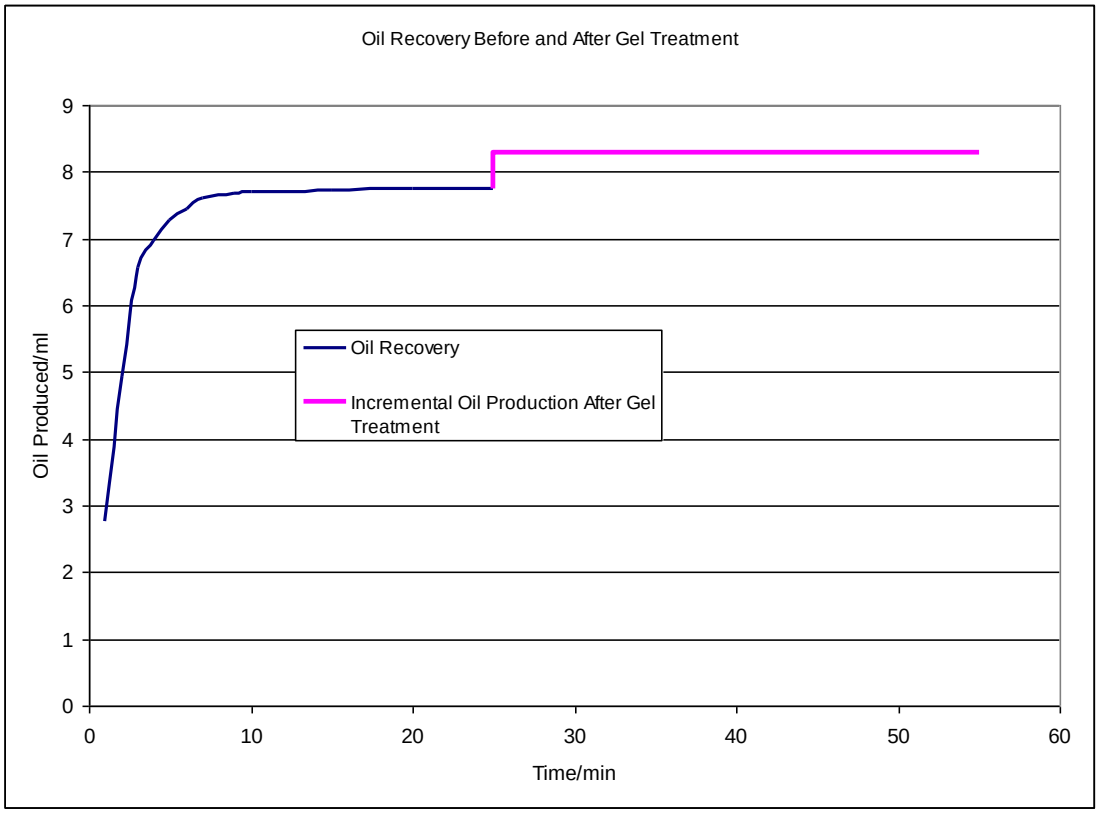

Fig. 4.27 – CO_2 Flood Recovery Curve for Fractured Sandstone

The recovery data is processed and shown in Fig. 4.27.

Average porosity of the sandstone is measured to be 19 % and the OOIP is estimated to be 8.95 ml. The initial oil recovery after CO_2 flood is 87% OOIP and incremental oil recovery after gel placement is 6% OOIP.

The pressure drop Δp from pressure transducer reading was around 8 psi before gel placement and around 54 psi after gel placement; this demonstrates the effectiveness of applying cross-linked gel to reduce CO_2 permeability in the core.

Our next step of research will be the application of higher concentration of cross-linked HPAM/$Cr(OAc)_3$ polymer gel to avoid gel breakdown and leak-off during CO_2 flooding.

The gel strength is a function of both concentration and composition. Observations made during the coreflood lead to our next step investigation of gel stability in fractured sandstone. To avoid the breakdown of gel structure and to reduce the water content leaking from the cross-linked polymer gel system to the sandstone matrix (Leak-off) will be our primary study topics. The final goal is to reduce gel leak-off, maintain gel stability and keep CO_2 permeability reduction.

4.4.2 10000 ppm Gel Application

In the previous laboratory study to control CO_2 mobility, we tested the diversion effect of relatively low concentration cross-linked gel system (3000 ppm concentration) and we observed incremental recovery due to the application of the cross-linked gel. However, the gel strength became our concern since at the end of the CO_2 flood experiment; significant gel front break down was observed. To complete the study we have tested another gel system of higher polymer concentration (10000 ppm concentration) so that we could compare the gel strength differences through direct CT image analysis.

Before coreflood experiment, the core was first oven heated and weighed; the dry core was placed in the core holder with a confining pressure of 2000 psi and under temperature of 70 °F. Then CO_2 fluid was injected into the dry core to achieve 100% CO_2 saturation at 800 psi; the core was scanned at this stage. Then the core was flushed with 50 ml of oil. The core was left under 800 psi pressure overnight to achieve 100% oil saturation (CO_2 is predicted to be in liquid state at 800 psi and 70 °F).

The fractured sandstone core was scanned for a total of 4 times at different intervals during the whole CO_2 flooding process.

After CO_2 flood, pre-formed gel-injection was performed to the sandstone core. High concentration 10000 ppm gel solution (with 6% KI dopant) and $Cr(OAc)_3$ cross-linker solution were mixed and left to cure for 24 hrs at room temperature. It was observed that this gel was much more elastic than the previous low concentration gel; the high concentration 10000 ppm cross-linked gel could not flow easily as did the low concentration 3000 ppm cross-linked gel. Preformed cross-linked gel was transferred to the accumulator and 10 ml of gel was injected into the core. The sandstone core was scanned 2 times during the gel placement stage. (Gel injection pressure around 1500 psi) The core was left for 24 hours at room temperature after gel placement. Then CO_2 flood resumed. The sandstone core was scanned 2 times during CO_2 flooding stage.

The color spectrum for this study is shown in Fig. 4.28.

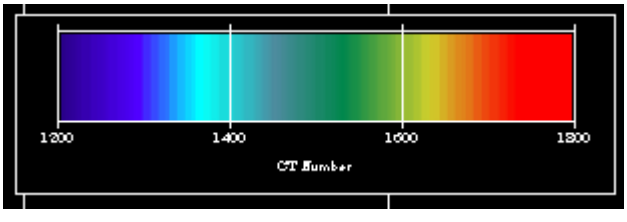

Fig. 4.28 – Color Spectrum (CT Number 1200~1800) for CT Images in Section 4.4.2

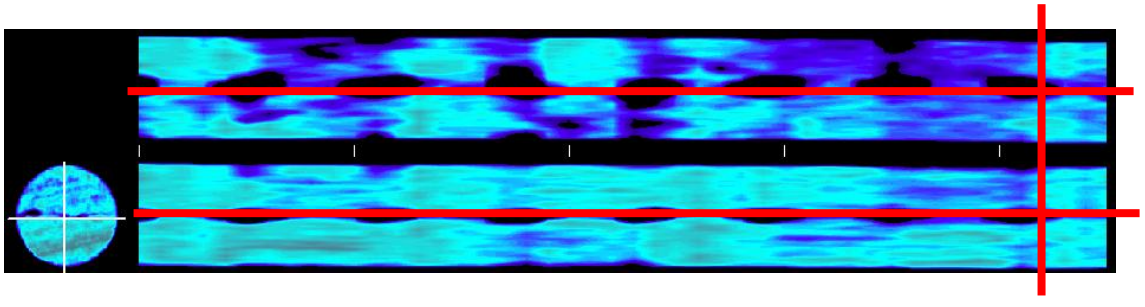

Fig. 4.29 – Scan of 100% CO_2 Saturated Fractured Sandstone Core

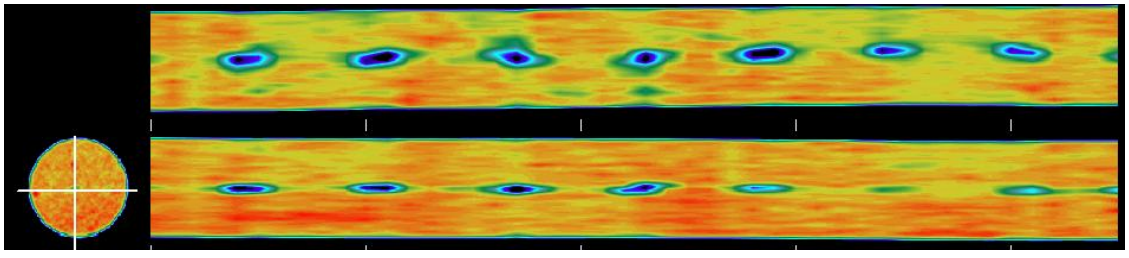

Fig. 4.30 – Scan of 100% Oil Saturated Fractured Sandstone Core

The same image features were observed as the coreflood experiment in section 4.4.1 on low concentration cross-linked polymer gel. In Fig. 4.29, higher concentration of CO_2 is observed on the horizontal fracture plane in dark blue color. There is sharp color contrast between the 100% CO_2 saturated core image (Fig. 4.29) and 100% doped oil saturated core image (Fig. 4.30).

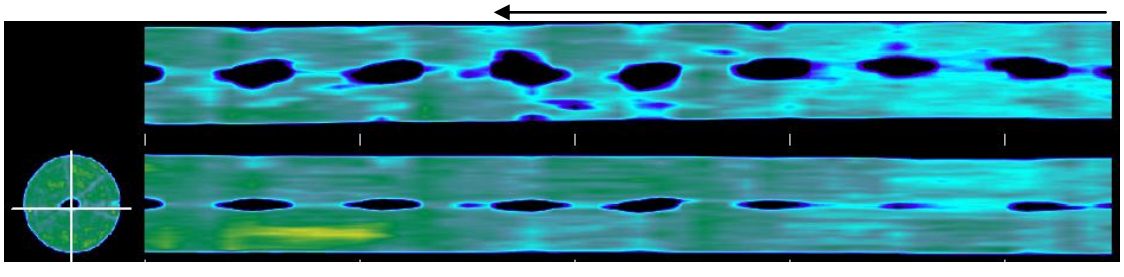

Fig. 4.31 – Scan at 4 Min of the CO_2 Flooding (Arrow shows the direction of CO_2 flow and it applies to all the coreflood images throughout the thesis.)

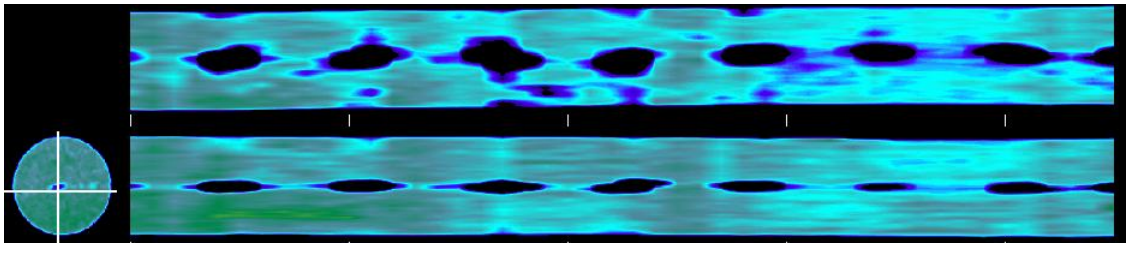

Fig. 4.32 – Scan at 9 Min of the CO_2 Flooding

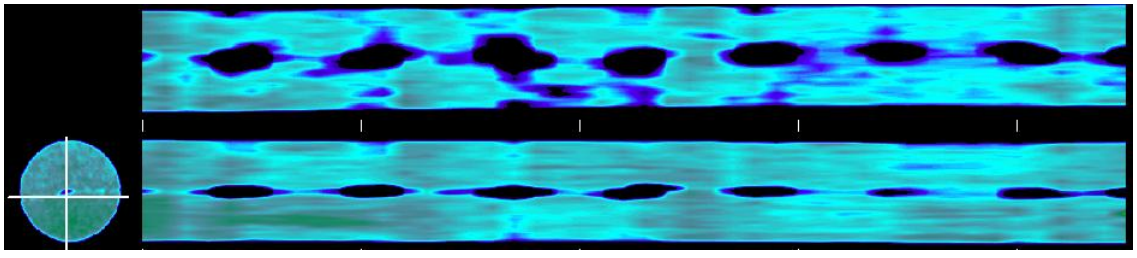

Fig. 4.33 – Scan at 25 Min of the CO_2 Flooding

CT images at different stages of CO_2 flooding were shown in Fig. 4.31, Fig. 4.32 and Fig. 4.33. Again, fast breakthrough of CO_2 was observed in the coreflood experiment. A bright blue stripe of CO_2 fluid path can be observed in the horizontal fracture in Fig. 4.31. The overall color of the whole core region shifts gradually from red to blue during the flooding process. Most of the observations correspond with our previous coreflood experiment. Again, there always exists a color difference between the upper horizontal cross section and the lower vertical cross section because CO_2 preferably aggregates in the horizontal fracture plane.

The CO_2 saturation profile was plotted after processing CT data in Fig. 4.34 and it resembles the CO_2 saturation profile we had in Fig. 4.26. CO_2 saturation is relatively uniform throughout the core and a slight decrease trend from right (inlet) to left (outlet) can be observed. At the end of the CO_2 flooding, the overall CO_2 saturation increases to almost 85%, demonstrating, again, the applicability of CO_2 flooding in highly fractured sandstone reservoir.

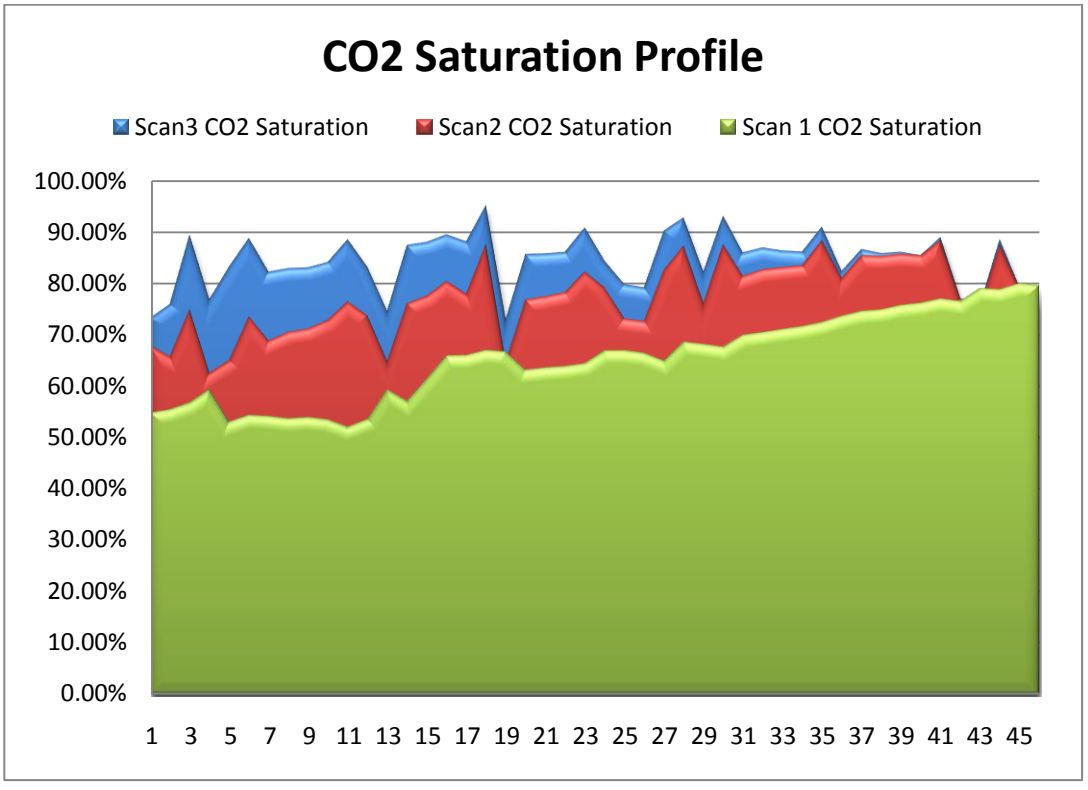

Fig. 4.34 – CO_2 Saturation Distribution in Fractured Sandstone Core

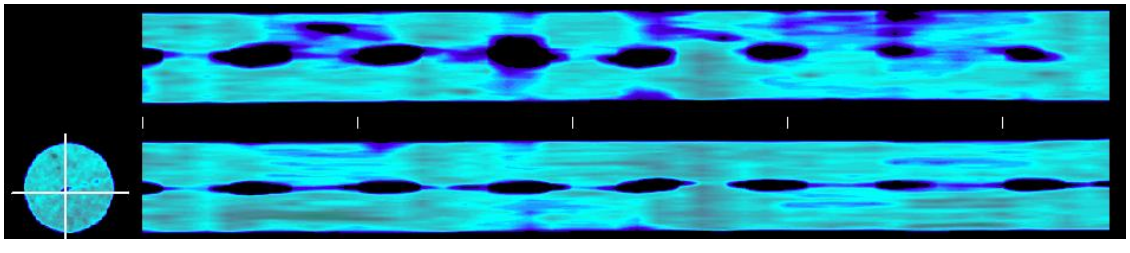

Fig. 4.35 – Scan before Gel Injection at 100 psi Gel Injection Pressure

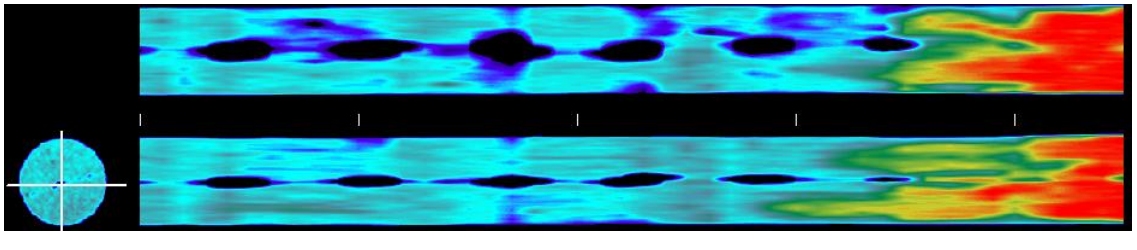

Fig. 4.36 – Scan after Gel Injection at 100 psi Gel Injection Pressure

CT images taken before and after gel placement are shown in Fig. 4.35 and Fig. 4.36. The most significant difference this time is the cross-linked gel injection pressure. Previously only 100 psi pressure was needed to inject 3000 ppm polymer gel into the core. In this experiment, before reaching 1500 psi injection pressure the pump was only compressing the gel volume. 10000 ppm gel only started to enter the core at 1500 psi. After the gel placement, it can be seen that the gel invades the first and second sandstone blocks. Again we injected 10 ml of gel same as with the 3000 ppm gel treatment. The color contrast between the gel front and the sandstone matrix is very obvious; some fingering behaviors can be observed at the gel front. The gel front in Fig. 4.36 is very difference from Fig. 4.23, possibly due to less leak-off from the 10000 ppm gel.

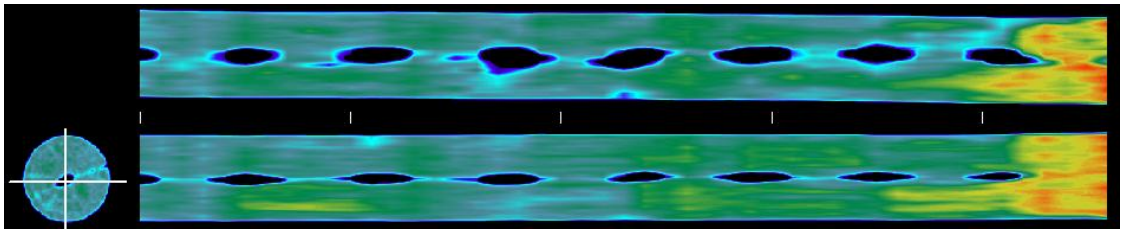

Fig. 4.37 – Scan at 2 Min of CO_2 Flooding in Core with Gel Placement

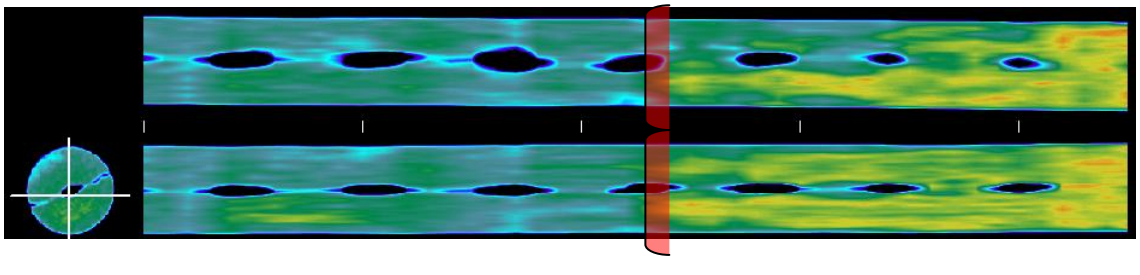

Fig. 4.38 – Scan at 30 Min of CO_2 Flooding in Core with Gel Placement

CT images taken during the CO_2 flooding after gel placement are shown in Fig. 4.37 and Fig. 4.38. The high concentration gel (10000 ppm) proved to be more stable during the CO_2 flooding process. Although after 30 min the gel invades further into the core, the invasion is confined relatively within the first half of the fractured sandstone core as shown by the red bars in Fig. 4.38. A comparison between the final gel distributions is provided in Fig. 4.39.

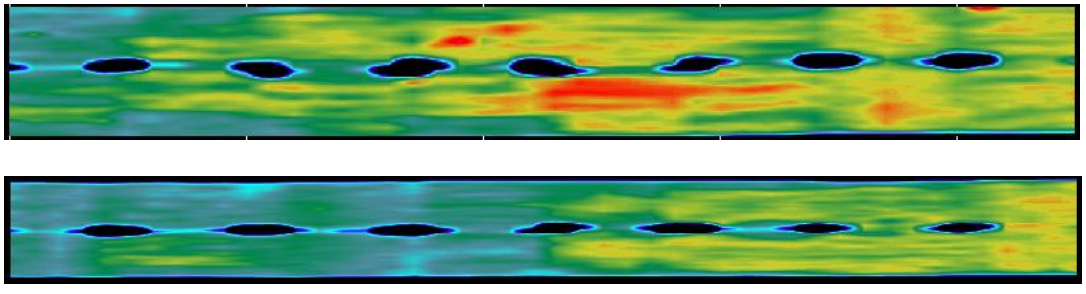

Fig. 4.39 – Comparison between the CT Images from the End of Coreflood for 3000 ppm (Above) Gel and 10000 ppm (Below) Gel

The high concentration gel stays at the injection end of the core throughout the coreflood process more than in the low concentration gel. We can conclude that there is less leak-off associated with the higher concentration gel by comparing the spreading areas of the gel. This causes less reservoir damage in the real production scenario. More importantly, this result suggests the possibility of studying gel stability using CT scan technique which visualizes the gel distribution in a very straightforward fashion.

Incremental oil production was also observed in this coreflood run with 10000 ppm gel treatment. Recovery curve obtained this time is similar to the last study.

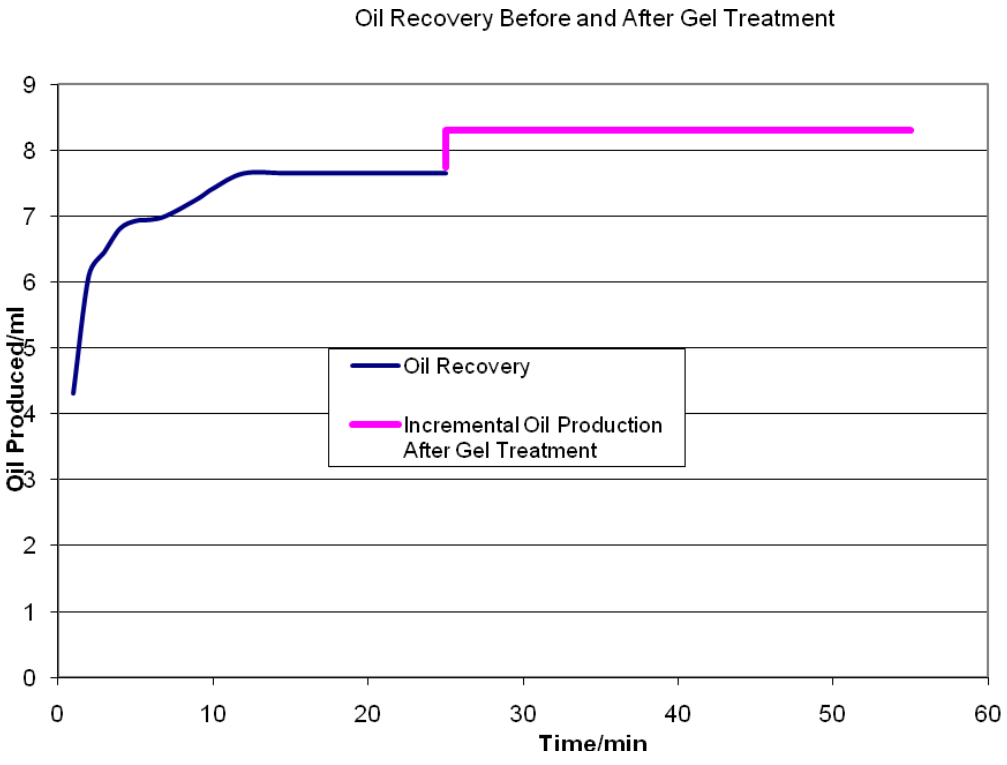

Fig. 4.40 – Oil Recovery Curve for CO_2 Flooding in Fractured Sandstone

The recovery data is processed and the recovery curve is shown in Fig. 4.40. Porosity of the sandstone is measured to be 19% and the OOIP is estimated to be 8.95ml. The original oil recovery after CO_2 flood is 85% OOIP and incremental oil recovery after gel placement is 5.6% OOIP.

The pressure drop Δp across the core from pressure transducer reading was around 8 psi before gel placement and around 850 psi after gel placement. The pressure drop of 10000 ppm gel (850 psi) is much higher than the pressure drop of 3000 ppm gel (54 psi); demonstrating the effectiveness of CO_2 permeability reduction by the higher concentration cross-linked polymer gel.

4.5 Experiment in Heterogeneous Carbonate Using Cross-linked Polymer Gels for Conformance Control

The carbonate reservoirs are typically characterized by high heterogeneity and this feature is specifically emphasized in our coreflood design. One of the challenges with carbonate coreflood is the selection of proper core sample. It is very common to encounter heterogeneities in the carbonate outcrop samples and our first run of CO_2 flood in carbonate core showed that significant heterogeneity could even lead to the blockage of CO_2 flow. We did not observe any CO_2 fluid breakthrough in some coreflood experiment when using certain impermeable yet heterogeneous carbonate cores. Fig. 4.42 is the CT image of one impermeable heterogeneous carbonate sample with a color spectrum shown in Fig. 4.41.

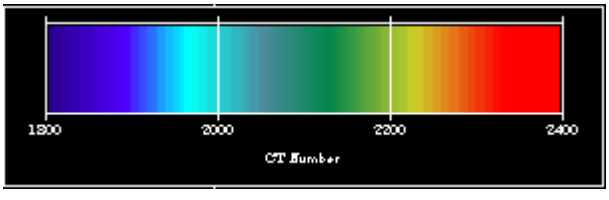

Fig. 4.41 – Color Spectrum (CT Number 1800~2400) for CT Images in Fig. 4.37

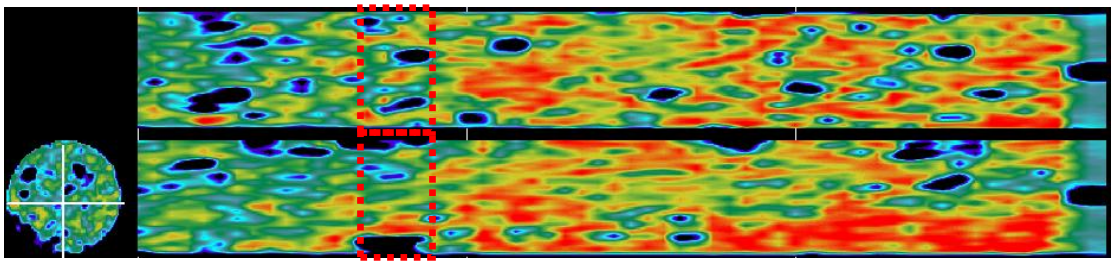

Fig. 4.42 - Scan of Impermeable Carbonate Core during Attempted CO_2 flooding

It is expected that the carbonate core sample will show some extent of permeability from the frequent presence of large pores. However during the oil injection/water drainage step, oil never broke through the whole core. During the CO_2 injection, CO_2 breakthrough did not occur either. It can be seen that a flow barrier exists at the end of the core; the region is enclosed by red dashed lines in Fig. 4.42. The left side of the barrier shows a general greenish color and the right side of the barrier shows a general reddish color. The fluid content difference between the left side (brine with low CT number) and the right side (doped oil with high CT number) causes this color contrast. Because of this barrier, oil does not seem able to get through the barrier to the left side.

Different carbonate core samples were drilled during our research. Some heterogeneous carbonate cores were obtained from carbonate cores provided by Chevron and we successfully conducted CO_2 flooding in those carbonate cores with heterogeneous permeability distribution and applied gel treatment as CO_2 mobility control method. This carbonate core has a relatively low permeability region in the injecting end and CO_2 can preferably follow the high permeability region during the CO_2 flood process. By applying the polymer gel at the entrance of the core, the permeability of the high permeability region can be adjusted so that the injecting fluid goes into the relatively low permeability regions which would have been left upswept during the initial stage of CO_2 flood.

Before coreflood experiment, the core was first oven heated and weighed. The dry core was placed in the core holder with a confining pressure of 2000 psi and under temperature of 70 °F. Then CO_2 fluid was injected into the dry core to achieve 100% CO_2 saturation at 800 psi and finally, the core was scanned. After the scan, the core was

flushed with 50 ml of oil. The core was left under 800 psi pressure overnight to achieve 100% oil saturation. (CO_2 is predicted to be in liquid state at 800 psi and 70 °F)

The carbonate core was scanned for a total of 5 times at different intervals during the whole CO_2 Flooding Process.

After CO_2 flood, in-situ gel injection was performed to the carbonate core. Low concentration 3000 ppm gel solution with $Cr(OAc)_3$ cross-linker was injected into the core immediately after mixing, injecting gel volume was 10 ml. The carbonate core was scanned twice during the gel placement stage. (Gel injection pressure around 100 psi)

The core was left for 24 hours at room temperature after gel placement. Then CO_2 flood resumed. The carbonate core was scanned twice during CO_2 flooding stage.

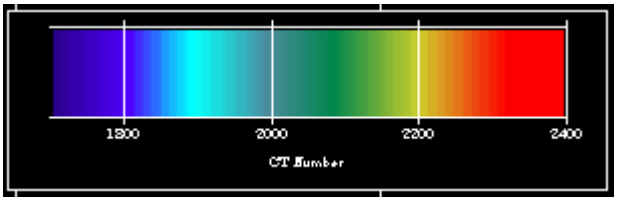

Fig. 4.43 – Color Spectrum (CT Number 1700~2400) for CT Images in Section 4.5 except Fig.4.37)

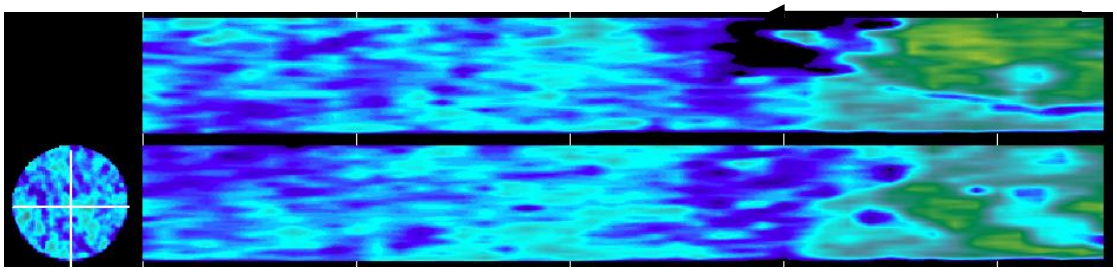

Fig. 4.44 – Scan of 100% CO_2 Saturated Heterogeneous Carbonate Core

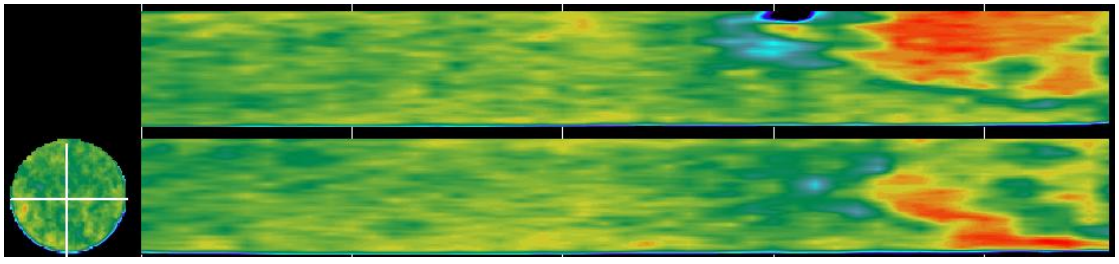

Fig. 4.45 – Scan of 100% Oil Saturated Heterogeneous Carbonate Core

The color spectrum for the study is shown in Fig. 4.43. The heterogeneity of the carbonate is very obvious from the CT images. The region on the right towards the CO_2 injection inlet has shown a different color compared to the rest of the core. In the 100% CO_2 saturated core (Fig. 4.44), low permeability region takes on the color of green. In the oil saturated core (Fig. 4.45), low permeability region takes on the color of red. This region has relatively lower permeability and higher matrix density; the high density corresponds to high CT numbers, distinguishing this region from the rest of the core. This low permeability/high density region is relatively hard to access by CO_2 during the CO_2 flooding.

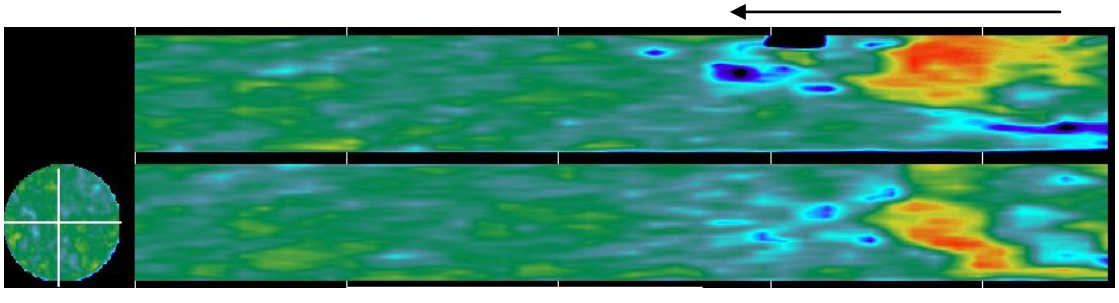

Fig. 4.46 – Scan at 5 Min of the CO_2 Flooding (Arrow shows the direction of CO_2 flow and it applies to all the coreflood images throughout the thesis.)

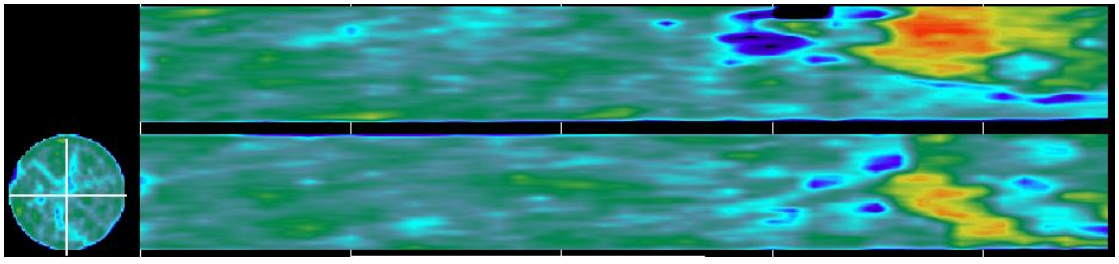

Fig. 4.47 – Scan at 8 Min of the CO_2 Flooding

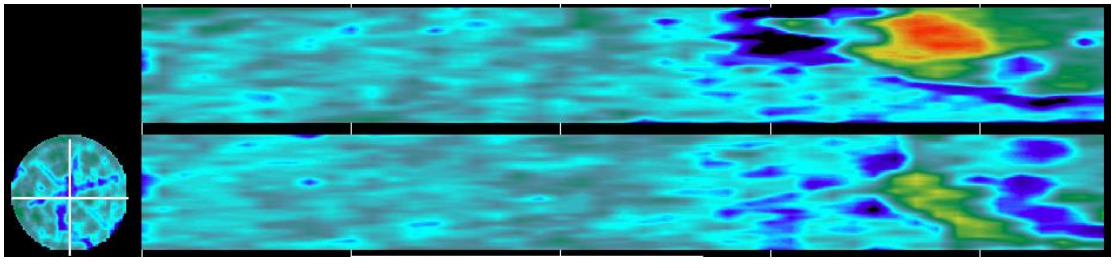

Fig. 4.48 – Scan at 15 Min of the CO_2 Flooding

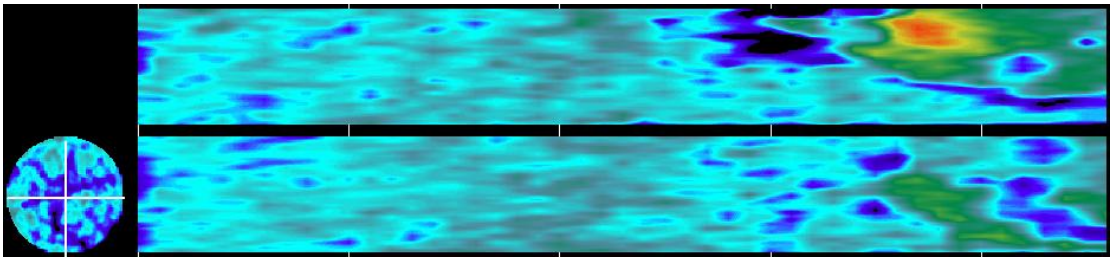

Fig. 4.49 – Scan at 40 Min of the CO_2 Flooding

CT images taken during different stages of CO_2 flooding are shown in Fig. 4.46, Fig. 4.47, Fig. 4.48 and Fig. 4.49. From the images shown above we can clearly see the color changes with time. CO_2 with low density shown in blue color is occupying the matrix gradually, and it can be observed at 5 min and 8 min that CO_2 aggregates in the matrix in the forms of blue streaks, indicating the preferable path for CO_2 flow. It is clear that

even at the end of the coreflood experiment, there is still oil trapped in the low permeability region in red color. It is reasonable to apply in-situ gel in this situation to improve the sweep efficiency. This time the gel is used in the in-situ application approach, because we are not treating fractures. For the heterogeneous yet unfractured carbonate core we inject polymer and cross-linker before gel formation so that the injected fluid enters the target matrix region and reduces the permeability of the earlier preferred CO_2 pathway; the goal is to direct the CO_2 away from the high-permeability pathway and get CO_2 into contact with oil in the low permeability region.

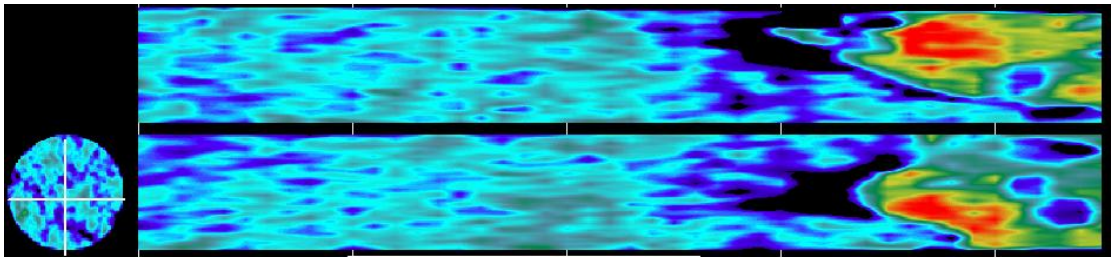

Fig. 4.50 – Scan before Gel Injection at 100 psi Gel Injection Pressure

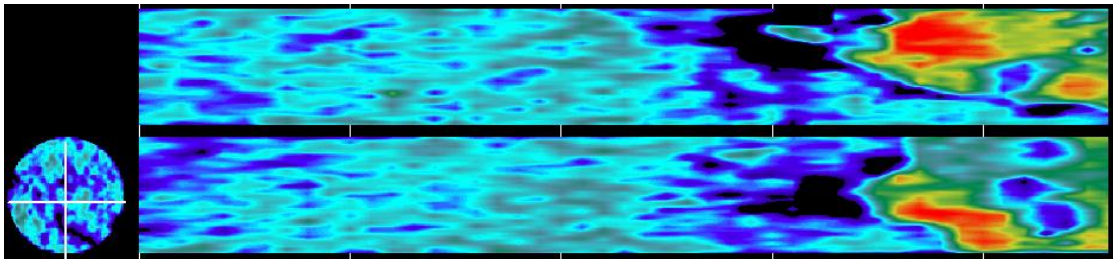

Fig. 4.51 – Scan after Gel Injection at 100 psi Gel Injection Pressure

CT images taken before and after gel placement are shown in Fig. 4.50 and Fig. 4.51. In-situ gel fluid is invading the front part of the core during this process. Considering the possible damage to the matrix, dopant KI was not added to the injected fluid. Thus no

clear distinction can be observed before and after gel injection (Fig. 4.50 and Fig. 4.51, respectively). However, by analyzing the CT number distribution across the core, the presence of gel in the matrix after the gel injection can be confirmed. The data processing result is shown below in Fig. 4.52:

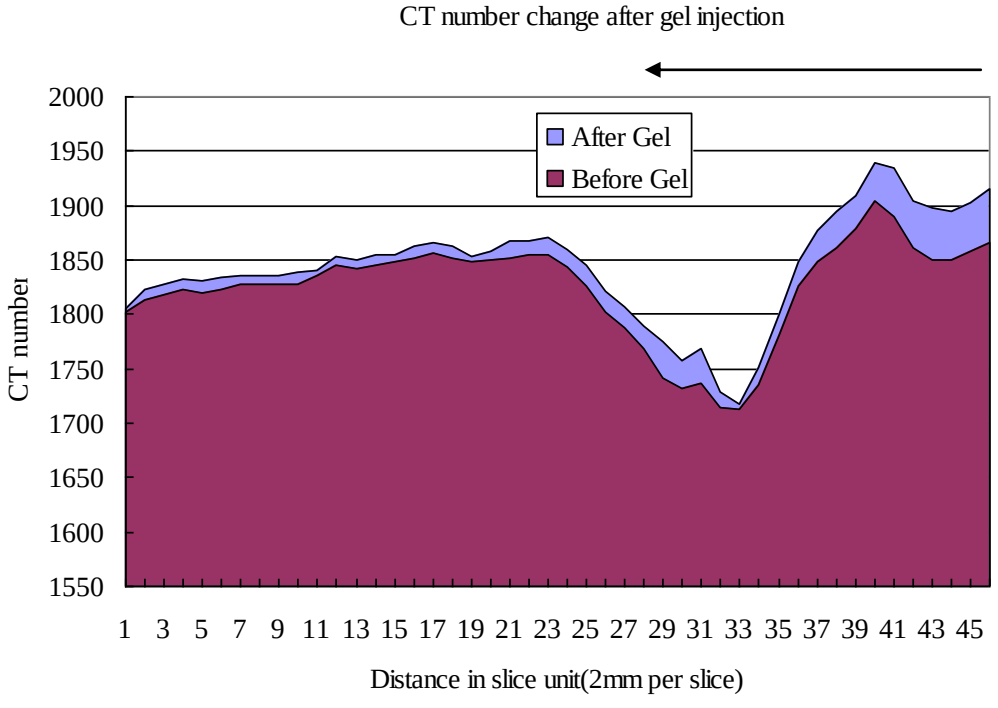

Fig. 4.52 – CT Nnumber Increase Before and After Gel Placement

It can be seen that CT number increases generally throughout the core after the gel placement. The increase is more significant towards the injection side and gradually diminishes towards the other end of the core. This confirms that the injected gel fluid is entering higher permeability regions of the core and raising the overall average CT number of the core.

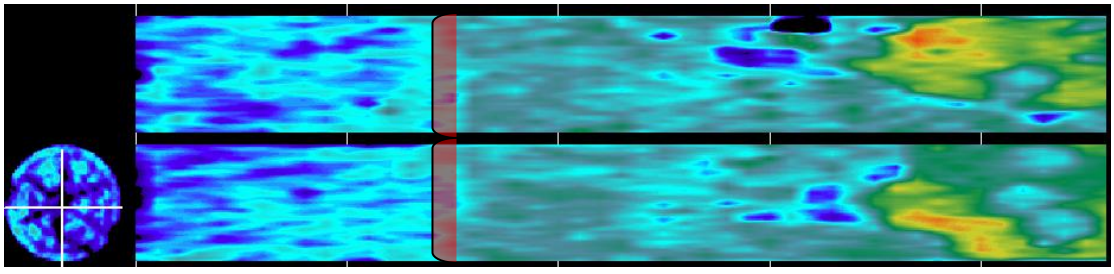

Fig. 4.53 – Scan at 2 Min of CO_2 Flooding after Gel Placement

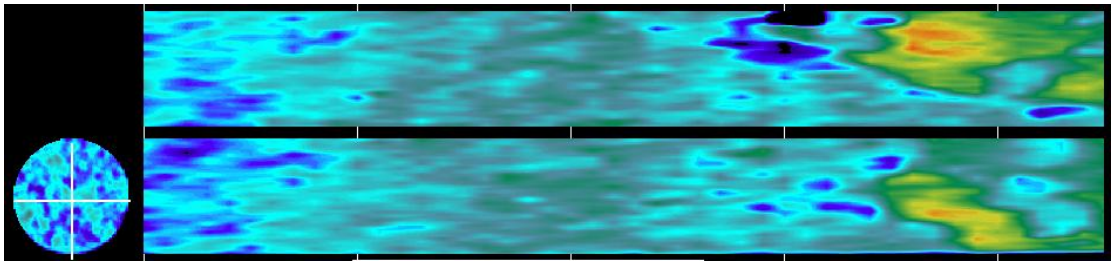

Fig. 4.54 – Scan at 30 Min of CO_2 Flooding after Gel Placement

The in-situ gel fluid had been left in the core for 24 hours after injection to complete the cross-linking reaction process. It can be observed in Fig. 4.53 that the gel formed a uniform front which is marked with red bars.

During the CO_2 flood after gel treatment, more oil is produced and collected as will be shown later in the recovery data. The incremental oil recovery is also confirmed by looking at the color change in the right region from red to almost yellow, indicating that oil has been driven out of this region.

It is important to note that after 30 min of CO_2 flooding there was no more oil production because the gel front was destroyed from Fig. 4.54. Although seems to scatter along the left half of the core due to CO_2 fluid flow, the breakdown of gel front

could not be clearly observed because KI dopant was not used to enhance the color contrast. In our sandstone coreflood experiments (Section 4.4), the gel presence was observed more clearly with KI dopant in the gel.

Fig. 4.55 – Inspection of the Actual Core Images

(Left: Injecting End/ Right: Producing End)

The core was examined after the coreflood experiment as shown in Fig. 4.55. It can be seen that a significant layer of gel was placed at the injection end which reduces the permeability of the relatively more permeable region. Although the gel front was destroyed within the core, no gel extruded out of the whole core as the producing end looks clean. However if we are to scale this operation up to the actual field production, the stability of gel can cause a big problem; it is important to ensure that the injected gel stay within high permeability regions even with CO_2 injection.

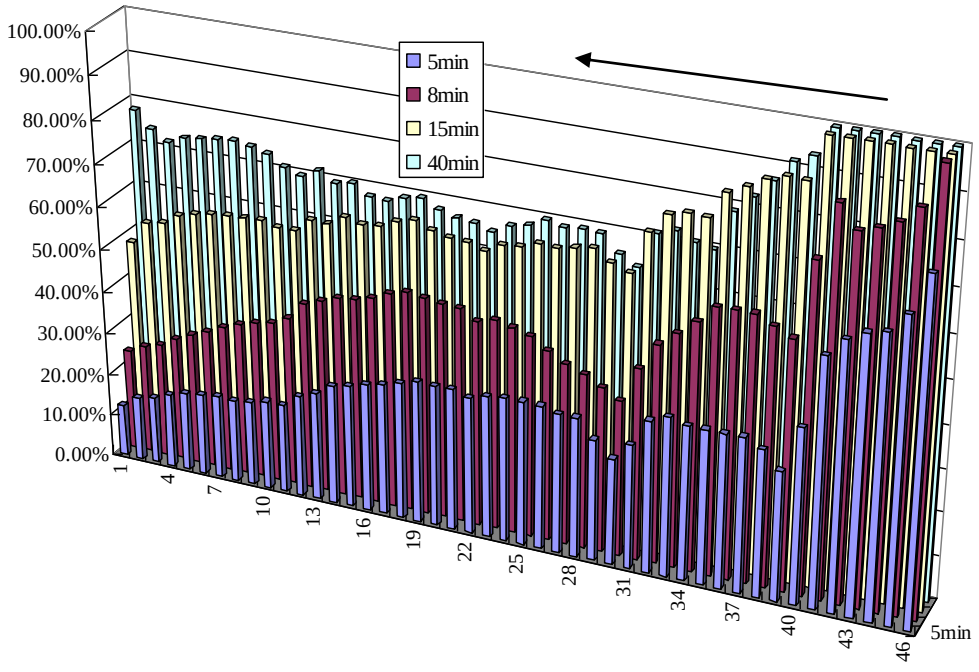

Fig. 4.56 – CO_2 Saturation Profile Distribution in Heterogeneous Carbonate Core

Fig 4.56 shows the plot of CO_2 saturation profile along the core. It can be observed that CO_2 saturation increases rapidly at the injection end while at the other end the CO_2 saturation does not go above 80% even by the end of the experiment. Significant heterogeneity pattern is shown in the CO_2 saturation profile, a common characteristic of the carbonate core.

The recovery data is processed and shown in Fig. 4.57.

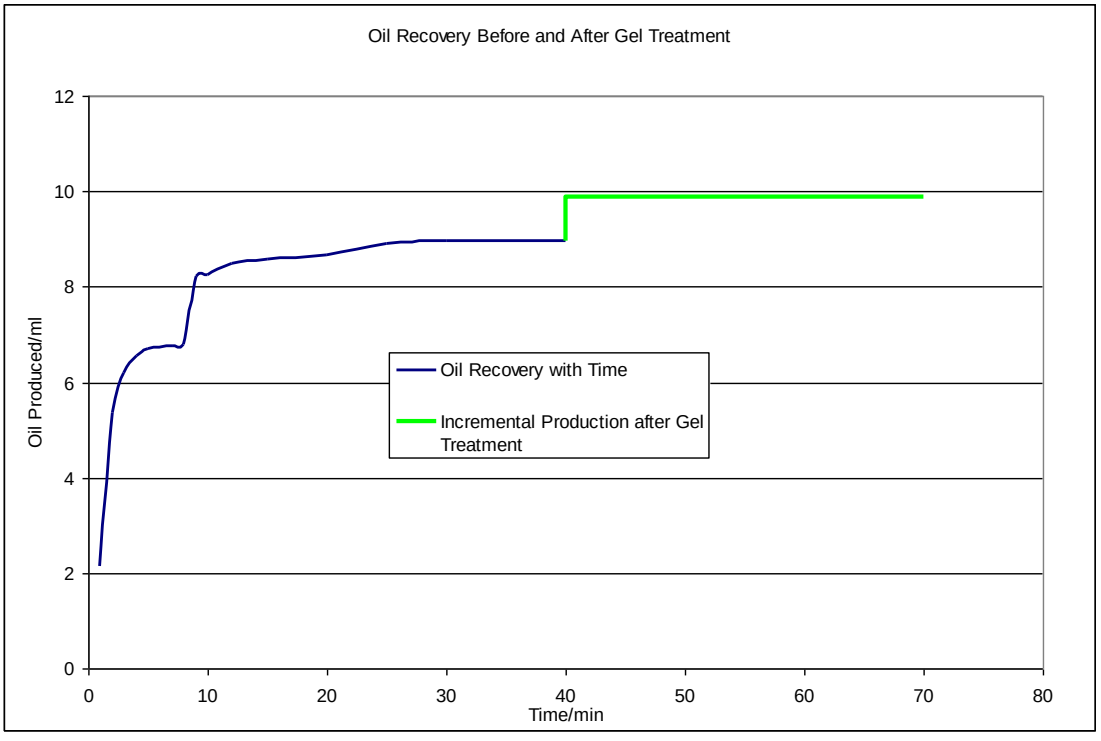

Fig. 4.57 – CO_2 Flood Recovery Curve for Heterogeneous Carbonate Core

Porosity of the carbonate is measured to be 22% and the OOIP is estimated to be 10.48 ml. The original oil recovery after CO_2 flood is 86% OOIP and incremental oil recovery after gel placement is 9% OOIP.

The pressure drop Δp from pressure transducer reading across the core region was around 50 psi before gel placement and around 660 psi after gel placement; this demonstrates the effectiveness of reducing CO_2 mobility in the core.

In the previous CO_2 mobility control laboratory studies (Section 4.4 and Section 4.5), conformance control HPAM/$Cr(OAc)_3$ polymer gel was used in both fractured sandstone and heterogeneous carbonate. Our experimental data show that the application of gel after initial CO_2 flooding yields incremental oil recovery. It is reasonable to conclude

that using HPAM/$Cr(OAc)_3$ polymer gel in CO_2 flooding operations yields additional oil recovery compared to the case where no gel treatment is applied.

4.6 Experiments in Fractured Sandstone Using Viscosified CO_2

We plan to test the efficiencies of several chemicals with promising viscosifier structural features. Using the technology of CT-imaging, we are able to monitor CO_2 fluid distribution and obtain direct measurement of residual oil saturation at different stages of the CO_2 flooding.

We designed a series of coreflood experiments to analyze the effectiveness of viscosified CO_2. Berea sandstone cores were used for the experiments. The fractured sandstone core was prepared from Berea sandstone cores with high permeability. We produced the fracture from the drilling lab and a total of 5 samples were prepared for the CO_2 flooding experiments. Each sandstone core all had a saw-cut fracture in the center throughout the core as shown in Fig. 4.58.

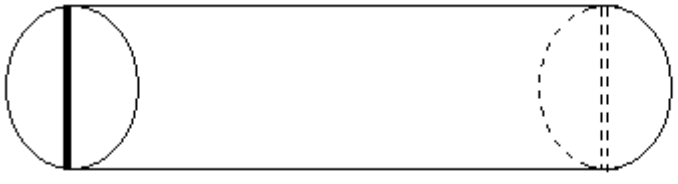

Fig. 4.58 – Sandstone Core with a Single Fracture in the Center

During the coreflood process, neat CO_2 were injected into oil saturated fractured sandstone core first as will be detailed in section 4.6.1. After the control study is established, viscosified supercritical CO_2 prepared by mixing viscosifier chemical with

CO_2 was used for CO_2 flooding and the overall efficiency was compared between each of the different viscosifiers and the neat CO_2 control experiment.

4.6.1 Neat CO_2 Flooding in Single Fracture Sandstone

Before coreflood experiment, the core was first oven heated and weighed. The dry core was placed in the core holder with a confining pressure of 3000 psi and under temperature of 130 °F. Then, CO_2 fluid was injected into the dry core to achieve 100% CO_2 saturation at 1800 psi and the core was scanned at this stage. Then, the core was flushed with 50 ml of oil. The core was left under 1800 psi pressure overnight to achieve 100% oil saturation (CO_2 is predicted to be in supercritical state at 1800 psi and 130 °F).

For neat CO_2 control experiment, CO_2 was injected directly for CO_2 flooding after the CO_2 fluid was compressed to 2000 psi in the accumulator (The CO_2 pressure in the accumulator is built up to 2000 psi to guarantee that when the CO_2 fluid reaches the inlet of the coreflood cell the CO_2 fluid pressure can still maintain around 1800 psi).

The fractured sandstone core was scanned for a total of 3 times at different intervals during the whole CO_2 Flooding Process (1800 psi injection pressure). The core was scanned after different pore volumes (PV) of CO_2 or CO_2/viscosifier mixture was injected, oil recovery was recorded also for different pore volumes of CO_2 or CO_2/viscosifier mixture injected. The color spectrum for this study is shown in Fig. 4.59.

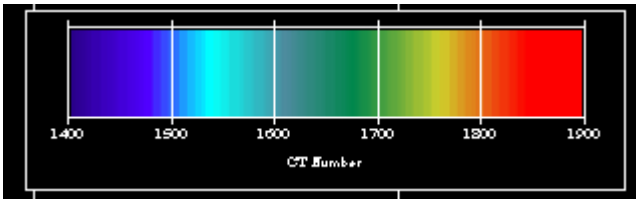

Fig. 4.59 – Color Spectrum (CT Number 1400~1800) for CT Images in Section 4.6.1

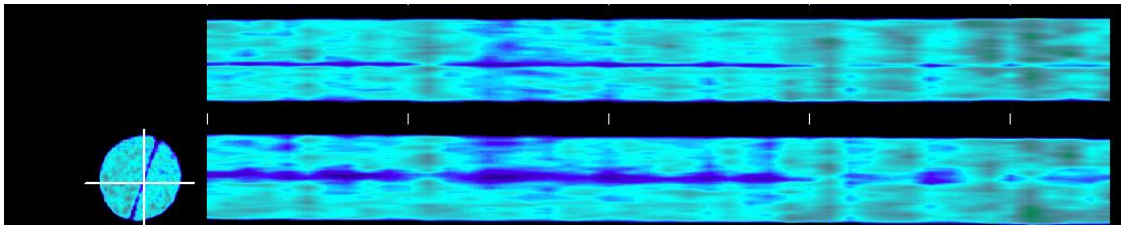

Fig. 4.60 – Scan of 100% CO_2 Saturated Single Fractured Sandstone Core

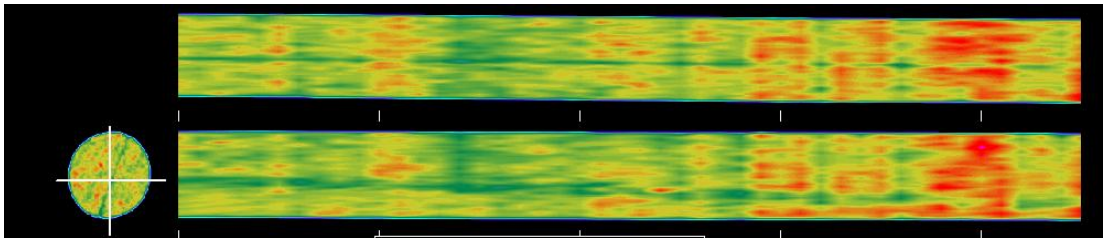

Fig. 4.61 – Scan of 100% Oil Saturated Single Fractured Sandstone Core

The CO_2 saturated core image (Fig. 4.60) and oil saturated core image (Fig. 4.61) are consistant with previous observations. It can seen clearly that the single fracture as a blue streak in the center of each core slab image. Differences between the upper slab image and the lower slab image in each figure are present as expected; the upper slab represents horizontal crosssection and the lower slab represents vertical crosssection. For the CO_2 saturated core image, we can see that the lower slab image shows more dark bule regions compared to the upper slab image. This is because the lower slab image is the vertical crosssection and it is in close proximity to the fracture plane.

In this coreflood experiment, the lower slab image shows more concentrated fluid presence; the fluid is either dark blue for CO_2 aggregation or dark red for oil aggregation.

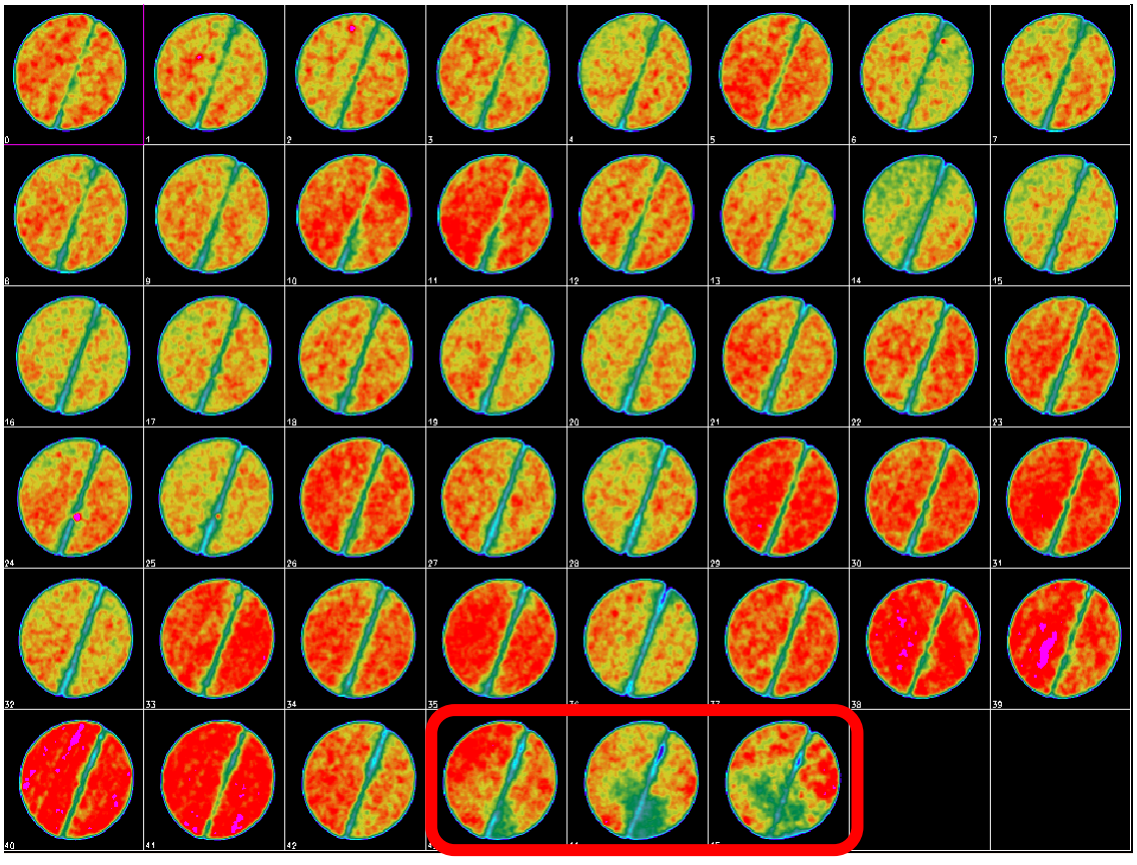

Fig. 4.62 – Vertical Slice Images of the Single Fractured Sandstone Core From Scan 1 (Images are tiled horizontally with the first image being the outlet and last image being the inlet.)

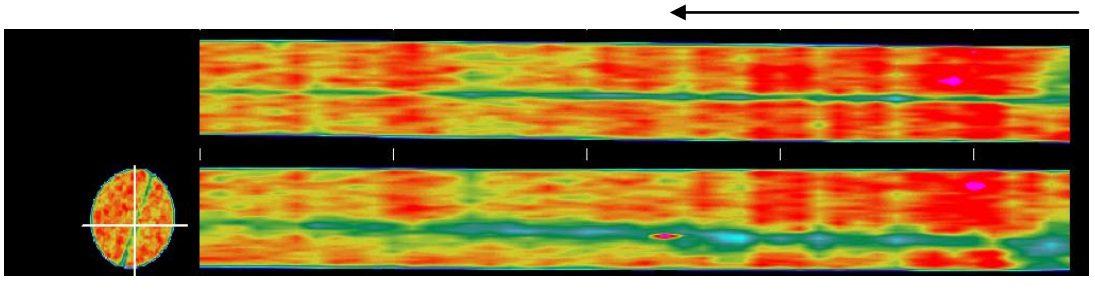

Fig. 4.63 – Scan 1 during the CO_2 Flooding in Single Fractured Sandstone (Arrow shows the direction of CO_2 flow and it applies to all the coreflood images throughout the thesis.)

Scan 1 was taken after 0.59 PV of CO_2 had been injected into the core. In comparison with the intial oil saturation image Fig. 4.61, it is very clear that CO_2 found its path along the fracture. In Fig. 4.62, we see the emerging green color spots in the first three slices at the entrance (circled out by the red rectangle), representing the accumulation of CO_2 saturation. In the reconstruction core image from Fig. 4.63, CO_2 flow preference could also be observed; in the lower slab image, the green color stays mostly at the bottom which might be caused by the higher density of viscosifier chemicals.

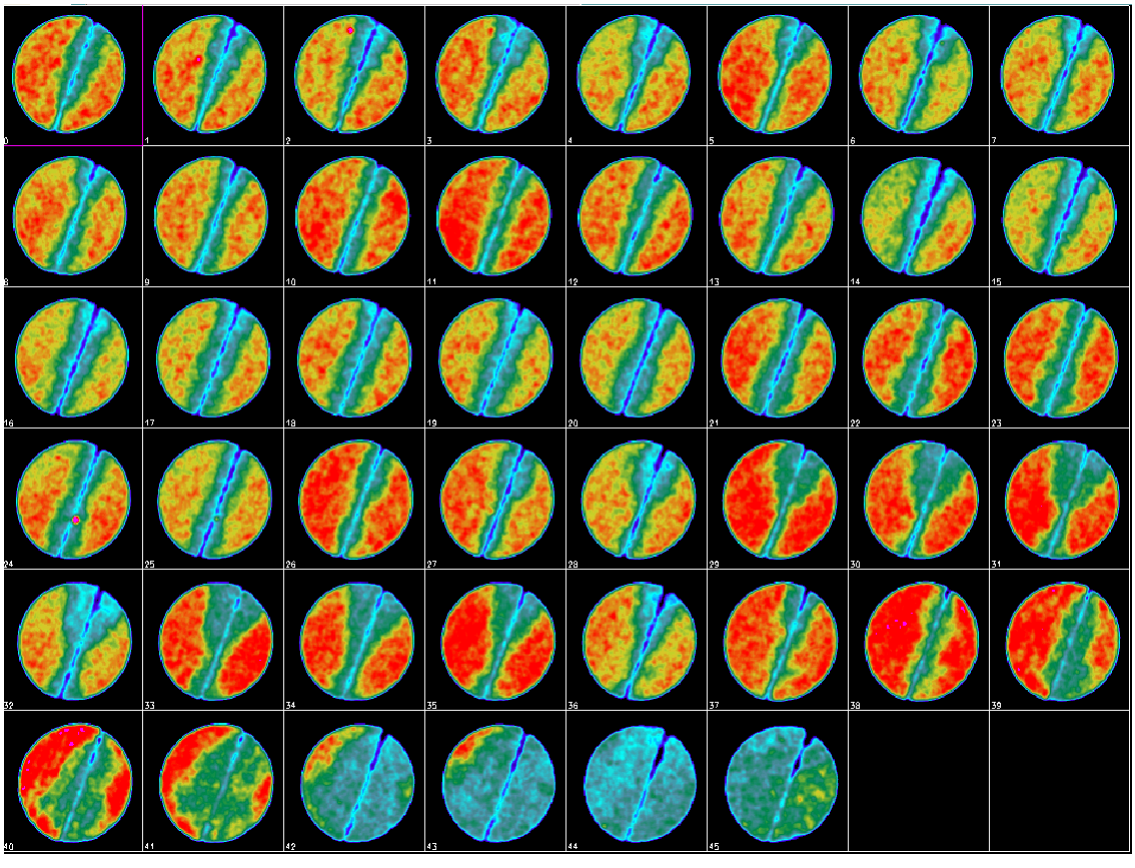

Fig. 4.64 – Vertical Slice Images of the Single Fractured Sandstone Core From Scan 2 (Images are tiled horizontally with the first image being the outlet and last image being the inlet.)

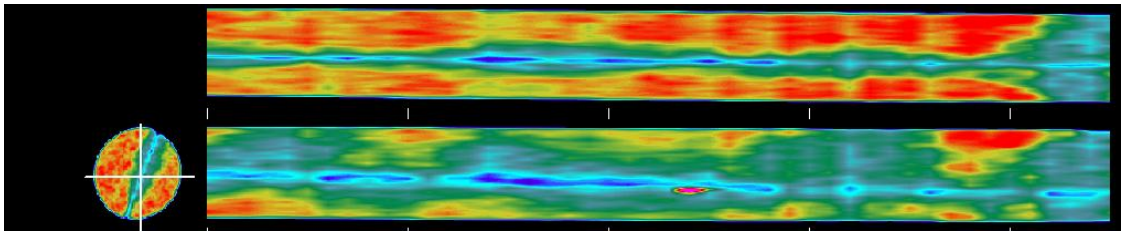

Fig. 4.65 – Scan 2 during the CO_2 Flooding in Single Fractured Sandstone

Scan 2 was taken after 1.54 PV of CO_2 had been injected. We can see clearly from the slice images that most of the fracture region has CO_2 saturation in the form of blue color compared with the surrounding yellow/red color. In Fig. 4.64, the first few slices close to the CO_2 entrance now have been almost completely saturated by CO_2. This improved swept efficiency near the injection end is expected in actually production. From Fig. 4.65, it is obvious that the CO_2 broke through the whole core (from the recovery end we observed CO_2 breakthrough around 0.8 PV.). The lower slab image in Fig. 4.65 is closer/parallel to the fracture plane. Thus, it is reasonable to see more CO_2 presence in the lower slab image. From the upper slab image in Fig. 4.65, we can conclude that the CO_2 is not forming a steady and uniform front. Instead, a sharp transition to the highly conductive fracture can be seen. This observation will likely contribute to very low CO_2 utilization in the actual production scenario.

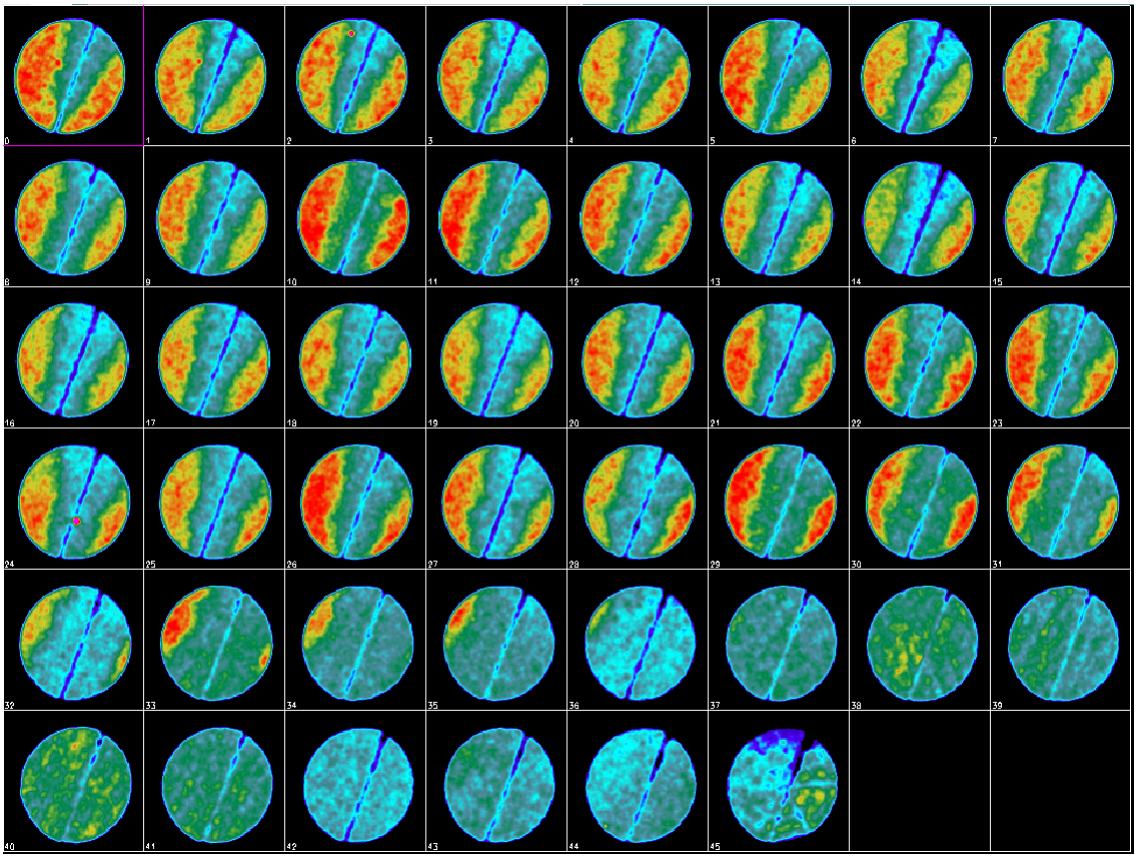

Fig. 4.66 – Vertical Slice Images of the Single Fractured Sandstone Core From Scan 3 (Images are tiled horizontally with the first image being the outlet and last image being the inlet.)

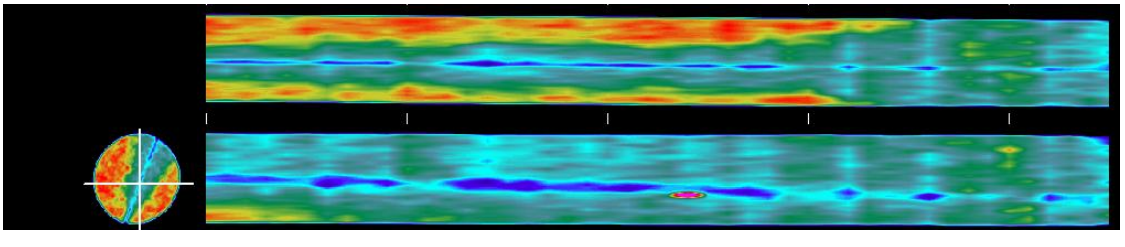

Fig. 4.67 – Scan 3 during the CO_2 Flooding in Single Fractured Sandstone

Scan 3 was take after 3.23 PV of CO_2 had been injected. The amount of CO_2 injected is already three times more than the pore volume. However, we can still observe large

streaks of red/yellow color which correspond to unrecovered oil. This color is especially obvious in the upper slab image in Fig. 4.67. CO_2 was just following the fracture's direction in the center. The sharp contrast between CO_2 and oil can also be seen in the slice images towards the outlet in Fig. 4.66.

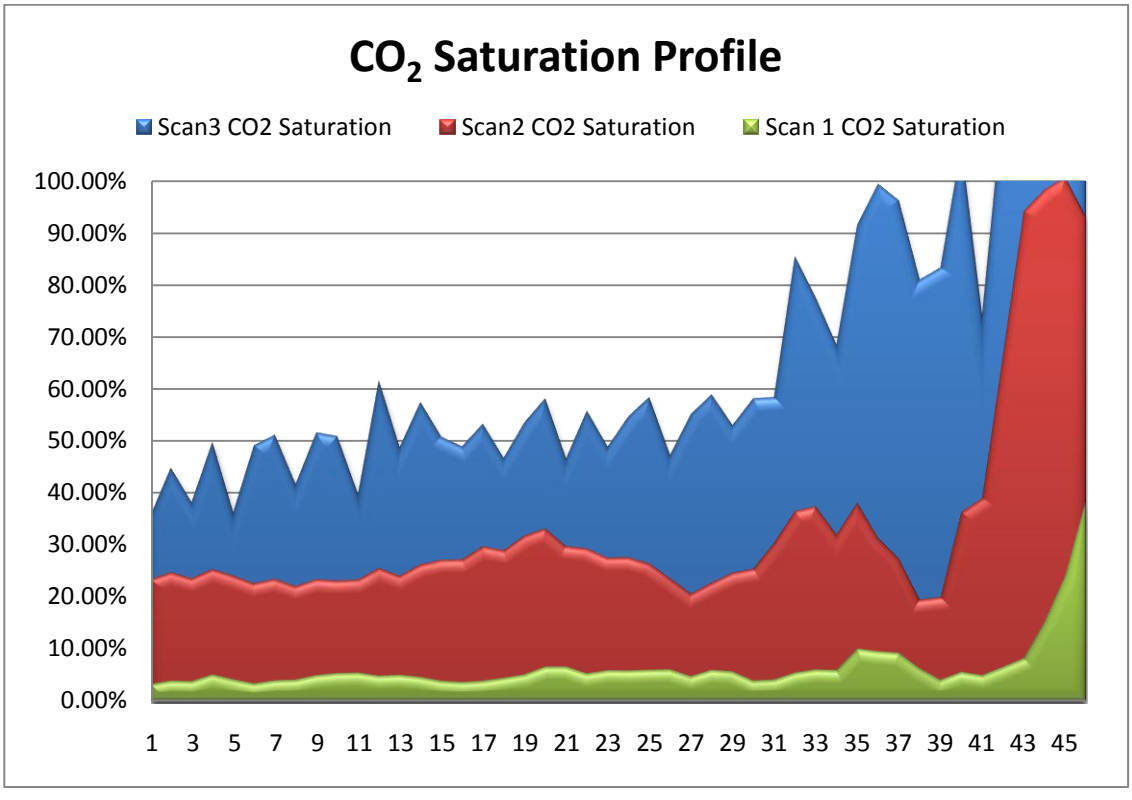

Fig. 4.68 – CO_2 Saturation Profile for Neat CO_2 Flood (CO_2 injected from right to left)

CT data was processed and CO_2 saturations at different intervals of the CO_2 flooding is plotted in Fig. 4.68. CO_2 saturation is around 20% in the injection end for scan 1 and stays uniformly low throughout the rest of the core. The CO_2 saturation close to the injection end can be increased up to 90% in scan 3. But as CO_2 progresses towards the outlet, CO_2 fluid seems to be just flowing through the fracture. Even after 3 PV of CO_2

has been injected in scan 3, most of the CO_2 saturation towards the outlet remains around 50%.

The oil recovery in terms of pore volumes is recorded in Table 4.2. The recovery data from volume measurement shows that the final oil recovery is around 67% OOIP, which is relatively low considering the high permeability of the sandstone core and large volume of CO_2 injected.

Table 4.2 – Oil Recovery Table for Neat CO_2 Flooding (CO_2 Breakthrough around 0.8 PV CO_2 injected.)

PV CO_2 Injected	0.59	1.54	3.23
OOIP% oil produced	21%	56%	67%

The recovery data in Table 4.2 agrees with the CO_2 saturation data in Fig. 4.68; both suggest a low overall recovery of the neat CO_2 flooding. CO_2 saturation was not built up effectively across the core and the overall sweep efficiency was low, thus resulting in low overall oil recovery. This will serve as a control study for our following viscosified CO_2 flooding experiments. The pressure drop for the neat CO_2 flooding process is around 8 psi, which is almost negligible. This low pressure drop is caused by the high conductivity of the fracture feature in the sandstone core.

4.6.2 Viscosified CO_2 Flooding in Single Fracture Sandstone (Dodecamethylpentasiloxane)

Dodecamethylpentasiloxane was tested as the first chemical for CO_2 viscosifier study. The structure of this chemical is shown in Fig. 3.2. The structure of this chemical contains repetitions of dimethylsiloxane unit which has been shown to be effective in viscosifying CO_2 fluid in earlier research[23]. Although the structure only contains a limited number of dimethylsiloxane units; coreflood experiments with this basic structure will yield information on the effectiveness of adding CO_2 viscosifying functionalities to the backbone of other viscosifier chemical. Dodecamethylpentasiloxane stays in liquid form at room temperature and pressure. It was used directly from reagent bottle to mix with CO_2 fluid.

Experimental conditions were same as described in section 4.6.1.

For the preparation of viscosified CO_2, the viscosifier chemical and cosolvent were placed into the accumulator first. 580 psi CO_2 was injected into the accumulator from a CO_2 gas cylinder to fill up the accumulator. The CO_2 and chemical mixture was then compressed to 2000 psi, during which time heat was generated from the mixing process. The mixture was left to reach equilibrium for 1 hour and then the mixture was used for CO_2 flooding.

5% wt of dodecamethylpentasiloxane chemical is used for the viscosified CO_2 fluid. CO_2 Weight was determined from the following method.

CO_2 gas from the gas cylinder has the properties as:

Accumulator pressure: 600 psi = 41.4 bar = 40.8 atm

Accumulator temperature: 70 °F = 294.1 K

Van Der Waals Equation was used for calculating the weight of the CO_2 used;

$$\left(p + \left({}^{n^2 a}/_{V^2}\right)\right)(V - nb) = nRT \quad \text{.....(4.1)}$$

p = the pressure of the fluid

V = the total volume of the container containing the fluid

a = a measure of the attraction between the particles (from Table 4.3)

b = the volume excluded by a mole of particles (from Table 4.3)

n = the number of moles

R = the universal gas constant

T = the absolute temperature

Table 4.3 – Van Der Waals Coefficients of Selected Gases

Gas	***a***	***b***
Unit	atm dm^6 / mol	dm^3 / mol
ideal	0.0	0.0
He	0.034	0.0237
Ar	1.345	0.0322
O_2	1.360	0.0318
N_2	1.390	0.0391
CO_2	3.592	0.0427
CH_4	2.253	0.0428
H_2	0.244	0.0266

Table 4.3 is used for constants. Solving the above equation we can get the CO_2 amount inside the accumulator (1000 ml) at 580 psi which is 2.1699 mol. The corresponding CO_2 weight is 95.48 grams.

We can then get the viscosifier weight as 4.77 gram for 5 wt% viscosifier/CO_2 mixture.

The color spectrum for this study is shown in Fig. 4.69.

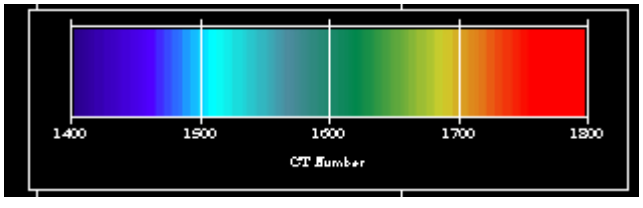

Fig. 4.69 – Color Spectrum (CT Number 1400~1800) for CT Images in Section 4.6.2

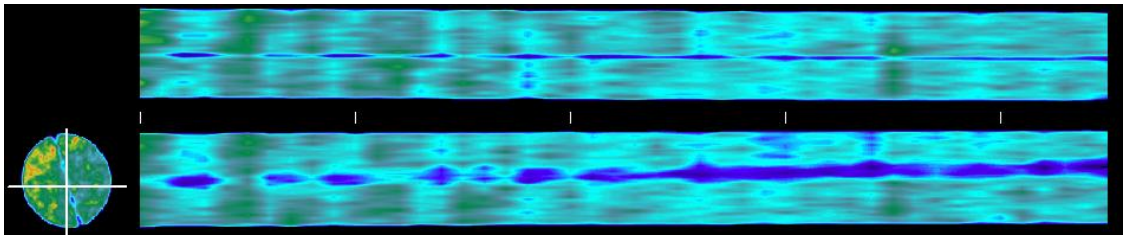

Fig. 4.70 – Scan of 100% CO_2 Saturated Single Fractured Sandstone Core

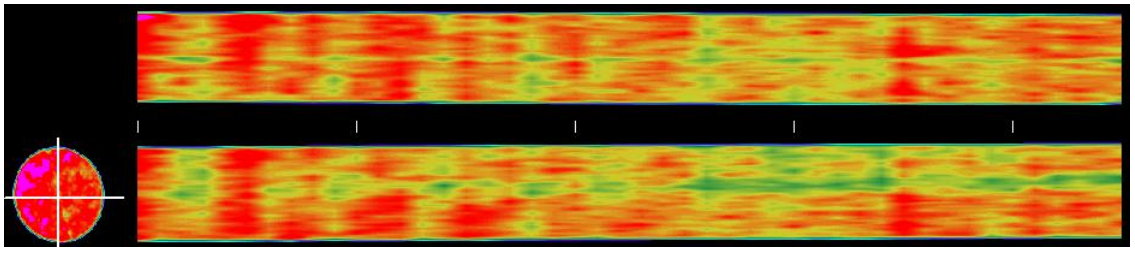

Fig. 4.71 – Scan of 100% Oil Saturated Single Fractured Sandstone Core

The above two scans are similar with the control study in section 4.6.1. Fig. 4.70 is the CO_2 saturated image and Fig. 4.71 is the oil saturated image. The vertical cross section (lower image) is closer to the fracture plane; in Fig. 4.70 more CO_2 concentration can be observed in the vertical cross section (lower image) as blue stripes compared with the horizontal cross section (upper image).

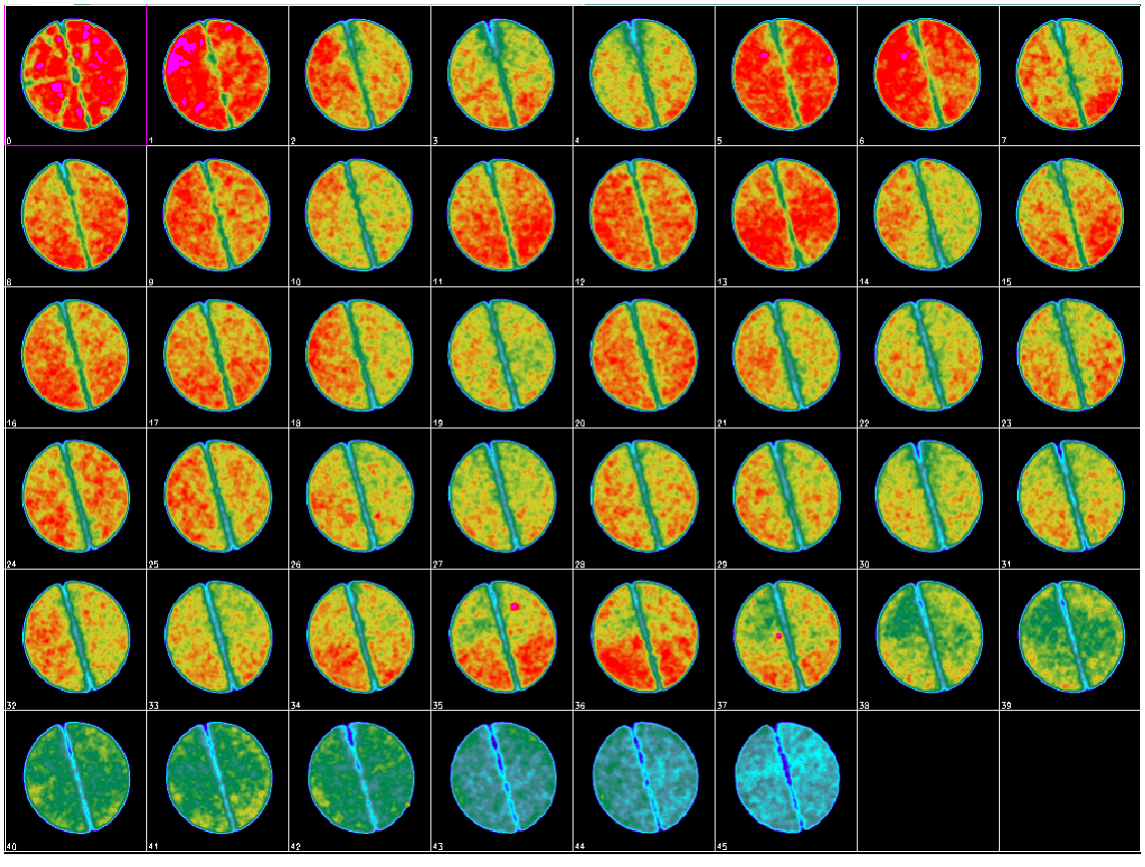

Fig. 4.72 – Vertical Slice Images of the Single Fractured Sandstone Core From Scan 1 (Images are tiled horizontally with the first image being the outlet and last image being the inlet.)

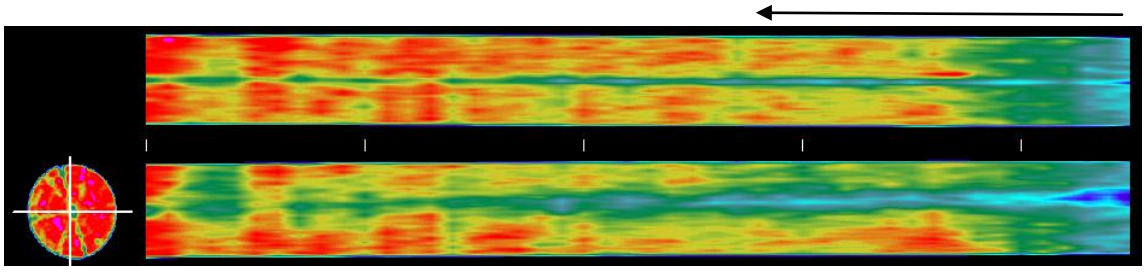

Fig. 4.73 – Scan 1 during the CO_2 Flooding in Single Fractured Sandstone (Arrow shows the direction of CO_2 flow and it applies to all the coreflood images throughout the thesis.)

The above scan was carried out after 0.47 PV of CO_2 had been injected. The CO_2 breakthrough did not occur yet at this time. In the slice images in Fig. 4.72, we can see a clear color distinction between the regions swept by CO_2 and the rest of the core which remains unswept. It can be concluded that the CO_2 mobility significantly reduced compared to the neat CO_2 case. In the vertical cross section (lower image) in Fig. 4.73 more CO_2 presence can be observed as a bright blue streak.

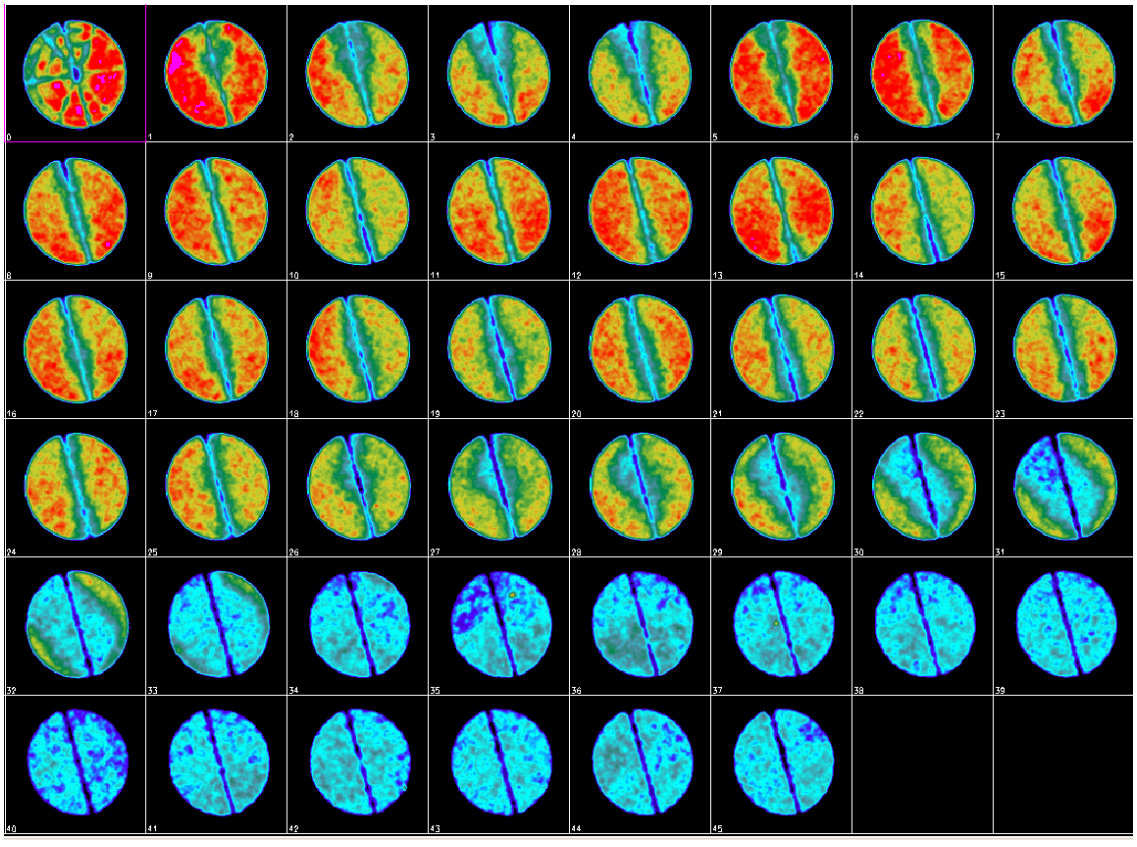

Fig. 4.74 – Vertical Slice Images of the Single Fractured Sandstone Core From Scan 2 (Images are tiled horizontally with the first image being the outlet and last image being the inlet.)

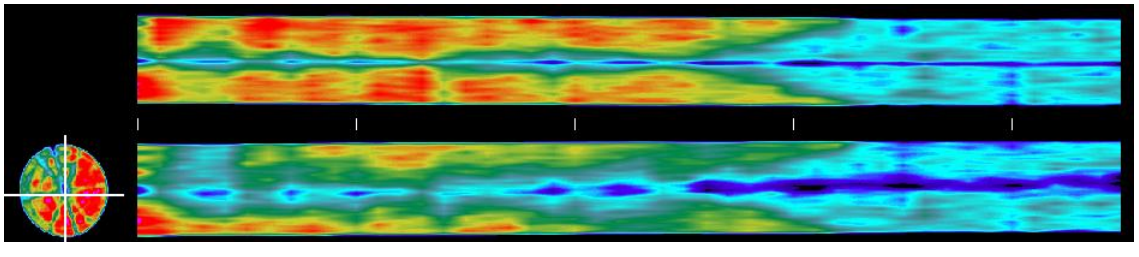

Fig. 4.75 – Scan 2 during the CO_2 Flooding in Single Fractured Sandstone

CO_2 breakthrough was observed after 1.26 PV of CO_2 injected. The CO_2 fluid coming out of the producing end solidified as dry ice form at atmosphere pressure. From both

the vertical slice images in Fig. 4.74 and the reconstructed slab images in Fig. 4.75 we can see the contrast between CO_2 invaded core regions and unswept regions. This is very different from all the previous neat CO_2 flooding cases; CO_2 mobility significantly decreased in the viscosified case here, allowing us to clearly to see the CO_2 flood front with high contrast. However, as expected, CO_2 flows through the fracture plane preferably. The increasing dark blue regions in the lower slab image in Fig. 4.75 suggest that CO_2 is concentrated in the fracture plane.

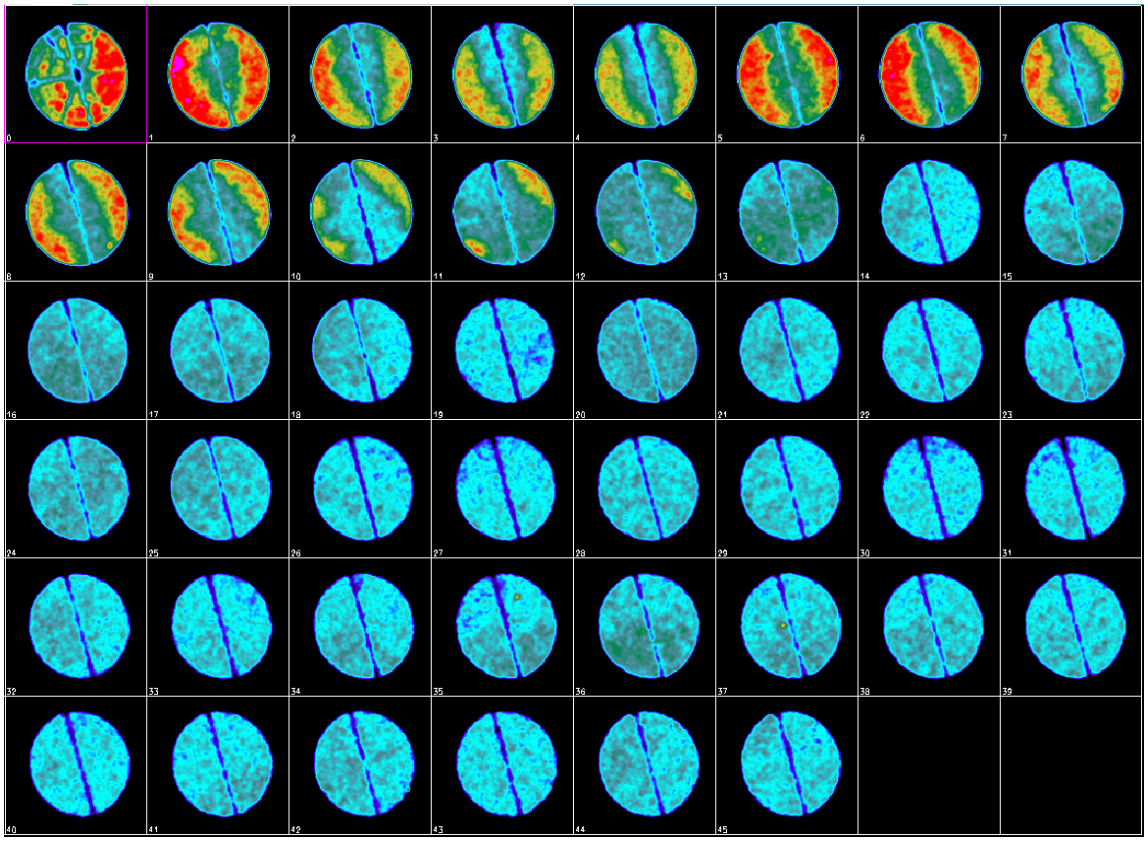

Fig. 4.76 – Vertical Slice Images of the Single Fractured Sandstone Core From Scan 3 (Images are tiled horizontally with the first image being the outlet and last image being the inlet.)

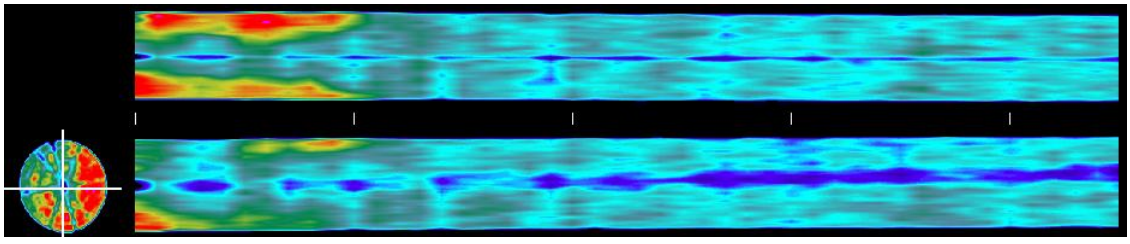

Fig. 4.77 – Scan 3 during the CO_2 Flooding in Single Fractured Sandstone

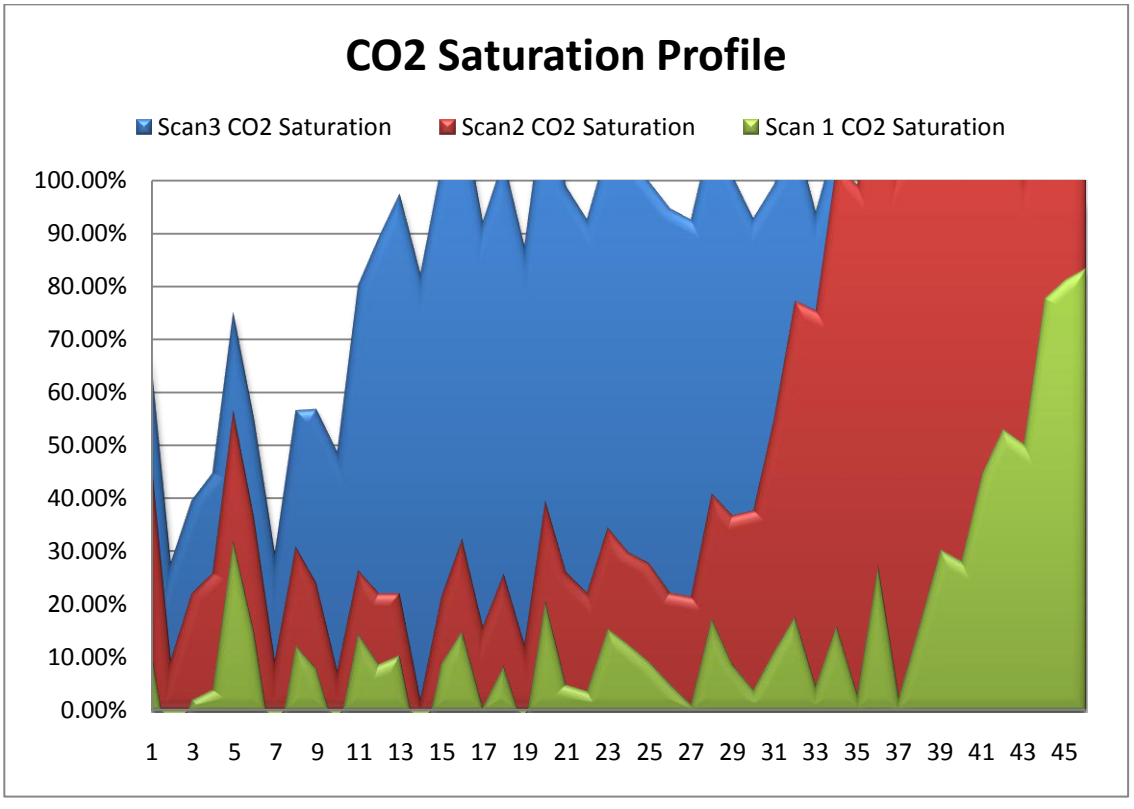

Fig. 4.78 – CO_2 Saturation Profile for Viscosified CO_2 Study (CO_2 injected from right to left)

CT images in Fig. 4.76 and Fig. 4.77 were taken at the end of CO_2 flooding after almost 6 PV of CO_2 was injected. As shown in the slab image, CO_2 reached most of the core regions as shown in bright blue color. It can still be seen that some parts of the core near the outlet remained red/yellow color, suggesting the presence of unswept oil.

CT data was processed and CO_2 saturations at different intervals of the CO_2 flooding is plotted in Fig. 4.78. We can see clearly that CO_2 saturation was distributed unevenly across the fractured core. From scan 1 to scan 3 the CO_2 saturation gradually increases towards the outlet side and we can see a sharp CO_2 saturation front progressing towards the left in the plot. The final CO_2 saturation was above 90% for most parts of the core; this is a much higher CO_2 saturation compared with the neat CO_2 control case in section 4.6.1. The following conclusion can be drawn by comparing the neat CO_2 and viscosified CO_2 coreflood experiments:

(1) Viscosified CO_2 breakthrough was slower than the control case and clear CO_2 flood front was observed. As a result, we can see significant CO_2 saturation distribution difference across the core.

(2) CO_2 saturation built up effectively in the CO_2 swept regions. The overall sweep efficiency was higher for the viscosified CO_2 than the neat CO_2 control case resulting in higher oil recovery.

The oil recovery in terms of pore volumes is represented in the Table 4.4.

Table 4.4 – Oil Recovery Table for Viscosified CO_2 Flooding (CO_2 Breakthrough around 1.26 PV CO_2 injected.)

PV CO_2 Injected	0.47	1.26	5.88
OOIP% oil produced	29%	56%	79%

The recovery data at different PV injected intervals shows a better recovery compared with the control case in Table 4.2; we can clearly see the recovery increases with time. Meanwhile, in the control, the recovery does not increase significantly after the CO_2 breakthrough occurred. Reading from the inlet and outlet pressure gauges, the pressure drop across the core for viscosified CO_2 flooding process is around 48 psi (Pressure Drop: 1830 - 1782 = 48 psi), while the control case has a pressure drop of only 8 psi across the core. This shows the increase of CO_2 viscosity after blending the CO_2 fluid with dodecamethylpentasiloxane in the viscosified CO_2 coreflood study.

4.6.3 Viscosified CO_2 Flooding Pressure Drop Test

In the previous lab studies, preliminary investigation on the formation of viscosified CO_2 flood front using the most simple dimethylsiloxane compound dodecamethylpentasiloxane was carried out. We observed differences between the neat CO_2 and viscosified CO_2 front. However, dodecamethylpentasiloxane is not an ideal candidate for increasing the viscosity of CO_2. Although its structural features make it highly soluble in CO_2, the molecular weight of this compound is too small (Mw. 385) to serve as an effective viscosifier; the study on this compound is beneficial in the sense of verifying the viscosifier mechanism.

The most direct evidence to prove the effectiveness of the viscosifier is the increase in pressure drop across the coreflood cell with the flow of viscosified CO_2 fluid. According to Darcy's law; flow rate across a porous medium can be calculated as:

$$Q = -(kA(P_{outlet} - P_{inlet}))/(\mu L) \quad \text{.....(4.2)}$$

Q: flow rate unit of volume per time

K: permeability

A: cross-sectional area

μ: viscosity of the fluid

P: pressure (inlet/outlet)

L: length of the porous medium

Equation 4.2 could be used as a measurement of viscosity in relation to pressure drop by the following format:

$$C/M = C\mu/k = \Delta P/Q \qquad (C = L/A) \quad \text{.....(4.3)}$$

M: Mobility

C: Constant related to the core size

The mobility related term C/M combines both viscosity and permeability regarding the specific fluid phase. If all other conditions remain the same, we can use the extent of increase in the $\Delta P/Q$ term to represent the proportional increase in the viscosity of the fluid phase. In our case the fluid is the viscosified CO_2 phase.

Details of the pressure drop test experimental procedures are provided below.

For the preparation of viscosifier solution, in all the coreflood tests the viscosifier is used together with the toluene cosolvent. The viscosifier chemical is 5% by weight in the final CO_2 fluid and the weight of the cosolvent is 10% by weight in the final CO_2 fluid. Before the coreflood experiment, a solution of viscosifier chemical and toluene cosolvent is prepared; the solid PVAc beads or liquid Polydimethylsiloxane fluid were mixed with toluene (10 grams of viscosifier chemical and 20 grams of toluene); the mixture was stirred overnight to obtain a homogeneous solution. The homogeneous solution was placed in the accumulator before filling the accumulator with 580 psi CO_2. After the accumulator was sealed and filled with 580 psi CO_2, the accumulator was

pressurized to 2000 psi by pump. Significant heat generation could be felt around the accumulator indicating the dissolution of the chemical into the CO_2 fluid. The mixture of viscosifier chemical, toluene cosolvent and CO_2 was left to equilibrize for hours until the heat stopped generating.

For the pressure drop test, unfractured Berea sandstone cores were used to obtain more significant pressure drop differences for neat CO_2 and viscosified CO_2. The sandstone core was placed in the oven and heated overnight before placing into the coreholder. An overburden of 3000 psi was applied to the core to be tested. Typically the CO_2 injection pressure was kept around 2000 psi. The CO_2 was left to flow until relatively constant fluid flow rate could be read from the Digital Injection Pump. Then the pressure drop across the coreflood cell was read from the digital pressure gauges. The sandstone core used was 1 inch in diameter and the lengths of the cores were around 4 inches. Each core was measured before the experiment to account for the differences in pressure drop.

Three pressure drop experiments were conducted to study the effectiveness of the viscosifiers.

(1) Neat CO_2

(2) 5% wt PVAc + 10% wt Toluene + CO_2

(3) 5% wt Polydimethylsiloxane + 10% wt Toluene + CO_2

The experimental results are listed in Table 4.5 as following; data from repeated runs are also included:

Table 4.5 – Pressure Drop Test Results

	Viscosifier Type	Inlet Pressure (psi)	Outlet Pressure (psi)	Flow rate (ml/min)	*C*/*M* Ratio*
Run 1	None	1911	1864	8.0	5.88
Run 2	PVAc	1899	1787	11.6	9.66
Run 3	PVAc	1901	1780	11.8	10.25
Run 4	Polydimethylsiloxane	1907	1881	4	6.50
Run 5	Polydimethylsiloxane	1907	1878	4.2	6.90
Run 6	Polydimethylsiloxane	1905	1867	8.38	4.53

*The pressure data has been calibrated before calculating mobility ratio

Values from Run 2 to Run 6 in Table 4.5 can be compared with the neat value of 5.88 in Run 1; we can see from the data that PVAc is a more suitable candidate for CO_2 viscosifier. The increase from Run 2 or Run 3 is almost twice the original neat CO_2 value. The polydimethylsiloxane in Run 3 to Run 6 does not give significant increase compared with the neat CO_2. To better understand the viscosifying mechanism,, we analyze further the behaviors of PVAc viscosified CO_2 using the CT scan technique as a preferred viscosifier chemical.

4.6.4 Viscosified CO_2 Flooding in Single Fracture Sandstone (PVAc)

In section 4.6.2 we completed the first set of study on dodecamethylpentasiloxane viscosified CO_2 flooding. The purpose was to observe the effect of viscosifier on the CO_2 flood front. After the pressure drop test in section 4.6.3 we are now focusing on the PVAc polymer as a better candidate for viscosifying CO_2. A different injection scheme was devised for PVAc viscosified CO_2 flood to better account for the effectiveness of viscosified CO_2. A total of 3 PV of CO_2 was injected; the first 1.5 PV of CO_2 was neat CO_2; after the first 1.5 PV PVAc, another 1.5 PV PVAc viscosified CO_2 was injected to obtain incremental oil recovery. The difference between this injection scheme and the neat CO_2 control case in section 4.6.1 is that in the latter case, all 3 PV injected were neat CO_2. The experimental scheme for section 4.6.1 and section 4.6.4 is summarized in Table 4.6; the scans represent the CT scans conducted to obtain the real time coreflood images:

Table 4.6 – CT-Scan Scheme for PVAc Viscosifier Study

	0.5 PV	1.0 PV	1.5 PV	2.0 PV	2.5 PV	3.0 PV
Control	Scan 1		Scan 2			Scan 3
PVAc case	Scan 1	Scan 2	Scan 3*	Scan 4	Scan 5	Scan 6

*After scan 3 viscosified CO_2 will be injected.

The PVAc viscosified CO_2 was prepared by 5wt% PVAc polymer and 10wt% toluene cosolvent. The CO_2 flood was conducted first using neat CO_2 for 1.5 PV injection; three scans were carried out at approximately 0.5 PV, 1.0 PV and 1.5 PV. After neat CO_2 injection, PVAc viscosified CO_2 was injected until 3.0 PV; another set of three scans was

carried out at approximately 2.0 PV, 2.5 PV and 3.0 PV. The total amount of CO_2 injected in this case is the same as the previous control case in section 4.6.1. Thus, it is reasonable to compare the final recoveries and CO_2 saturation.

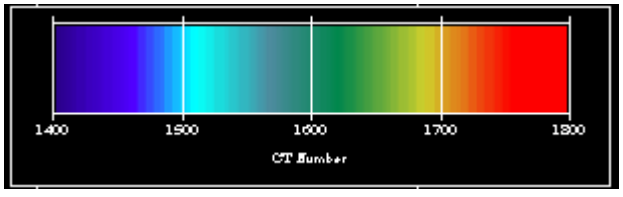

Fig. 4.79 – Color Spectrum (CT Number 1400~1800) for CT Images in Section 4.6.4

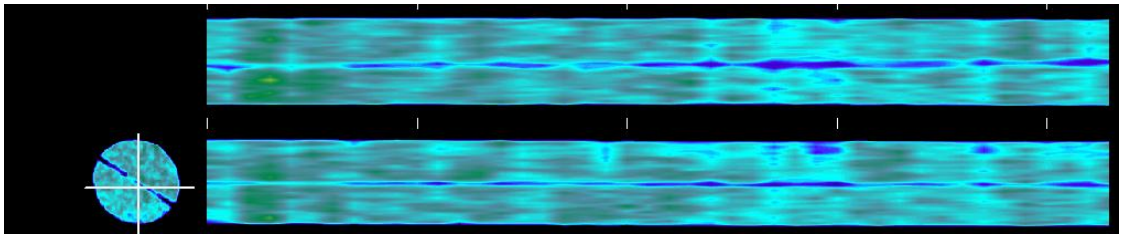

Fig. 4.80 – Scan of 100% CO_2 Saturated Single Fractured Sandstone Core

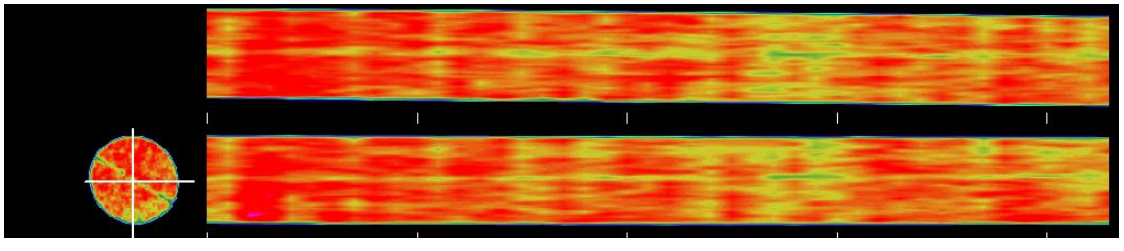

Fig. 4.81 – Scan of 100% Oil Saturated Single Fractured Sandstone Core

The color spectrum for this study is shown in Fig. 4.79. The two saturation images from Fig. 4.80 and Fig. 4.81 are similar with the neat CO_2 control study. This time the fracture orientation is more tilted towards the horizontal direction; it is less likely to

observe the oil and CO_2 saturation aggregation in the fracture plane since neither of the horizontal and vertical slabs is aligned with the fracture plane.

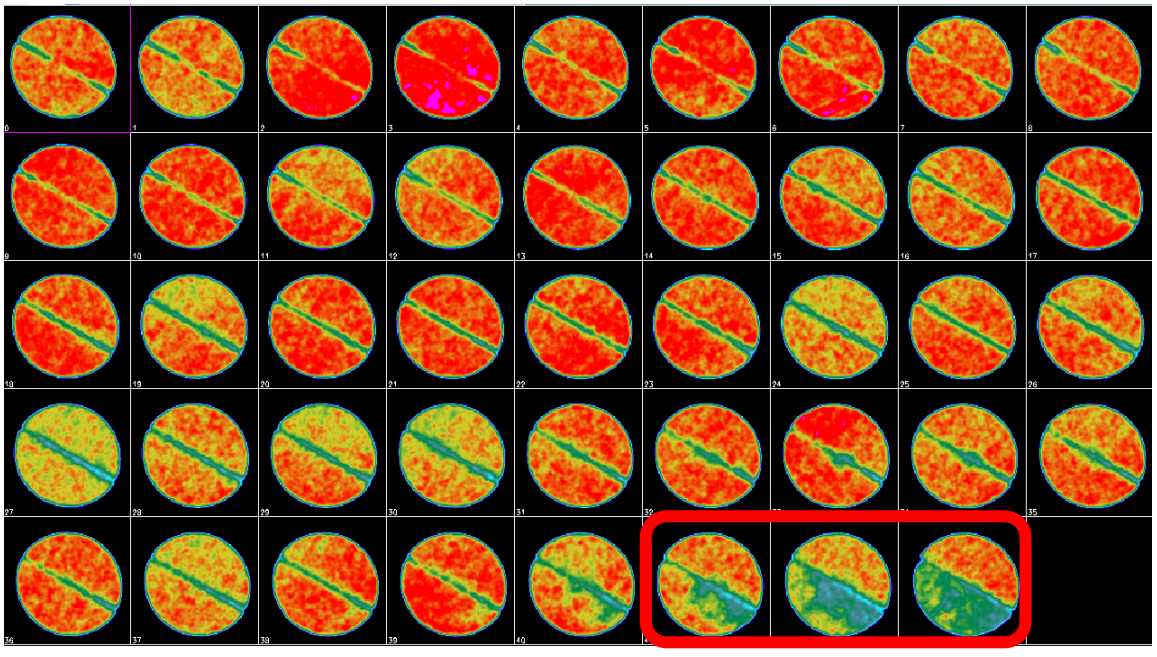

Fig. 4.82 – Vertical Slice Images of the Single Fractured Sandstone Core From Scan 1 (Images are tiled horizontally with the first image being the outlet and last image being the inlet.)

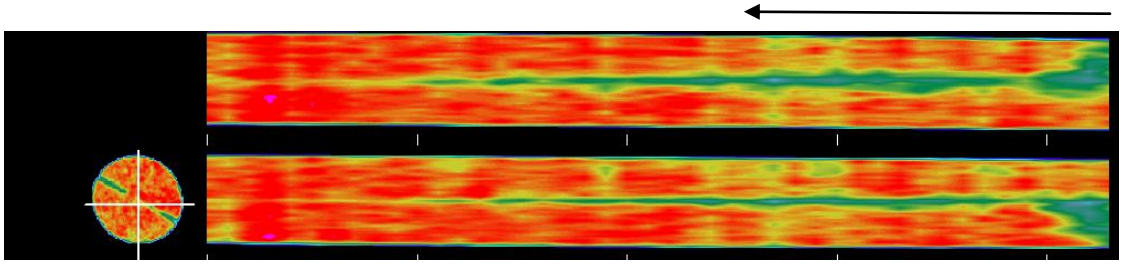

Fig. 4.83 – Scan 1 during the CO_2 Flooding in Single Fractured Sandstone (Arrow shows the direction of CO_2 flow and it applies to all the coreflood images throughout the thesis.)

From the slab images in Fig. 4.83 it is obvious that CO_2 has not broken through the core; the thin green streak of CO_2 gradually disappears towards the outlet end of the core. The CO_2 saturation contrast between two half cores in this case is also more significant; in the first three slices at the injection end in Fig. 4.82 (circled out by red rectangle), the CO_2 saturation will congregate primarily at the lower half of the core. This is also partly due to the fact that the fracture orientation in this case is more towards the horizontal direction and viscosifier chemical with high density preferably flows in the lower half of the core.

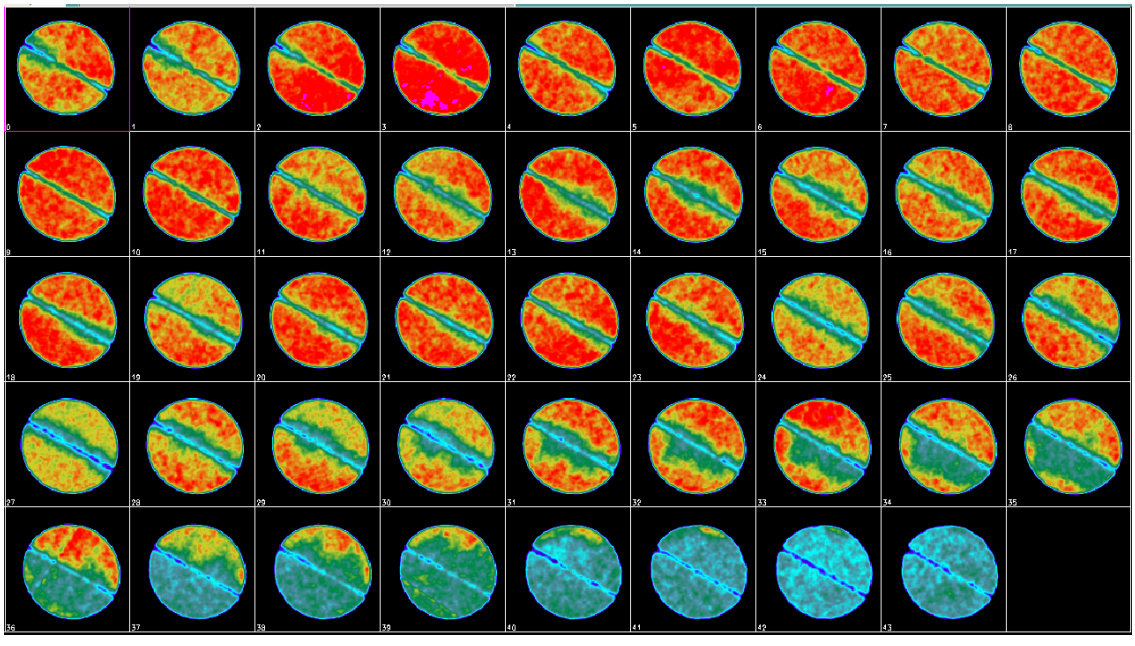

Fig. 4.84 – Vertical Slice Images of the Single Fractured Sandstone Core From Scan 2 (Images are tiled horizontally with the first image being the outlet and last image being the inlet.)

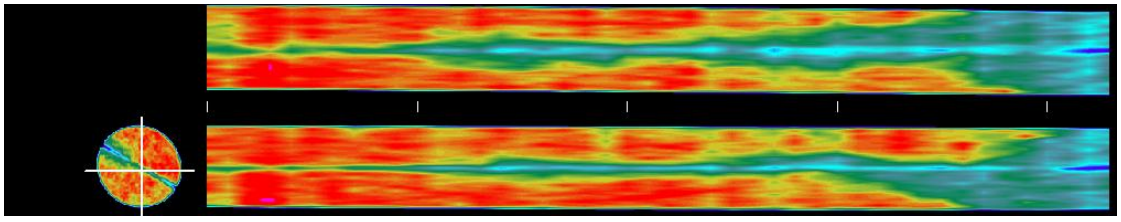

Fig. 4.85 – Scan 2 during the CO_2 Flooding in Single Fractured Sandstone

At 1.06 PV of neat CO_2 injection, it can be seen that CO_2 break through occurred in the form of green streaks towards the outlet in Fig.4.85. The neat CO_2 fluid cannot form a uniform front. The CO_2 fluid was mainly flowing through the fracture and a sharp transition of CO_2 saturation from injection point to the outlet was observed. In Fig. 4.84, the CO_2 saturation separation between two half cores is still obvious in the slices close to the injection point with the lower half of the core images green and the upper half image red/yellow.

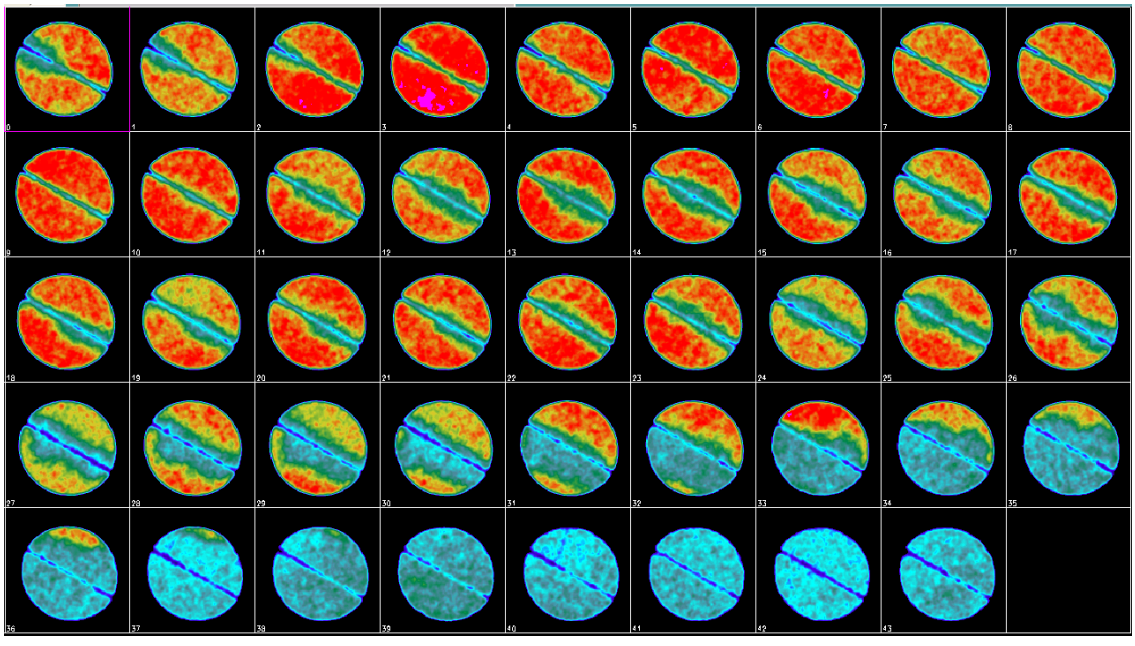

Fig. 4.86 – Vertical Slice Images of the Single Fractured Sandstone Core From Scan 3 (Images are tiled horizontally with the first image being the outlet and last image being the inlet.)

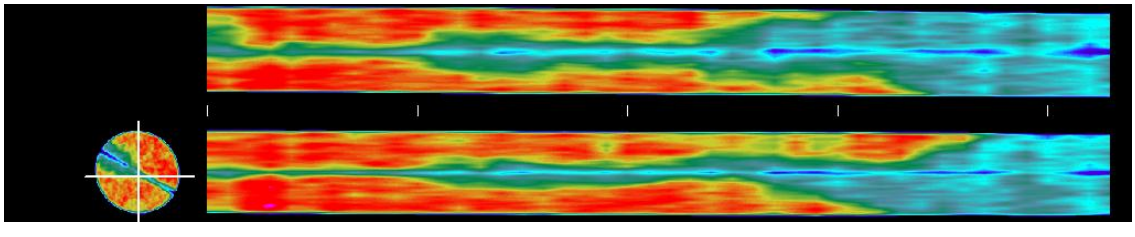

Fig. 4.87 – Scan 3 during the CO_2 Flooding in Single Fractured Sandstone

After 1.5 PV of CO_2 has been injected; we see from both the slice images in Fig. 4.86 and the slab images in Fig. 4.87 that the sweep effeciency is still not ideal espeically for the second half of the core which is close to the outlet. At this point the average CO_2 saturation is very close to the control case by processing the CT-data quantitatively; the average CO_2 saturation of the whole core after 1.5 PV for the neat CO_2 control case is

34% while the average CO_2 saturation of the whole core after 1.5 PV for the case in Fig. 4.87 is 38%; this shows that with or without PVAc visosifier, the CO_2 flood effeciencies are approximately the same.

After the 1.5 PV injection of neat CO_2, we changed the injection fluid to PVAc viscosified CO_2. Another three scans were carried out until a total of 3 PV CO_2 has been injected.

We scanned the core at normal pressure before resuming viscosified CO_2 flood to find out the oil distribution within the core as shown below.

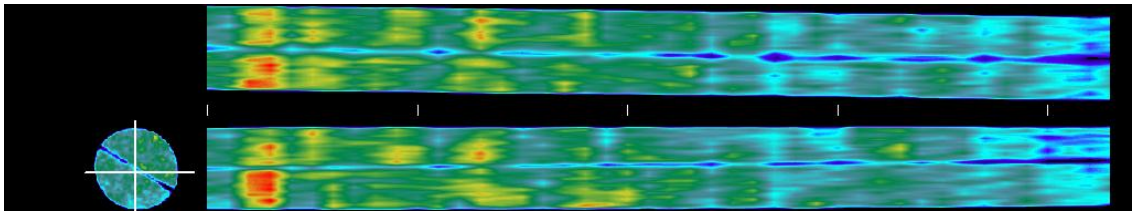

Fig. 4.88 – CT Image of Single Fractured Sandstone Core before Injecting PVAc Viscosified CO_2

The scan in Fig. 4.88 was taken at normal pressure without CO_2 presence. Therefore, the color tone shown was deviated from the other coreflood images in section 4.6.4. However, we can still see the trend of oil distribution in the fractured sandstone core. Towards the injection end, remaining oil saturation was low while towards the outlet end most of the oil still remained unswept.

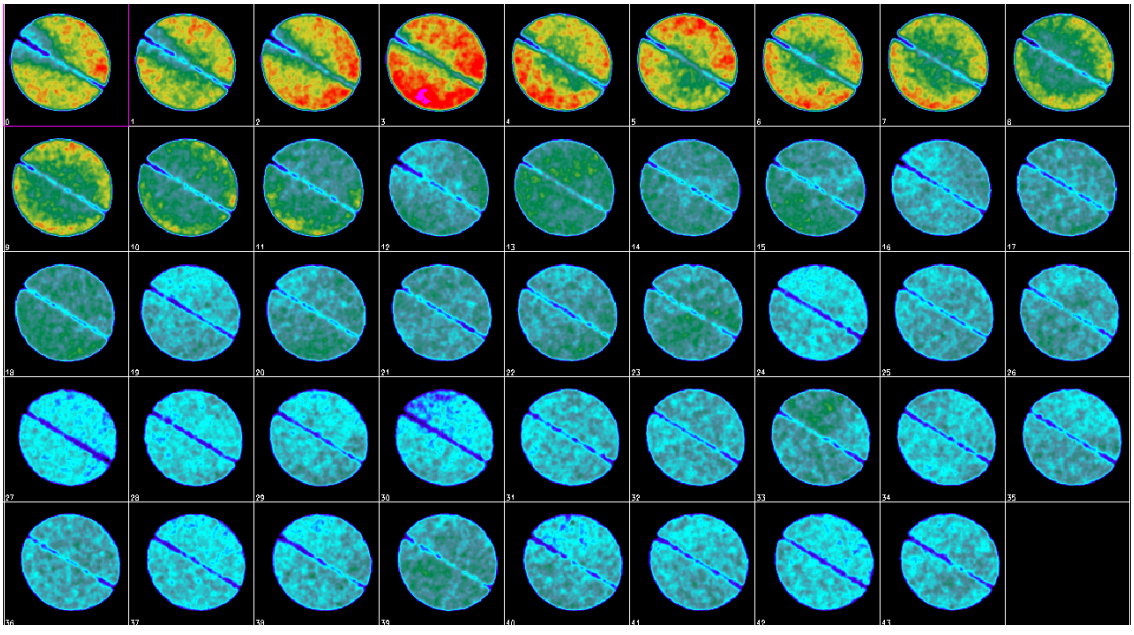

Fig. 4.89 – Vertical Slice Images of the Single Fractured Sandstone Core From Scan 4 (Images are tiled horizontally with the first image being the outlet and last image being the inlet.)

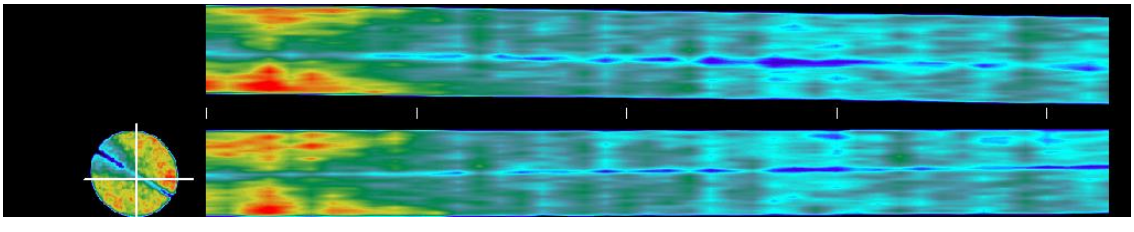

Fig. 4.90 – Scan 4 during the CO_2 Flooding in Single Fractured Sandstone

After resuming CO_2 flood, scan 4 was taken at around 2.0 PV (an incremental of 0.5 PV viscosified CO_2 injected.). Now the slice images in Fig. 4.89 and the slab images in Fig. 4.90 show steady progress of the CO_2 flood front and a very good sweep of the regions covered by CO_2. For almost 4/5 of the core in Fig. 4.90, the sandstone matrix color changed into complete blue indicating predominant CO_2 presence.

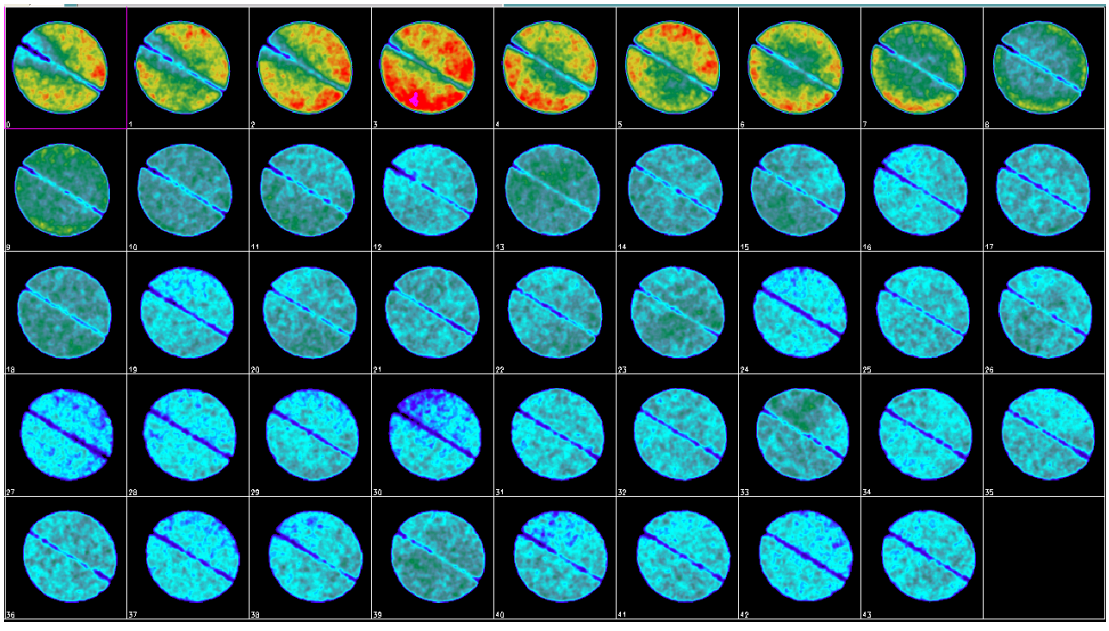

Fig. 4.91 – Vertical Slice Images of the Single Fractured Sandstone Core From Scan 5 (Images are tiled horizontally with the first image being the outlet and last image being the inlet.)

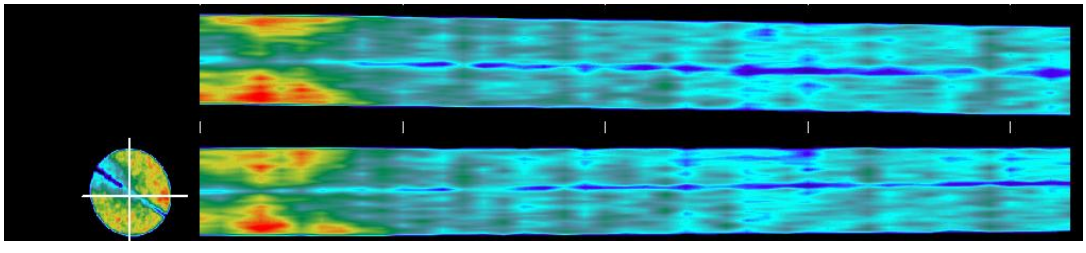

Fig. 4.92 – Scan 5 during the CO_2 Flooding in Single Fractured Sandstone

As more CO_2 was injected; the CO_2 progressed towards the outlet. This can be seen better by carefully observing the color change of the slice core images in Fig. 4.91 close to the outlet end with green CO_2 spot growing bigger in the center. We can also notice the rebuilding of CO_2 flood front; the transition interface between CO_2 (blue) and oil

occupied matrix (yellow/red) was not as sharp as the neat CO_2 flooding images in Fig. 4.92.

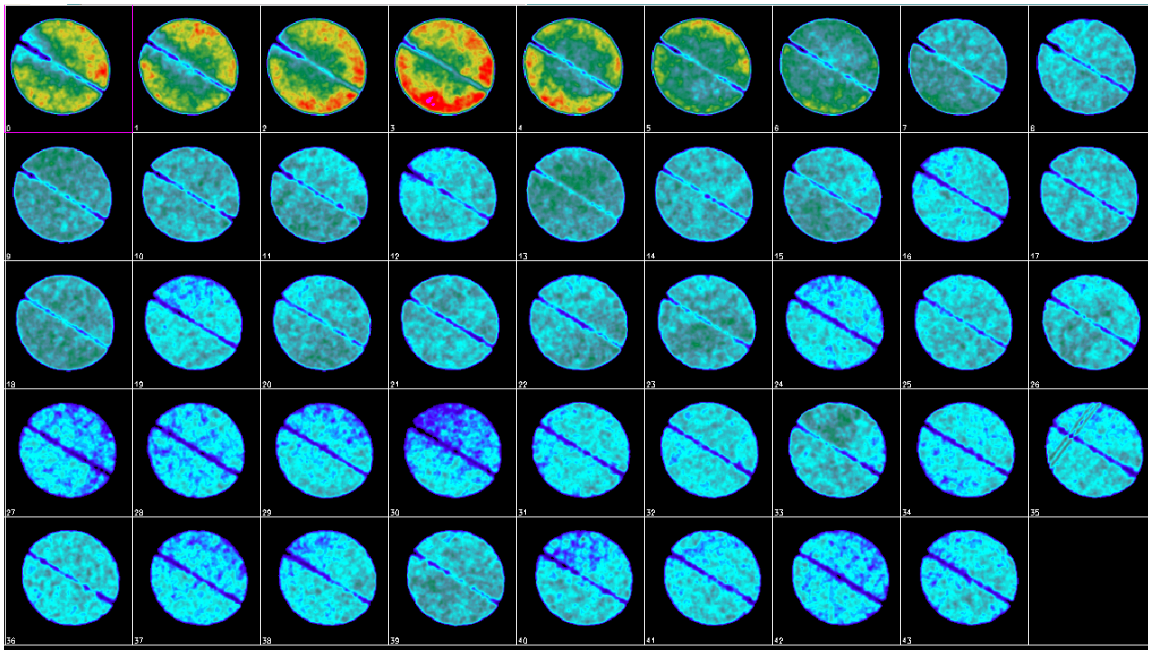

Fig. 4.93 – Vertical Slice Images of the Single Fractured Sandstone Core From Scan 6 (Images are tiled horizontally with the first image being the outlet and last image being the inlet.)

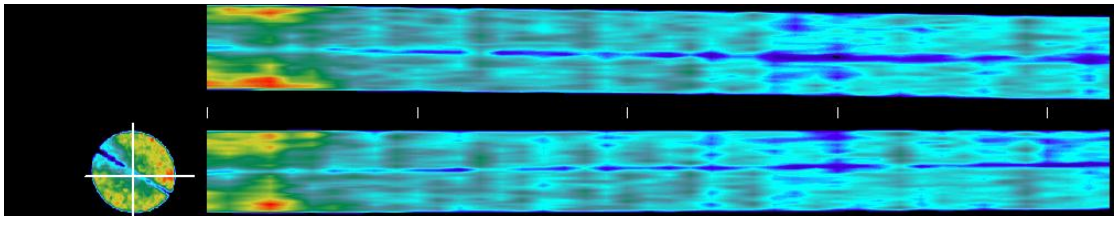

Fig. 4.94 – Scan 6 during the CO_2 Flooding in Single Fractured Sandstone

Scan 6 was the last scan taken after 2.99 PV CO_2 was injected (an incremental of 1.5 viscosified CO_2 injected). As shown in both slab images in Fig. 4.94 and slice images in

Fig. 4.93, most of the core regions were swept by CO_2. The final saturation images in Fig. 4.94 clearly reveal the difference between applying PVAc viscosified CO_2 and applying neat CO_2 for the same amount of CO_2 (3 PV) injected.

Table 4.7 – Oil Recovery Table for Neat/Viscosified CO_2 Flooding (CO_2 Breakthrough around 0.8 PV CO_2 injected)

	Neat CO_2 Injection			Viscosified CO_2 Injection		
PV CO_2 Injected	0.49	1.06	1.56	2.06	2.55	2.99
OOIP% oil produced	21%	46%	58%	68%	74%	76%

The recovery data is shown in Table 4.7. As the final recovery reveals, the 76% recovery is significantly higher than the 67% recovery for the neat CO_2 injection case using the same amount of CO_2 (3 PV).

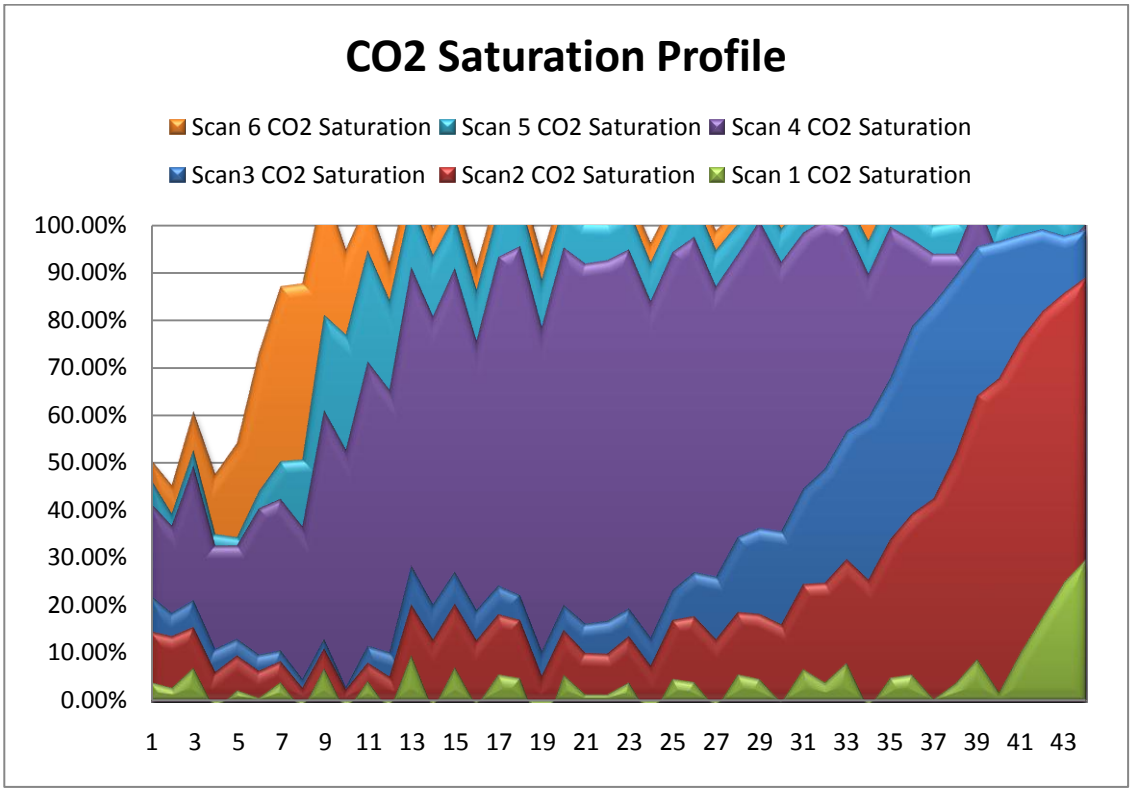

Fig. 4.95 – CO_2 Saturation Profile for PVAc Viscosified CO_2

The CO_2 saturation distribution profile along the core was obtained by processing the CT data quantitatively as shown in Fig. 4.95. Scan 1-3 represent neat CO_2 injection and scan 4-6 represent viscosified CO_2 injection. There are several noticeable features in the saturation plot. First of all, after the transition from neat CO_2 to viscosified CO_2, the CO_2 saturation increases significantly. Also worth noticing is the shape of CO_2 front; for scan 1-3 the decline of CO_2 saturation along the core is relatively slow with a tilted slope while for scan 4-6 the transition from CO_2 saturated zone to unswept zone is relatively steeper with a more vertical slope compared with neat CO_2.

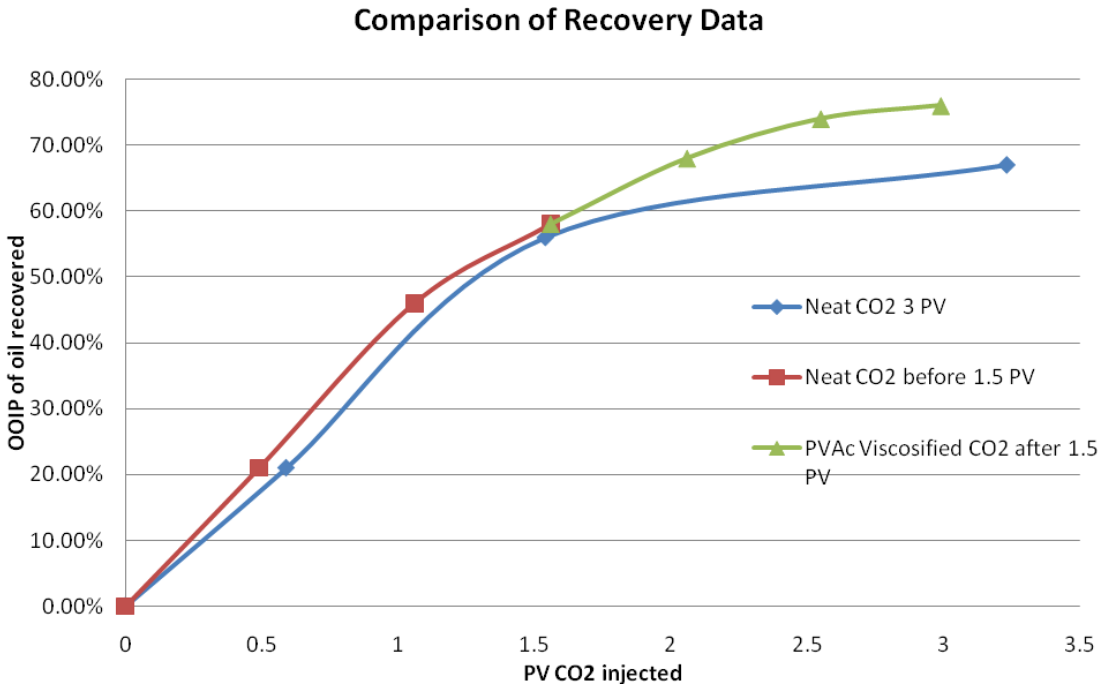

Fig. 4.96 – Oil Recovery with Pore Volume of CO_2 Injected Comparison

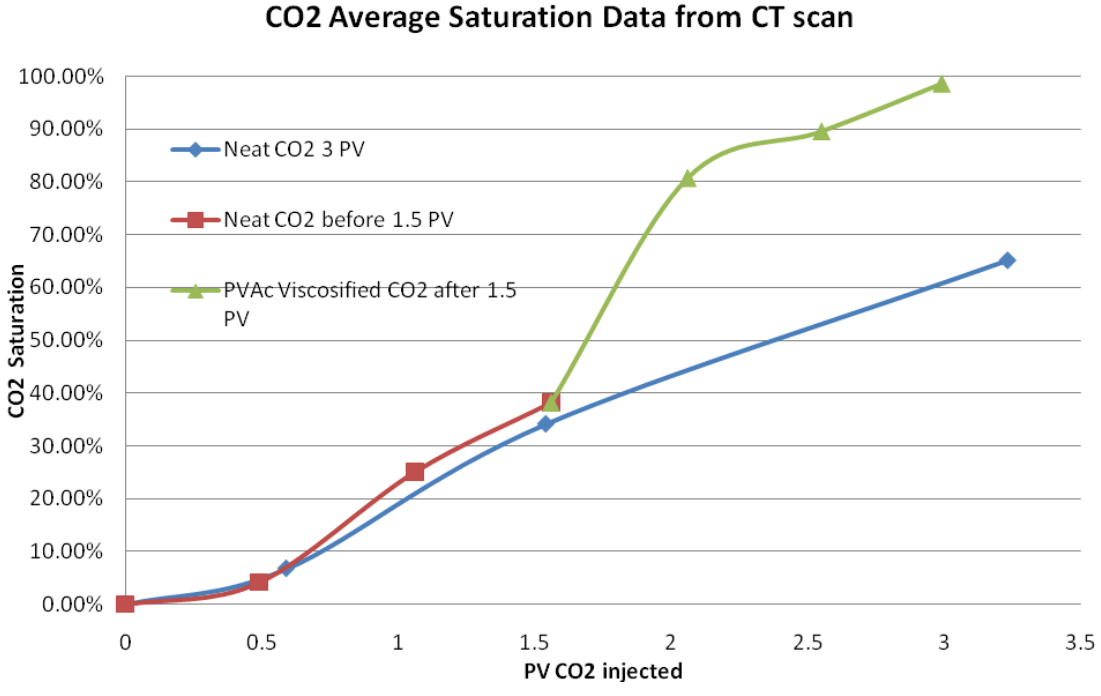

Fig. 4.97 – CO_2 Saturation with Pore Volume of CO_2 Injected Comparison

Finally, two plots in Fig. 4.96 and Fig. 4.97 summarize two CO_2 coreflood studies in section 4.6.1 and section 4.6.4. The first plot of recovery curve comparison is obtained from the oil recovered with pore volumes of CO_2 injected. CO_2 saturation curve comparison in Fig. 4.91 is obtained by calculating quantitatively the average saturation of CO_2 across the whole core region with different pore volumes of CO_2 injected.

In the recovery data plot in Fig. 4.96, the increasing trend before 1.5 PV for both cases is almost identical; the OOIP recoveries for both cases end up at around 55 % after the 1.5 PV CO_2 has been injected. Once PVAc viscosifier is applied to the viscosifier case, the two recovery curves begin to divert into different directions. The final recovery of viscosifier case is around 76 % while the neat CO_2 case reaches 67 % recovery in the end. It is a solid proof that more oil was recovered from the PVAc viscosified case.

In the CO_2 saturation plot in Fig. 4.97, similarly before 1.5 PV the saturation curves stay almost the same for both cases; both curves reach around 35 % CO_2 saturation after 1.5 PV of neat CO_2 has been injected. After 1.5 PV when the PVAc viscosifier is adopted, the viscosifier curve suddenly rises above the neat CO_2 control curve. This is also very evident in the CO_2 flood images from the different extent of color change. Finally after 3 PV of total CO_2 is injected for both cases, the average CO_2 saturation of the viscosifier case reaches 98% while the final average CO_2 saturation for the control case only reaches 56%. The difference in the final CO_2 saturation here is more significant compared with the final recovery data, possibly due the lag between the volume of the real oil recovered and volume of the oil collected at the outlet as caused by the dead oil volume within the coreflood system.

4.7 Simulation Study of Viscosified CO_2 Flooding

We plan to carry out initial simulation research to anticipate the benefits of using viscosifier chemical in CO_2 EOR production. A general CMG black oil simulation model using pseudo-miscible consideration is developed based on field data (Field P) provided by an oil company. Interpretations on the general model are provided when permeability heterogeneity and CO_2 mobility differences are considered. Finally a CO_2 pattern flood model of Well A from data provide by the same oil company and the simulation results are presented to provide predictions on possible operation scenarios.

4.7.1 Simulation of Viscosified CO_2 Flooding by CMG

Since the CO_2 viscosifier technology has not been widely used in the actual field production, there have been very few reports on the simulation of viscosified CO_2 flooding. Our research on possible methods for the simulation of viscosified CO_2 flooding process leads to the following three major approaches:

(1) Compositional Simulation (GEM): Using the specific key word *VISCOSITY, the component viscosities of the reservoir oil and CO_2 can be specified and the fluid viscosities during the simulation calculations can be computed using the direct mixing-rule. Viscosities depend on fluid composition.

(2) Black Oil Simulation (IMEX): The pseudo-miscible consideration in the black-oil IMEX module of CMG software allows us to define CO_2 as a solvent slug which is miscible with the oil. In this model we can modify the phase behaviors of the solvent phase (CO_2) directly, especially for the CO_2 viscosity change with pressure. We can also define the miscibility pressure from solvent phase data. Viscosities depend on fluid composition and pressure.

(3) Composition Simulation (GEM): Viscosities can be computed from the Jossi, Stiel and Thodos correlation.[35] This approach utilizes a low-pressure viscosity evaluation by Herning-Zipperer and Yoon-Thodos formulas. To modify and demonstrate the viscosifer effect on the CO_2 fluid, we can modify the CO_2 fluid pseudo-critical volume parameters used for computing the mixture critical volume in the Jossi, Stiel and Thodos correlation. Viscosities depend on fluid composition, temperature and pressure.

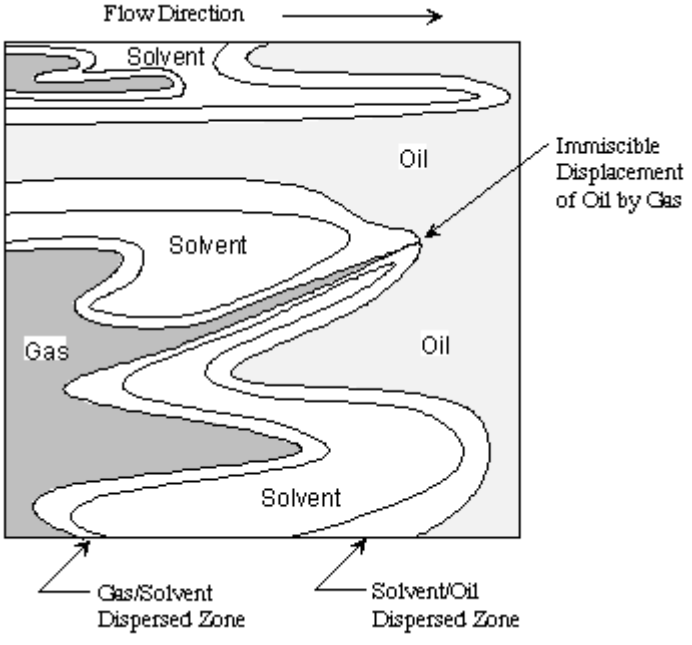

Fig. 4.98 – Three-Component Miscible Displacement in a Grid Block (Todd and Longstaff 1972)[36]

Fig. 4.98 depicts a typical fluid distribution within a grid block for pseudo-miscible consideration. The solvent phase is displacing oil under miscible condition and a possible gas phase will be following the solvent phase to drive the displacement forward. However, it is possible that the oil/solvent and solvent/gas dispersion zones will merge;

in this case the solvent saturation will drop due to gas presence and miscibility will probably be lost. We have eliminated the factor of gas here, and only use CO_2 as the solvent phase, so the displacement will occur under miscible conditions.

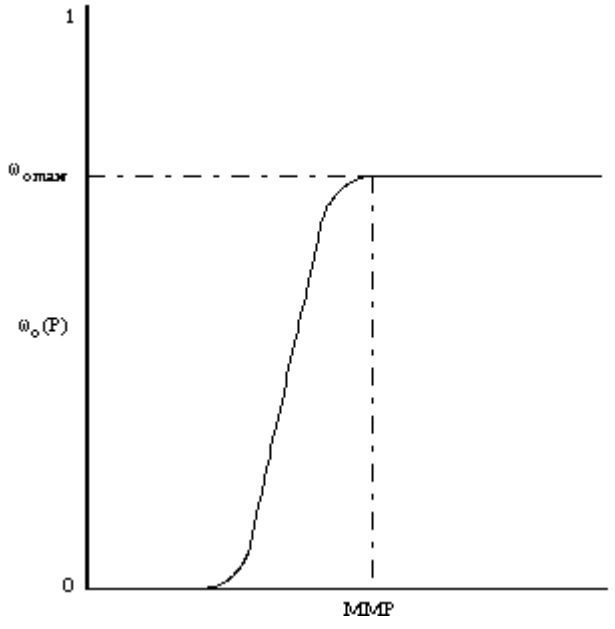

Fig. 4.99 – Mixing Parameter *vs.* Pressure

Fig.4.99 shows the mixing of solvent and oil. The mixing extent is controlled by a pressure-dependent mixing parameter, $\omega_o(P)$. This parameter specifies the ratio of solvent mixing with oil. We can read from the figure that when pressure reaches the minimum miscibility presure (MMP), the mixing parameter reaches maximum. On the other hand, when the pressure is well below MMP, the mixing parameter is close to 0 and the solvent displacing oil process is immiscible displacement. This mixing parameter curve can be adjusted in history-matching study to match the field performance.

4.7.2 General Reservoir Model

Sensitivity study comparing different extents of CO_2 viscosity increase was performed on the general reservoir model. A 1/8 of a 5 spot CO_2 pattern flood was set up as shown in Fig. 4.100.

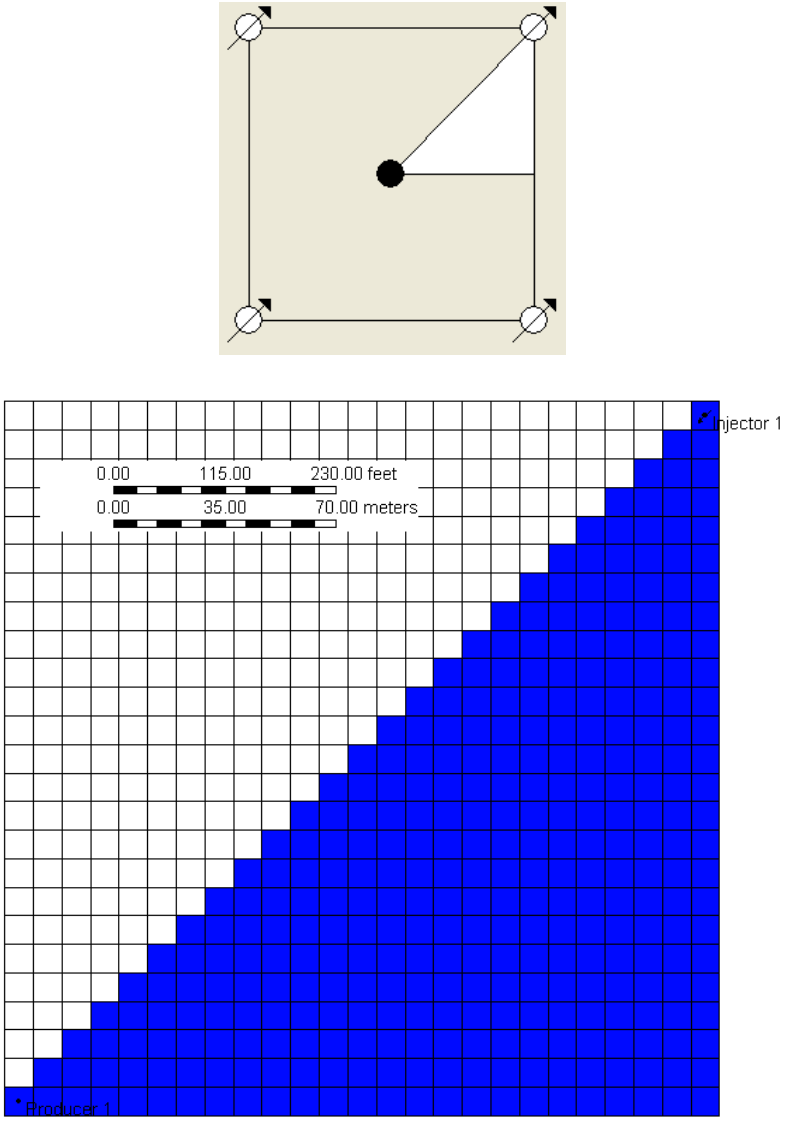

Fig. 4.100 – 1/8 of a 5-Spot CO_2 Pattern Flood Model

Reservoir data: reservoir data was extracted from company provided data. Cartesian grid 24×24×10 was used with 30 ft horizontal spacing and 10 ft vertical spacing. 10 layers, divided into two regions verticals, were set up; from top to bottom the first 1-5 layers have a permeability of 1 mD while the 6-10 layers have a permeability of 10 mD. Grid top (1,1,1) was set to 9400 ft in reference to the Field P data and WOC (Water Oil Contact) was set to 9500 ft to satisfy a 30% water saturation from the Field P data. Reference pressure was set to be 4300 psia according the average of Units in Field P. 3D representation of the reservoir model with the permeability distribution is provided in Fig. 4.101:

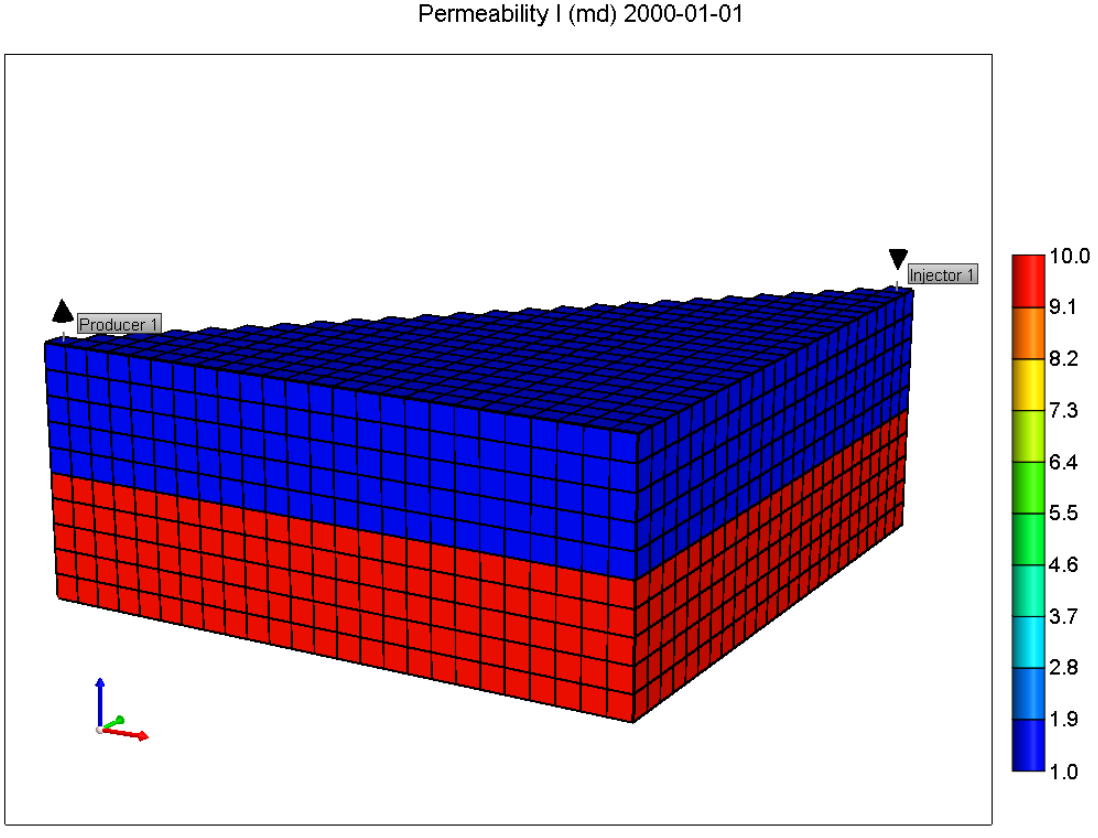

Fig. 4.101 – 3-D Representation of the CO_2 Pattern Flood Model

Viscosity Data: In our simulation study, we assumed the same mixing paramter-pressure relationship for both viscosified CO_2 and neat CO_2. The major difference between different simulation runs is the viscosity increase of CO_2 fluid phase under the same pressure. The plot in Fig. 4.102 below shows the data we use for the neat CO_2 flooding case. The red curve is the mixing parameter $\omega_o(P)$ changing with pressure. We can see from the plot that above MMP (1500 psi) the mixing parameter becomes almost constant. The blue curve is the viscosity of neat CO_2 changing with pressure. We see that at reservoir pressure conditon (around 4300 psi), the CO_2 viscosity is still relatively low (0.05 cp).

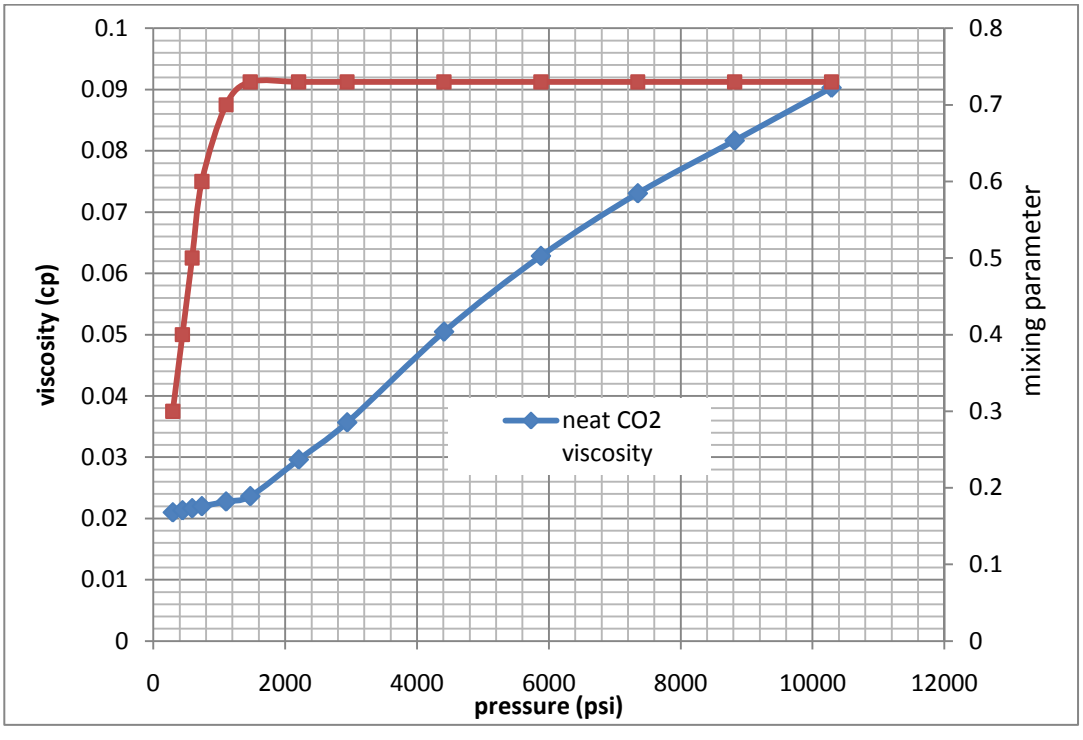

Fig. 4.102 – Mixing Parameter and CO_2 Viscosity Changing with Pressure

To illustrate the possible CO_2 viscosifier effects, we plotted a series of curves as shown in Fig. 4.103 to represent the new viscosity-pressure relationship. We set the maximum viscosity increase as 20 fold according to literature and then put in two other less significant viscosity increasement in between the neat CO_2 case and the 20 fold viscosity increasement case as 5 fold and 10 fold separately.

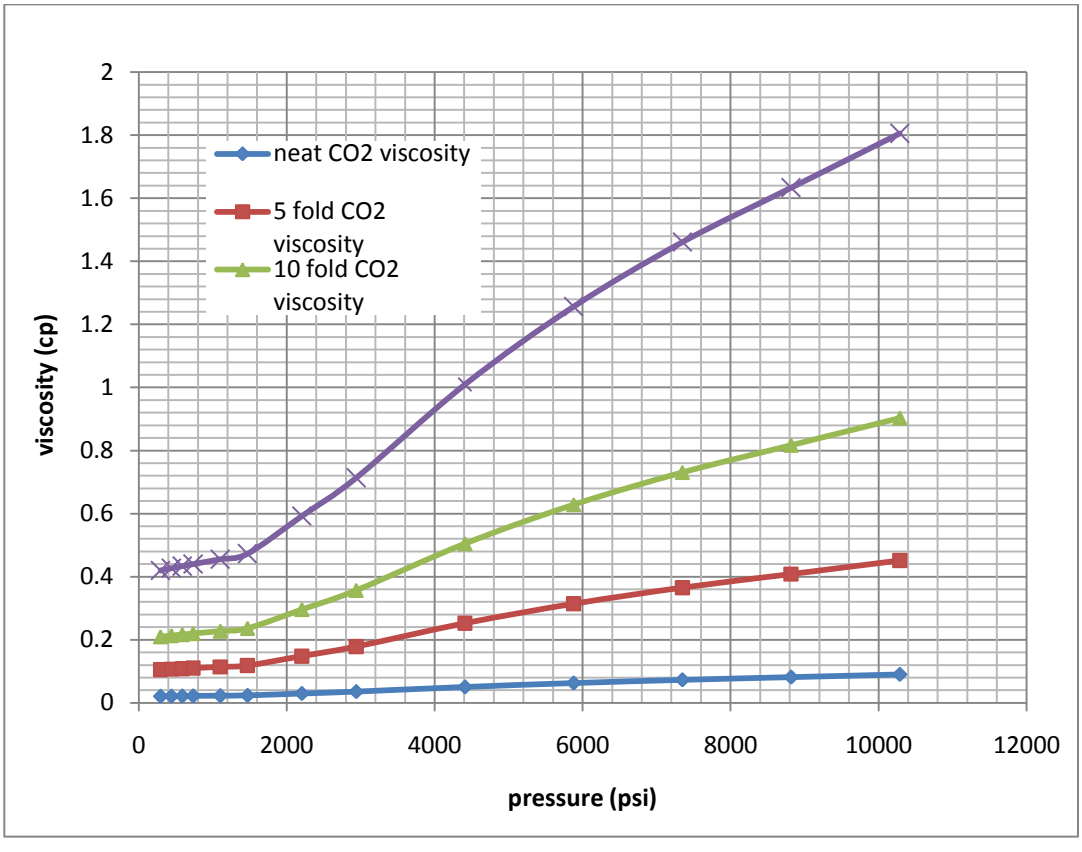

Fig. 4.103 – Different Viscosity Curves Changing with Pressure

Simulation Results Discussion: Since high permeability contrast exists between the 1-5 layers and 6-10 layers in our model (1 mD *vs* 10 mD), we expected that this contrast would cause early breakthrough of CO_2 in the higher permeability layers thus resulting in low overall recovery. We decided to perform a sensitivity study on the extent of CO_2

viscosity increase. The following three runs were conducted for the same reservoir model with different viscosity of the CO_2 injected:

Case 1: Neat CO_2 flooding

Case 2: 10 fold viscosity increase CO_2 flooding

Case 3: 20 fold viscosity increase CO_2 flooding

Simulation was conducted for the time period of 4 years starting from 2001-1-1 to 2004-1-1. For the injection well, CO_2 was injected at 500,000 SCF/d rate. For the production well, the oil production was set to 200 bbl/d (constraint) from the beginning. We first looked at the solvent saturation distribution in the cross section of the 1/8 5-spot CO_2 pattern flood:

Saturation Color Scal

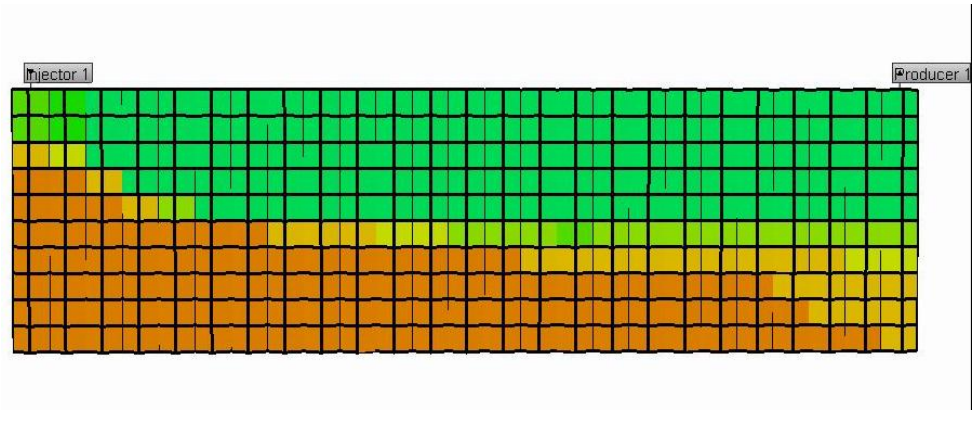

Neat CO_2 flooding

Fig. 4.104 – Solvent Saturatoin Distribution for Three Different Simulation Runs

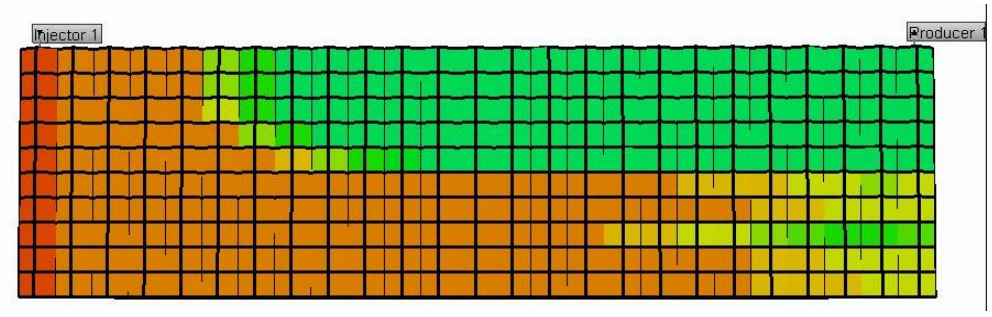

10 fold viscosity CO_2 viscosity increase CO_2 flooding

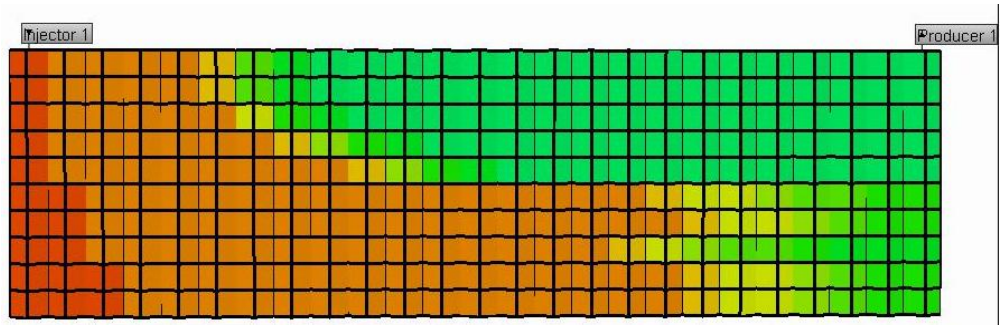

20 fold viscosity CO_2 viscosity increase CO_2 flooding

Fig. 4.104 – Continued

CO_2 saturation final distributions in the model are shown in Fig. 4.104. For the neat CO_2 flooding Case 1, most of the CO_2 injected flows through the high permeability layers 6-10 and we can see that almost no solvent (CO_2) is present in layer 1-5 even at the end of the simulation. For 10 fold viscosity increase Case 2, the sweep effeciency increases for the first 5 layers but still there is a great preference for CO_2 to flow through the high permeability layers 6-10. The 20 fold viscosity increase Case 3 has a slightly better sweep effeciency compared to that in Case 2, but the major advanatage is that in Case 3 the solvent front progress is delayed in layer 6-10 compared with Case 2. Therefore, we can conclude that Case 3 has the latest CO_2 breakthrough time.

The oil rate and cumulative oil production rate curves for the 4 years' simulation are plotted for each case in Fig. 4.105 and Fig. 4.106, respectively. As can be read from the oil rate plot, the constant 100 bbl/d production rate starts to decline as time goes by. For Case 1 with neat CO_2, oil rate starts to decline around 2002-1. For Case 2 with 10 fold viscosity increase, oil rate starts to decline around 2002-6. For Case 3 with 20 fold viscosity increase, oil rate starts to decline around 2002-9. In other words, viscosifier delays the time at which oil rate starts to decline. The same trend is reflected in the cumulative oil production case, more oil is produced in the long run after the application of viscosified CO_2; the time at which cumulative oil production curves divert from each other corresponds to the oil rate decline time in the oil rate curve.

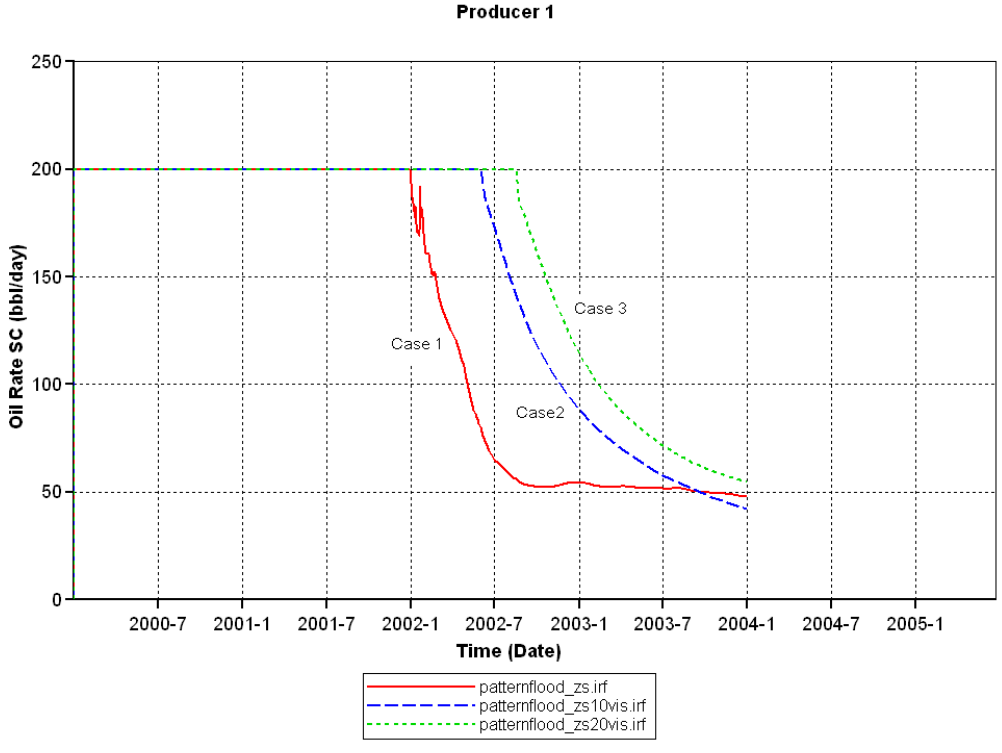

Fig. 4.105 – Simulation Results: Oil Rate for Case 1 to Case 3

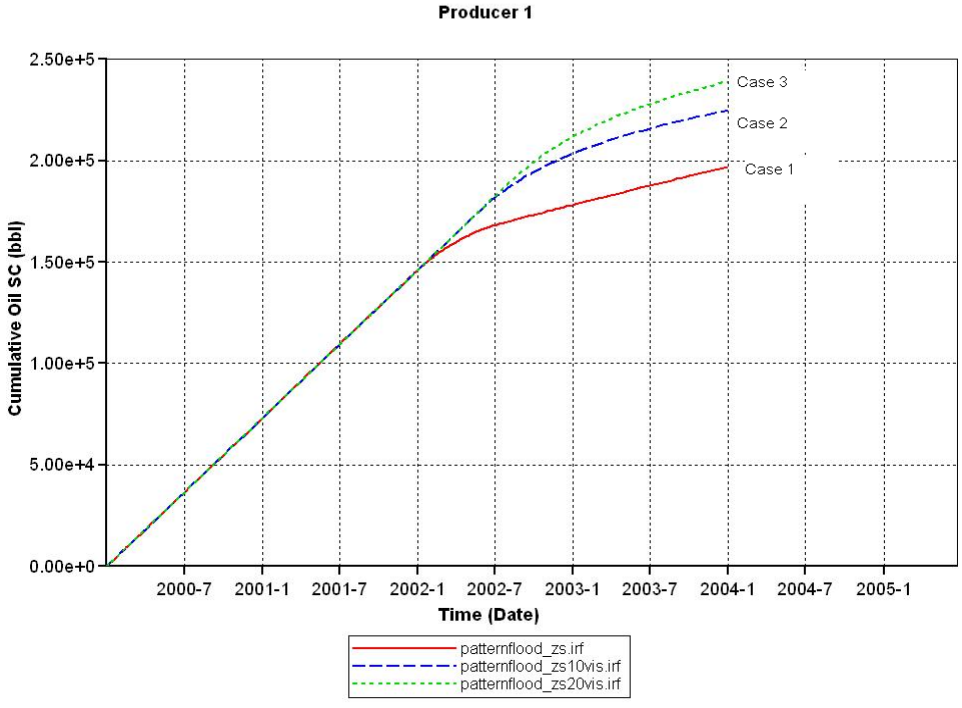

Fig. 4.106 – Simulation Results: Cumulative Oil Rate for Case 1 to Case 3

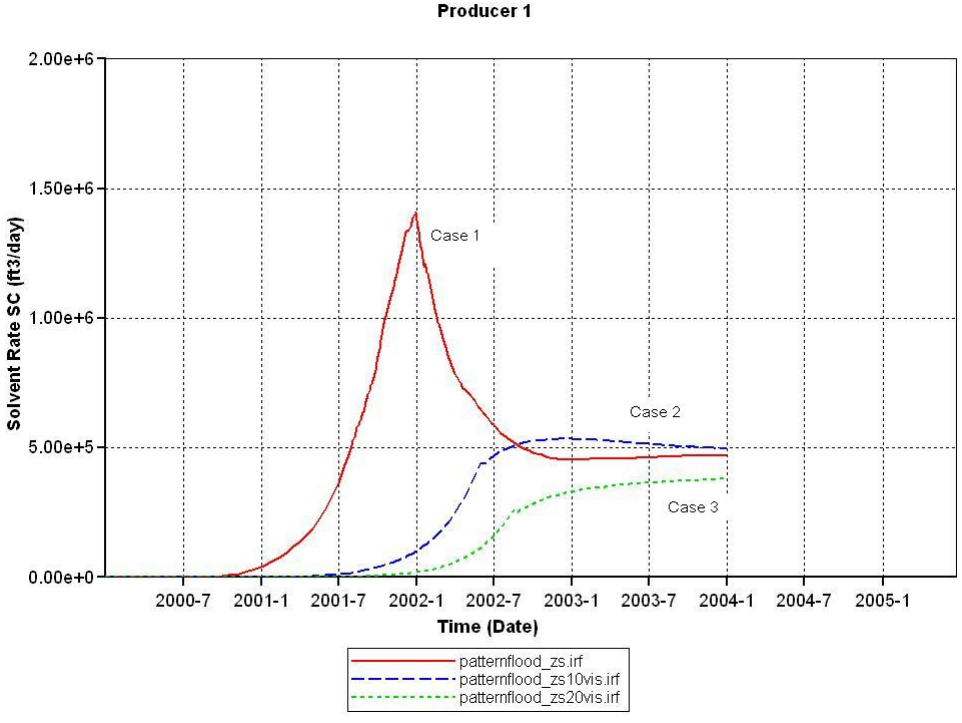

Fig. 4.107 – Solvent Production Rate for Case 1-3

The solvent production rate curves are also plotted for each case in Fig. 4.107. (solvent here equals CO_2, solvent production means CO_2 production.) For Case 1 with neat CO_2, the CO_2 breakthrough time is as early as 2000-8; for Case 2 with 10 fold viscosity increase, the CO_2 breakthrough occurrs around 2001-7; for Case 3 with 20 fold viscosity increase, the CO_2 breakthrough occurrs around 2002-1. When no viscosifier is added for CO_2 flooding, Case 1 curve reaches the peak around 2002-1 at which the CO_2 production rate is around 1400,000 SCF/d. This rate is is much higher than the CO_2 injection rate of 500,000 SCF/d; this discrepency causes rapid reservoir pressure depletion. For Case 1 and Case 2, the CO_2 production rate stabalizes around 500,000 SCF/d after 2002-9, an indication that most of the CO_2 is flowing through the high permeability layer without sweeping the low permeabilty zones. This case presents very low utilization of CO_2 injected. For Case 3, at the end of our simulation time the CO_2 production rate is around 400,000 SCF/d, which, is still below the CO_2 injection rate 500,000 SCF/d. Thus, Case 3 definitely outperforms Case 1and Case 2 in terms of efficient CO_2 utilization.

Case 1 well-bottom hole pressure and well block pressure

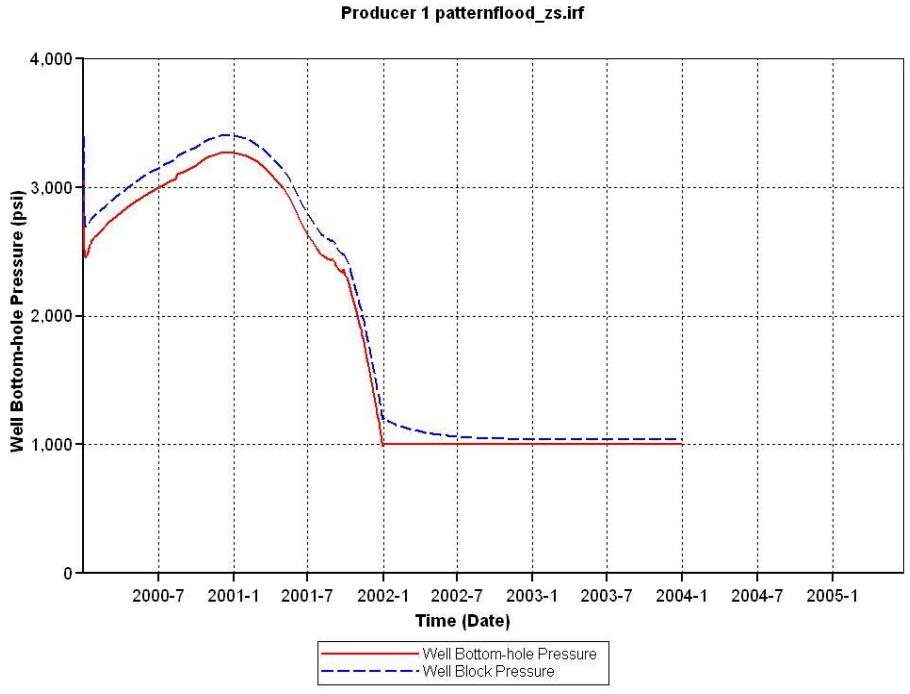

Case 2 well-bottom hole pressure and well block pressure

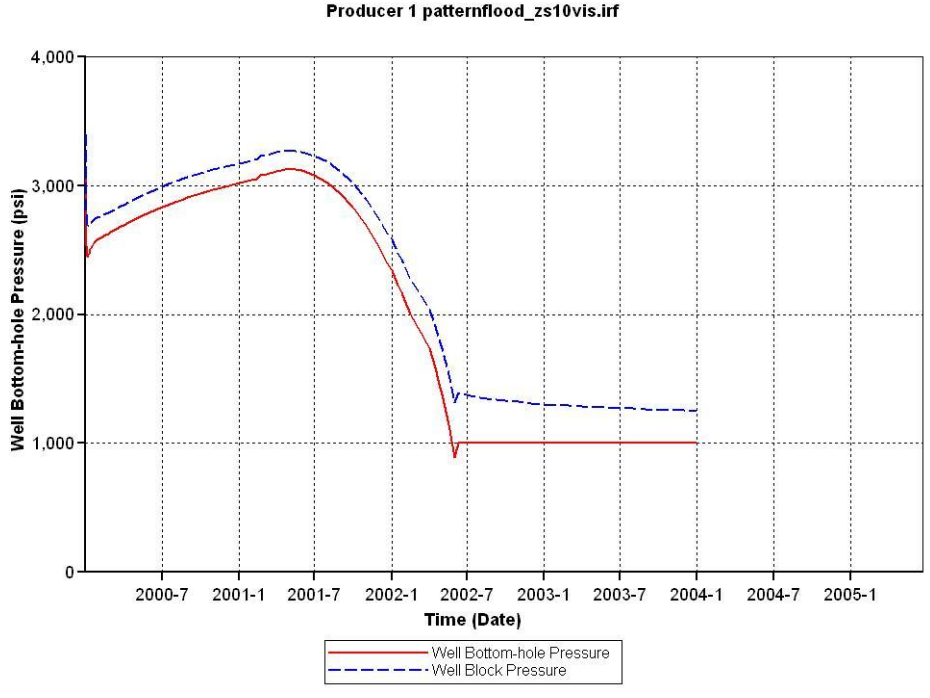

Fig. 4.108 – Well Block Pressure vesus Well Bottom-hole Pressure for Case 1-3

Case 3 well-bottom hole pressure and well block pressure

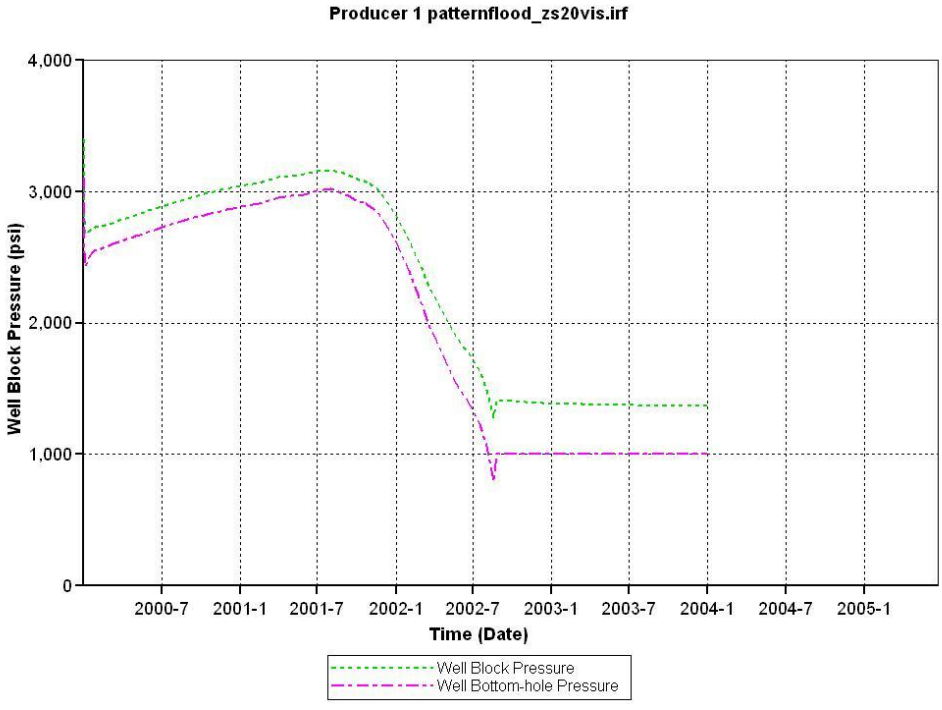

Fig. 4.108 – Continued

Finally, a comparison between well bottom-hole pressure and well block pressure is made for each case in Fig. 4.108. Note that the peak of the well block pressure occurrs at almost the same time of CO_2 breakthrough in Fig. 4.107, because reservoir pressure starts to decline sigfinicantly after CO_2 breakthrough occurrs at the production well. The well bottom hole pressure constraint is set to be 1000 psi, so when the well block pressure drops below or equal to 1000 psi, no oil is produced. From Case 1 to Case 3, it is obvious that the neat CO_2 Case 1 has a very rapid well block pressure drop and towards the end of production the two curve almost overlaps, resulting in a very low oil production rate. For Case 2 and Case 3, the application of viscosifiers delays the drop of

well block pressure below 1000 psi with the same CO_2 injection rate. It can be concluded CO_2 viscosifier application also helps maintain the reservoir pressure.

4.7.3 Simulation of Viscosified CO_2 Flooding for Well A

Based on all the previous simulation study results we combined the basic pseudo-miscible simulation model with data from the company and applied to the Well A in Field P. Using well-testing data and log data, we can get a more realistic representation of a CO_2 pattern flood case. Reservoir performance characteristics will be evaluated through this well model. The basic simulation data are listed in Table 4.8.

Table 4.8 – Well A Model Properties and Injection Details

Reservoir Description	
Length (ft)	24 × 30
Width(ft)	24 × 30
Number of Pay Zones	4
Number of Layers	10
Depth of Top of the Reservoir (ft)	9150
Pay Zones (ft)	9149.6 – 9173.2
	9293.0 – 9314.3
	9455.4 – 9460.3
	9521.0 – 9527.6
Reference Pressure (Psi)	4000
Temperature (^oF)	90

Table 4.8 – Continued

Reservoir Description	
Porosity (Variable)	0.18, 0.15, 0.18, 0.18
Permeability (md)	0.92, 0.0704, 16.7, 33
Kz/Kx	0.1
Dip , degree	0
Operation Details	
Number of Producing Wells	1
Number of Injecting Wells	1
Maximum Production Rate (STB/D)	100
Minimum Production BHP (psi)	1000
Maximum Injection Rate (million SCF/D)	0.5 (2 Years)
Injection Well Skin	0
Injection Gas Composition	100% ,CO_2
Simulation Period	2 years

The 3-D representation of the pattern flood model is presented in Fig. 4.109.

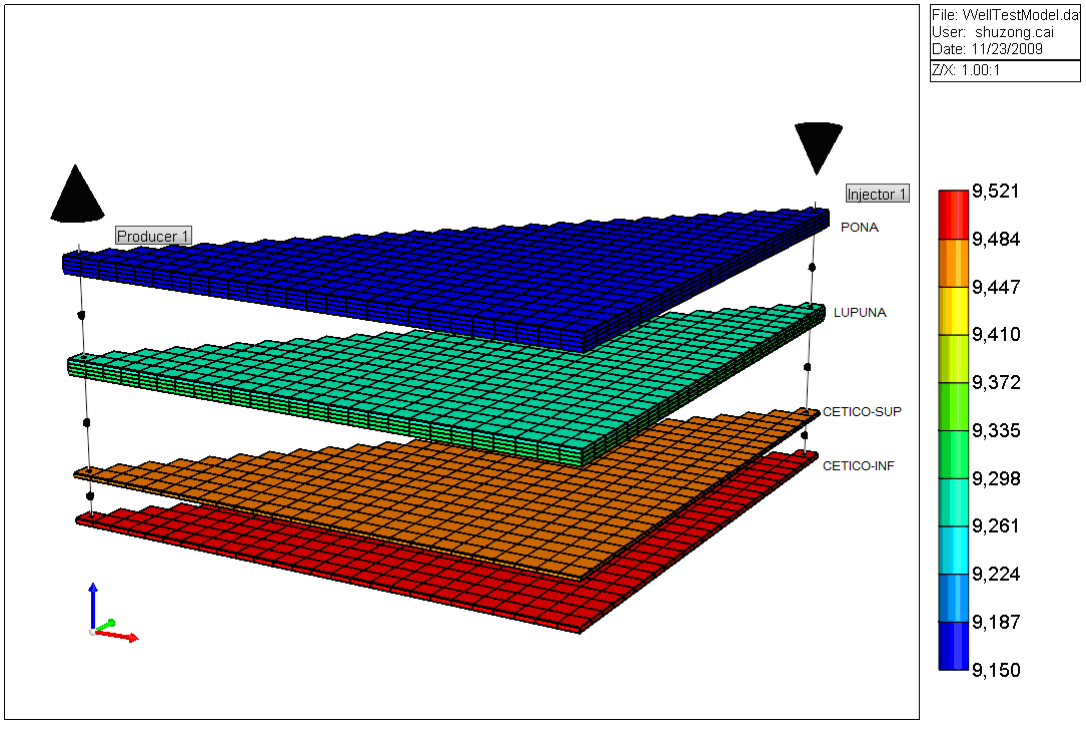

Fig. 4.109 – 3-D Representation of Well A Model

The simulation study starts from 2000-1 and ended at 2002-1 for two years. Two cases are considered in this simulation study.

Case 4: Neat CO_2 flood

Case 5: 20 fold viscosity increase CO_2 flood

The simulation ran for 2 years and various parameters are compared at the end of 2 years for the two cases. Results from the following reservoir performance parameters are presented: Oil Production Rate, Cumulative Oil Production Rate, CO_2 Production Rate and CO_2 Saturation.

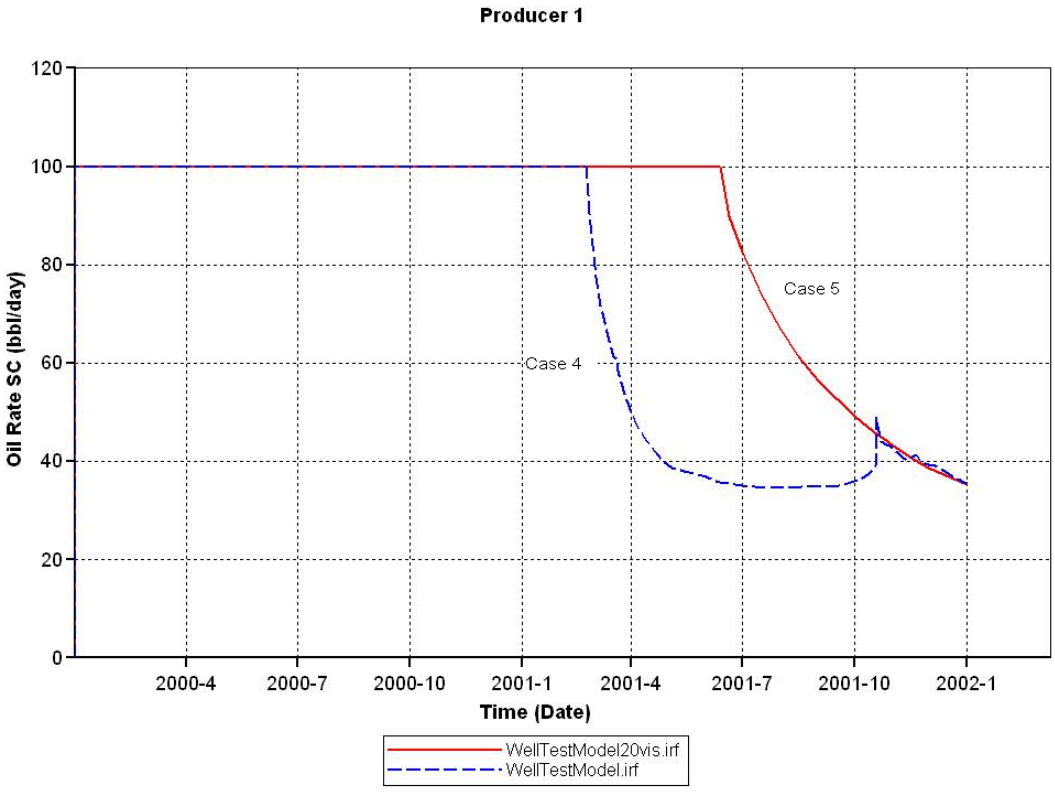

Fig. 4.110 – Oil Rate for Case 4 and Case 5

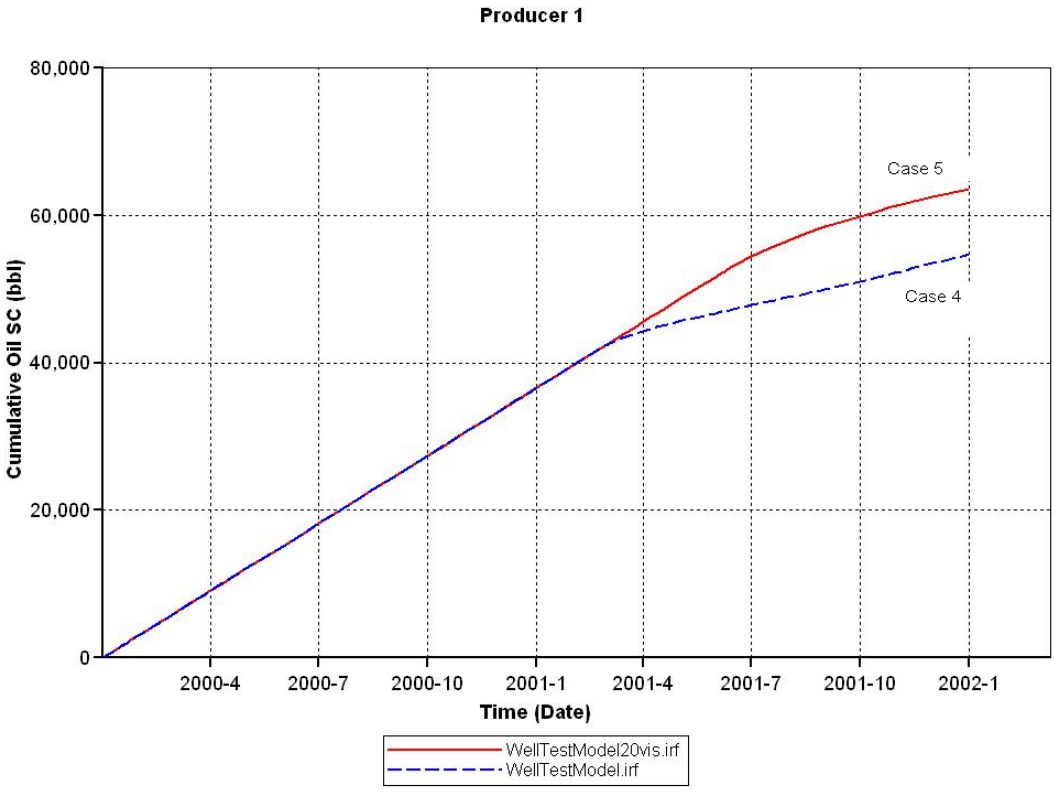

Fig. 4.111 – Cumulative Oil Rate for Case 4 and Case 5

Significant difference can be observed between Case 4 with neat CO_2 and Case 5 with 20 fold viscosified CO_2 in terms of oil production. In Fig. 4.110 the oil rate for Case 4 starts to decline round 2001-3 and the oil rate for Case 5 starts to delince around 2001-6; the application of viscosifers delays the oil rate decline. The high permeability contrast between layered pay zones contributes to the early oil rate decline. For the cumulative production rate in Fig. 4.111, viscosified Case 5 gives more cumulative production in the long run in comparison with neat CO_2 flooding Case 4 as expected.

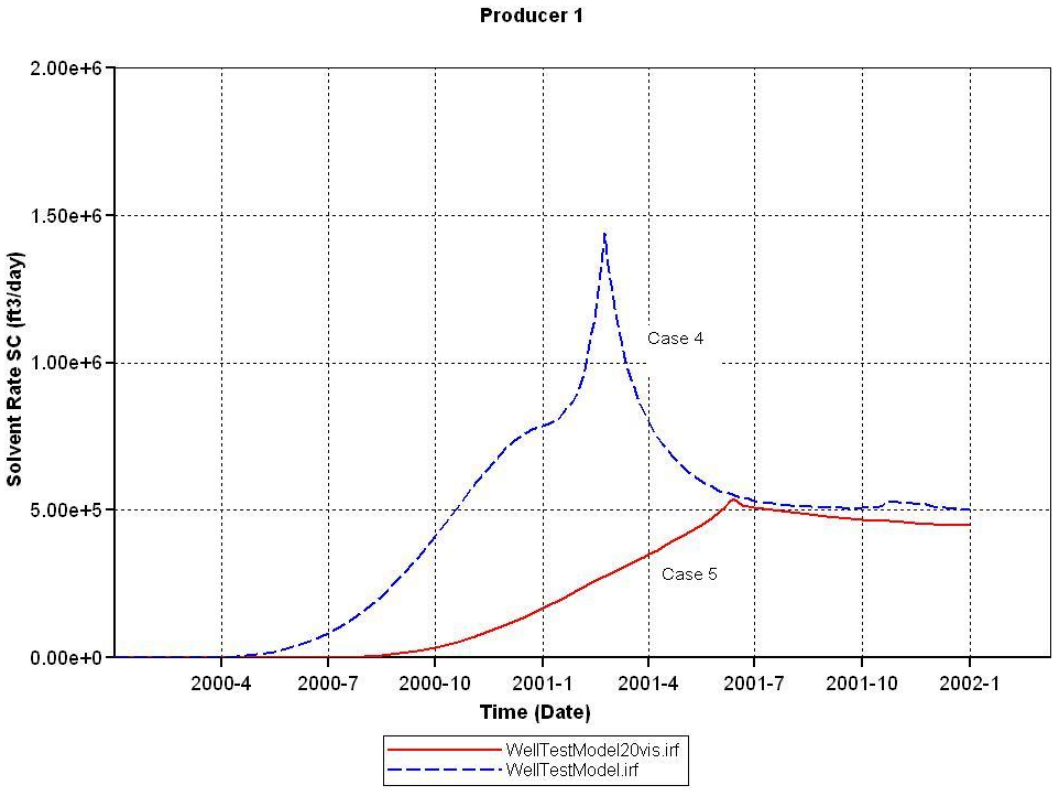

Fig. 4.112 – Solvent Production Rate for Case 4 and Case 5

In Fig. 4.112 of solvent rate plot, solvent means CO_2 fluid. The CO_2 breakthrough for case 4 of neat CO_2 occurrs around 2000-4, while the CO_2 breakthrough for Case 5 of 20 fold CO_2 viscosity increase occurrs around 2000-8. For the neat CO_2 flooding case, the CO_2 production reaches a peak rate of 1400,000 SCF/d which is much higher than the CO_2 injection rate of 500,000 SCF/d. Such high production rate can cause reservoir pressure depletion problems. The time when CO_2 production rate equals to CO_2 injection rate (500,000 SCF/d) for both cases is towards the end of simulation time after 2001-7. This indicates the presence of highly permeable layers which conducts CO_2 flow directly from injection well to production well.

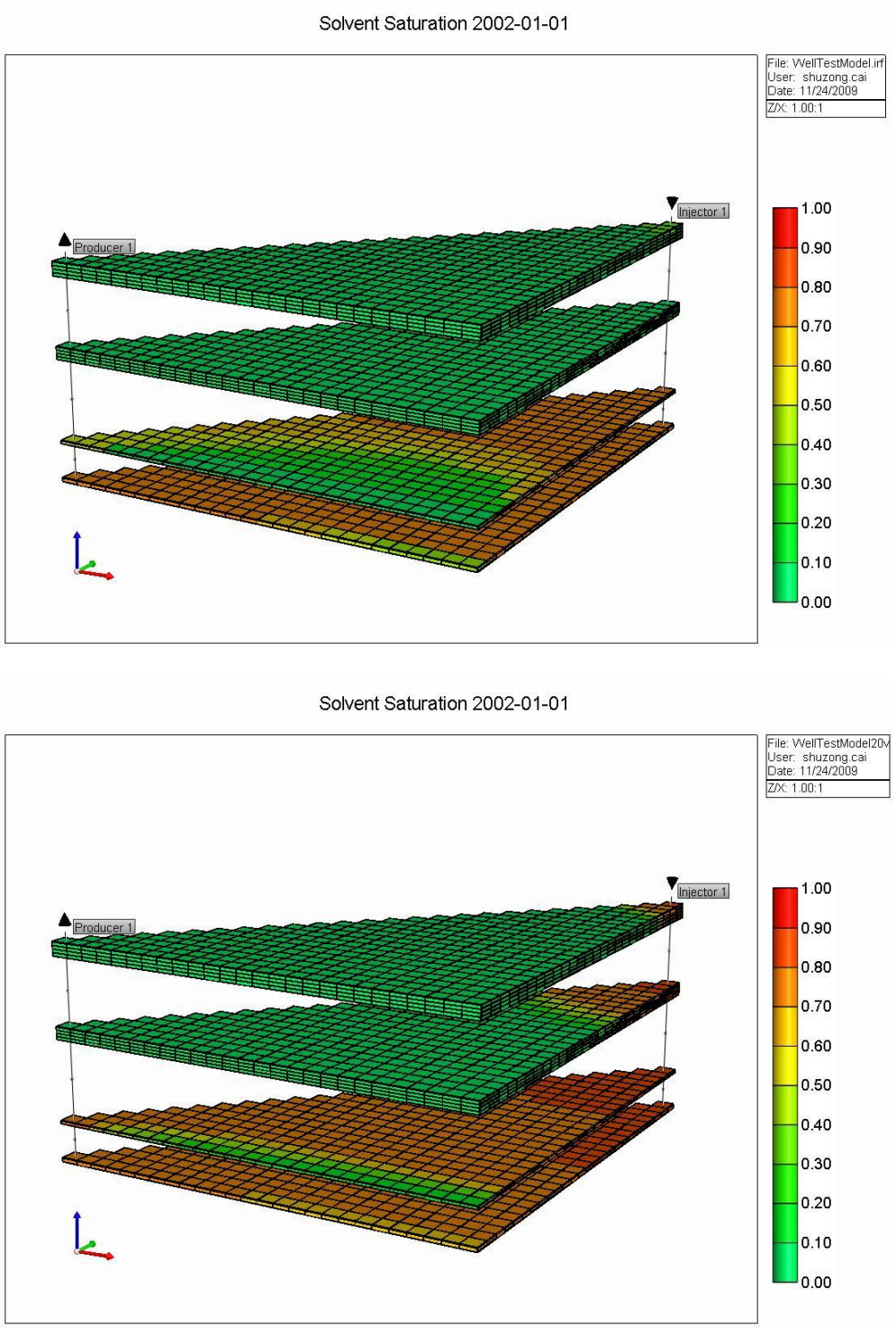

Fig. 4.113 – Solvent Saturation Distribution in the 3D Reservoir Model at the End of Simulation (Above: Case 4, Below: Case 5)

As revealed by the solvent saturation 3D representation in Fig. 4.113, most of the production in the two cases is from the lower two production intervals. This is caused by the high permeability of these two thin intervals. In Case 4, the problem is worsened with neat CO_2, as we can see that in the lowest layer CO_2 flows straight towards the production well. As a result, most of the upper three layers are not even swept by the CO_2 fluid. When CO_2 viscosity is increased 20 fold in Case 5, we see that the oil sweep efficiency in the third layer from top is improved and most of oil is recovered. However, in Case 5 the solvent saturation in the two upper layers increases very little compared with the neat CO_2 Case 4, with the first layer from top almost remaining untouched. The best way to address this problem is to use gel treatment to reduce the permeability of two high permeability intervals in the bottom (16.7 mD and 33 mD). This method will direct CO_2 to sweep the relatively lower permeability intervals (0.929 mD and 0.0704 mD).

CHAPTER V

CONCLUSIONS AND RECOMMENDATIONS

5.1 Conclusions

In the laboratory study, we completed the crosslinked polymer gel conformance control study and the direct CO_2 mobility control study using viscosifiers.

1. For the study of gel performance control, we tested 10,000 ppm high concentration gel and found out it was more stable compared with the 3,000 ppm gel. The 10,000 ppm gel gave a higher pressure drop in CO_2 flooding,leading to a better permeability reduction. We also proved the effectiveness of applying in-situ conformance control gel in carbonate reservoirs by carrying out CO_2 flood in heterogeneous carbonate core. In all the gel treatment experiments, we obtained incremental oil recovery during the resumed CO_2 flooding. Cross-linked HPAM/$Cr(OAc)_3$ gels could improve sweep efficiency and overall oil recovery
2. For the study of CO_2 viscosifiers, the control CO_2 flooding experiment using neat CO_2 was conducted twice; in both trials we obtained expected low recovery due to higher conductivity of the fracture. The first low molecular weight viscosifier of dodecamethylpentasiloxane was studied and we noticed significant differences in the CO_2 flooding images; a better CO_2 flood front was formed, suggesting the reduction in CO_2 mobility. We tested the high molecular weight compound PVAc and Polydimethylsiloxane with toluene as cosolvent. During the pressure drop tests, we determined PVAc to be a better compound for the

CO_2 mobility reduction. The PVAc viscosified CO_2 flooding process was then studied using the CT-scan technique. In comparison with the neat CO_2, significant differences for PVAc viscosified CO_2 were discovered in terms of CO_2 flood front, CO_2 saturation and oil recovery. CT images also showed that viscosified CO_2 provided better sweep efficiency. CO_2 flow preference in the lower half core was also observed in several coreflood experiments which could account for part of the oil recovered.

3. In our simulation work we looked at different cases which were modeled based on Geological Differences, Injection Well Position and Production Scheme. A black-oil pseudo-miscible model for Field P was developed using data from Well A. The basic assumptions from pseudo-miscible model were specified and then a general model was constructed to illustrate the simulation methodology. In the Well A Model, a neat CO_2 injection case and a viscosified CO_2 injection case were studied. Higher cumulative oil recovery and better sweep efficiency were observed for viscosified CO_2 case and CO_2 breakthrough was delayed using the viscosified CO_2. However, the heterogeneity of the permeability in the reservoir suggests that a gel treatment for high permeability layers might be necessary before conducting any CO_2 flooding.

5.2 Recommendations

1. Considering the limitations of setting up coreflood system under the CT scanner; the CT images are already sufficient for our analysis. However, better temperature control device during the CT scan and more complex and

accurate coreflood system is desirable which will yield more accurate and reliable quantitative results.

2. Larger core samples from other outcrop or drilling sources can further expand the scope of our research. Larger cores are especially useful in observing gravity drainage of the injected fluid. Alumina or titanium CT scan core holders with bigger diameter fittings are required for larger cores.
3. A survey on the industrial supply of siloxane or vinyl acetate polymers will certainly help to identify promising CO_2 viscosifier chemicals for field applications.

REFERENCES

1. Green, D.W., and Willhite, G.P.: "*Enhanced Oil Recovery*", Richardson: Henry L. Doherty Memorial Fund of AIME Society of Petroleum Engineers, 3 (1998).
2. Carbon Dioxide: Temperature – Pressure Diagram., http://www.chemicalogic.com/download/co2_phase_diagram.pdf Downloaded 4 May 2010.
3. Holm, L.W., and Josendal, V.A.: "*Mechanisms of Oil Displacement By Carbon Dioxide*", *JPT 26* (12), (1974) 1427-1438. SPE-4736-PA.
4. Giraud, A., and Thomere, R.: "*Dynamic Miscibility Contribution to the Study of Mixture Zones*", *Revue*, *IFP 23* (5), (1968) 95-102.
5. Farzad, I., and Amani, M.: "*Evaluating Reservoir Production Strategies in Miscible and Immiscible Gas-Injection Projects. Paper SPE 108014 presented at the Latin American & Caribbean Petroleum Engineering Conference*", *Buenos Aires, Argentina,* 15-18 April. (2007).
6. Glasø, Ø.: "*Generalized Pressure-Volume-Temperature Correlations*", *JPT* 32 (5), (1980) 785-795. SPE-8016-PA.
7. Benham, A.L., Dowden, W.E., and Kunzman, W. J.: "*Miscible Fluid Displacement-Prediction of Fluid Miscibility*", *Trans.*, AIME 219, (1960) 229-237.
8. Firoozabadi, A. and Aziz, K.: "*Analysis and Correlation of Nitrogen and Lean-Gas Miscibility Pressure*", *SPEREE* 1 (6), (1986) 575-582. SPE-13669-PA.
9. Eakin, B.E. and Mitch, F.J.: "*Measurement and Correlation of Miscibility*

Pressure of Reservoir Oils. Paper SPE 18065 presented at the SPE Annual Technical Conference and Exhibition", *Houston, Texas,* 2-5 October. (1988).

10. Cronquist C.: "*Carbon dioxide dynamic displacement with light reservoir oils. Paper presented at the 1978 U.S. DOE Annual Symposium*", *Tulsa, Oklahoma,* 28-30 August. (1978).
11. Vargas-Vasquez, S.M. and Romero-Zerón, L.B.: "*A Review of the Partly Hydrolyzed Polyacrylamide Cr(III) Acetate Polymer Gels*", *Petroleum Science and Technology* 26 (4), (2008) 481-498.
12. McCool S., Li X., and Willhite G.P.: "*Flow of a Polyacrylamide/Chromium Acetate System in a Long Conduit*", *SPEJ* 14 (1), (2009) 54-66. SPE-106059-PA.
13. Martin, F.D., and Kovarik, F.S.: "*Chemical Gels for Diverting CO_2: Baseline Experiments. Paper SPE 16728 presented at the SPE Annual Technical Conference and Exhibition*", *Dallas, Texas,* 27-30 September. (1987).
14. Seright, R.S.: "*Mechanism for Gel Propagation through Fractures. Paper SPE 55628 presented at the SPE Rocky Mountain Regional Meeting*", *Gillette, Wyoming,* 15-18 May. (1999).
15. Asghari, K., and Taabbodi, L.: "*Laboratory Investigation of Indepth Gel Placement for Carbon Dioxide Flooding in Carbonate Porous Media. Paper SPE 90633 presented at the SPE Annual Technical Conference and Exhibition", Houston, Texas,* 26-29 September. (2004).
16. Hild, G.P., and Wackowski, R.K.: "*Reservoir Polymer Gel Treatments to Improve Miscible CO_2 Flood*", *SPEREE* 2 (2), (1999) 196-204. SPE-56008-PA.
17. Karaoguz, O.K., Topguder, N.N., Lane, R.H., Kalfa, U., and Celebioglu, D.:

"*Improved Sweep in Bati Raman Heavy-Oil CO_2 Flood: Bullhead Flowing Gel Treatments Plug Natural Fractures*", *SPEREE* 10 (2), (2007) 164-175. SPE-89400-PA.

18. Raje, M., Asghari, K., Vossoughi, S., Green, D.W., and Willhite, G. P.: "*Gel Systems for Controlling CO_2 Mobility in Carbon Dioxide Miscible Flooding*", *SPEREE* 2 (2), (1999) 205-210. SPE- 55965-PA.
19. Asghari, K., Mirjafari, P., Mahinpey N., and Dong, M.: "*Reducing the Permeability of Sandstone Porous Media to Water and CO2: Application of Bovine Carbonic Anhydrase Enzyme. Paper SPE 99787 presented at the SPE/DOE Symposium on Improved Oil Recovery*", *Tulsa, Oklahoma,* 22-26 April. (2006).
20. Heller, J. P., Dandge, D.K., Card, R. J., and Donaruma, L. G.: "*Direct Thickeners for Mobility Control of CO2 floods*", *SPEJ* 25 (5), (1985) 679-686. SPE-11789-PA.
21. Terry, R. E., Zaid, A., Angelos, C., and Whitman, D. L.: "*Polymerization in Supercritical CO2 to improve CO2/Oil Mobility Ratios. Paper SPE 16270 presented at the SPE International Symposium on Oilfield Chemistry", San Antonio, Texas,* 4-6 February. (1987).
22. McClain, J.B., Betts, D.E., Canelas, D.A., Samulski, E.T., and DeSimone, J.M.: "*Characterization of Polymers and Amphiphiles in Supercritical CO2 using Small Angle Neutron Scattering and Viscometry*", *Polym. Mater. Sci. Eng*. 74, (1996) 234-235.
23. Bae, J.H.: "*Viscosified CO_2 Process: Chemical Transport and Other Issues.*

Paper SPE 28950 presented at the SPE International Symposium on Oilfield Chemistry", *San Antonio, Texas,* 14-17 February. (1995).

24. Enick, R.M., Beckman E.J. and Hamilton, A.: "*Inexpensive CO_2 Thickening Agents for Improving Mobility Control of CO_2 Floods*" http://www.netl.doe.gov/technologies/oil-gas/publications/EPreports/BC15315_FinalReport.pdf. (2005). Downloaded 21 April 2009.
25. Xu, J., Wlaschin, A., and Enick, R.M.: "*Thickening Carbon Dioxide With the Fluoroacrylate-Styrene Copolymer*", *SPEJ* 8 (2), (2003) 85-91. SPE-84949-PA.
26. Le, V.Q. and Nguyen, Q.P.: "*A Novel Foam Concept with CO_2 Dissolved Surfactants. Paper SPE 113370 presented at the SPE/DOE Symposium on Improved Oil Recovery*", *Tulsa, Oklahoma,* 20-23 April. (2008).
27. Huh, D.G., Cochrane, T.D., and Kovarik, F.S.: "*The Effect of Microscopic Heterogeneity on CO_2-Foam Mobility: Part 1-Mechanistic Study*", *JPT* 41 (8), (1989) 872-879. SPE-17359-PA.
28. Wang, G. C.: "*A Laboratory Study of CO2 Foam Properties and Displacement Mechanism. Paper SPE 12645 presented at the SPE/DOE Enhanced Oil Recovery Symposium*", *Tulsa, Oklahoma,* 15-18 April. (1984).
29. Liu, Y., Grigg, R.B., and Bai, B.: "*Salinity, pH, and Surfactant Concentration Effects on CO2-Foam. Paper SPE 93095 presented at the SPE International Symposium on Oilfield Chemistry*", *The Woodlands, Texas,* 2-4 February. (2005).
30. Fjelde, I., Zuta, J., and Duyilemi, O.V.: "*Oil Recovery from Matrix during CO2-Foam Flooding of Fractured Carbonate Oil Reservoirs. Paper SPE 113880*

presented at the Europec/EAGE Conference and Exhibition", *Rome, Italy,* 9-12 June. (2008).

31. Hounsfield, G.N.: "*A Method of an Apparatus for Examination of a Body by Radiation Such as X- or Gamma-Radation. British Patent No.1, 283,915*", London, UK (1972).
32. Wellington, S.L. and Vinegar, H.J.: "*X-Ray Computerized Tomography*", *JPT* 39 (8), (1987) 885-898. SPE-16983-PA.
33. Du, D., Zitha, P. L.J., and Uijttenhout, M.G.H.: "*Carbon Dioxide Foam Rheology in Porous Media: a CT Scan Study*", *SPEJ* 12 (2), (2007) 245-252. SPE-97552-PA.
34. Chakravarthy, D., Muralidaharan, V., Putra, E., Hidayati, D.T., and Schechter, D.S.: "*Mitigating Oil Bypassed in Fractured Cores During CO_2 Flooding Using WAG and Polymer Gel Injections. Paper SPE 97228 presented at the SPE/DOE Symposium on Improved Oil Recovery*", *Tulsa, Oklahoma,* 22-26 April. (2006).
35. Jossi, J.A., Stiel, L.I. and Thodos, G.: "*The Viscosity of Pure Substances in the Dense Gaseous and Liquid Phases*", *A.I.Ch.E. Journal* 8 (1), (1962) 59–63.
36. Todd, M.R. and Longstaff, W.J.: "*The Development, Testing, and Application Of a Numerical Simulator for Predicting Miscible Flood Performance*", *JPT* 24 (7), (1972) 874-882. SPE-3484-PA.

VITA

Name:	Shuzong Cai
Address:	Harold Vance Department of Petroleum Engineering Texas A&M University 3116 TAMU – 507 Richardson Building College Station, TX 77843-3116 c/o David Schechter
Email Address:	shuzong.cai@pe.tamu.edu
Education:	B.S., Chemistry, Peking University, China, 2006 M.S., Chemistry, New York University, 2008 M.S., Petroleum Engineering, Texas A&M University, 2010